Elastic and Inelastic Shock Compression of Diamond and Other Minerals

by

Ryan Stewart McWilliams

B.S. (University of Massachusetts, Amherst) 2001

A dissertation submitted in partial satisfaction of the

requirements for the degree of

Doctor of Philosophy

in

Earth and Planetary Science

in the

Graduate Division

of the

University of California, Berkeley

Committee in charge:

Professor Raymond Jeanloz, Chair
Professor Rudolf Wenk
Professor Geoff Marcy

Spring 2008

The dissertation of Ryan Stewart McWilliams is approved:

Chair _____ Date _____

_____ Date _____

_____ Date _____

University of California, Berkeley

Spring 2008

Elastic and Inelastic Shock Compression of Diamond and Other Minerals

by

Ryan Stewart McWilliams

Abstract

Elastic and Inelastic Shock Compression of Diamond and Other Minerals

by

Ryan Stewart McWilliams

Doctor of Philosophy in Earth and Planetary Science

University of California, Berkeley

Professor Raymond Jeanloz, Chair

Laser-driven shock wave experiments have been used to examine the response of diamond and quartz to conditions of high dynamic stress, and finite-strain theory has been developed to treat the shock response of these and other high-strength minerals in the elastic shock-compression regime. For diamond, two-wave shock structures featuring an elastic-precursor shock followed by an inelastic shock are observed. The Hugoniot elastic limits of diamond are measured to be 80.1 (± 12.4), 80.7 (± 5.8) and 60.4 (± 3.3) GPa for <100>, <110> and <111> orientations, respectively. The elastic yield strength of diamond inferred from these measurements is 75 (± 20) GPa and is strongly anisotropic. Inelastic-compression states beyond the Hugoniot elastic limit show a varying degree of strength retention, with the <111> orientation showing a retention of strength and the <110> orientation showing a loss of strength, based on comparisons with the ideal hydrostatic shock response of diamond. Diamond is nontransparent to VISAR interferometry above its elastic limit, likely due to scattering of light in shocked diamond behind the inelastic wave. The elastic-precursor shock is transparent; for elastic-uniaxial strain in the <100> and <110> directions the index of refraction along the compression axis increases. The two-wave structure in diamond is expected to persist to at least 450

GPa and to even higher stresses for short-duration experiments; this is inconsistent with the commonly used Hugoniot of diamond reported by Pavlovskii (1971). For α-quartz, a transition from optically transparent to reflecting is identified at a pressure of ~ 80 GPa on the Hugoniot. The VISAR index of refraction correction for transparent quartz at high pressure is found to be 1.16 (± 0.04). Eulerian and Lagrangian finite-strain formulations are developed to treat the case of elastic-shock compression at low stresses, for application to diamond, quartz and sapphire.

Chair Date

Table of Contents

Introduction

Carbon is the fourth most-abundant element in our solar system. The suggestion that significant quantities of condensed carbon, in the form of diamond, may be present in the interiors of hydrocarbon-rich giant planets such as Uranus and Neptune has remained resilient since it was first proposed by Ross [1-3]. Planetary models, therefore, will need to account for the properties of diamond at the extreme pressures and temperatures of planetary interiors. In extrasolar planetary systems, carbon may be even more abundant than in our own [4], and thus the equation-of-state of solid carbon may be even more relevant to describing the structure and evolution of extrasolar planetary bodies [5]. The diamond phase of carbon is also of unparalleled utility in numerous technological applications due to its high strength, transparency, chemical inertness, and high thermal conductivity. In studies of extreme states of matter, diamond is frequently used in to generate static high pressure conditions using the diamond-anvil cell, and has been proposed as a capsule material for inertial-confinement fusion experiments, at, for example, the National Ignition Facility.

In Chapter 1, new experiments investigating the equation-of-state of carbon at high (~ 100 GPa) pressures are reviewed. These experiments use the method of shock compression, by which supersonic compression waves are introduced to materials to generate well characterized states of high pressure and temperature. Under shock compression, diamond has been studied extensively in the high pressure regime, beyond about 600 GPa, where diamond melts into metallic liquid carbon [6]. However, below 600 GPa, where solid, insulating diamond is stable, there have been very few

experimental studies. It was observed previously that the study of diamond by shock waves at these pressures is complicated by the uniquely high strength of diamond [7].

One feature of shock compression of high-strength solids is the very high Hugoniot elastic limit (or HEL), which is the stress at which shock compression transitions from generating purely elastic strain in materials to inelastically or plastically deforming the material. Both above and below the HEL, theories of nonlinear elasticity can be used to examine the shock response – that is, the change in density as a function of applied stress. While finite-strain theory has been examined extensively to treat states of shock compression well beyond the HEL, it's has been only partially examined to treat elastic shock compressions below the HEL. The theory of finite strain for elastic shock compressions is developed in Chapter 2, and is then used to examine the elastic shock responses of several minerals, including diamond and quartz.

Finally, in Chapter 3, new observations on the shock-compressional response of silica (SiO_2) are presented, motivated by the use of quartz (α-SiO_2) as a standard material in the study of diamond presented in Chapter 1. Specifically, we examine the transition of silica from a transparent, solid insulator at low pressure to a strongly reflecting metallic fluid at high pressure.

Acknowledgements

I am in great debt to Raymond Jeanloz for the opportunity to study at Berkeley and Lawrence Livermore National Laboratory, and for his constant and optimistic support.

Thanks also to fellow Berkeley graduate students who have helped me along the way, Kanani Lee, Brent Grocholski, Victoria Lee, Wren Montgomery, Arianna Gleason, and Dylan Spaulding; Berkeley postdocs Sang-Heon 'Dan' Shim, Sergio Speziale, and Sébastien Merkel whose advice has been invaluable; and Berkeley staffmembers Tim Teague and Margie Winn, to name a few.

I am also in great debt to the researchers of Lawrence Livermore National Laboratory who have taken a great deal of time from their own schedules to train me and entertain my constant requests for assistance, particularly Jon Eggert, Damien Hicks, Peter Celliers, Ray Smith, Gilbert Collins, Steve Letts, Jim Cox, Walter Unites, Tim Uphaus, and above all, Dwight Price and the staff of the Jupiter Laser Facility. The enthusiasm, commitment, and seriousness of these researchers has had a profound influence on myself both scientifically and personally.

And of course, thanks to family, friends, and all that…

“A warrior calculates everything.”

- Don Juan

Chapter 1:

Shock Hugoniot, elastic limit, and strength of diamond under dynamic stress.

Abstract:

Laser-driven shock waves have been used to examine the elastic-inelastic response of single-crystal diamond shocked in the <100>, <110> and <111> crystallographic orientations. Two-wave shock structures featuring an elastic precursor followed by an inelastic shock are observed. Elastic precursors show evidence of stress relaxation behind the shock, decay of precursor amplitude with propagation distance, and a strong scaling with driving pressure, with precursors reaching maximum amplitudes of ~ 200 GPa. The Hugoniot elastic limits of diamond are measured to be 80.1 (± 12.4), 80.7 (± 5.8) and 60.4 (± 3.3) GPa for <100>, <110>,and <111> orientations, respectively. The elastic yield strength of diamond inferred from these measurements is 75 (± 20) GPa and is strongly anisotropic. Inelastic compression states beyond the Hugoniot elastic limit show a varying degree of strength retention, with the <111> orientation showing the largest retained strength, and the <110> orientation showing the least, based on comparisons with the ideal hydrostatic shock response of diamond. Diamond is nontransparent to VISAR interferometry above its elastic limit, likely due to scattering of light in shocked diamond behind the inelastic wave. The elastic precursor shock is transparent; for elastic uniaxial strain in the <100> and <110> directions, we find that the index of refraction of diamond along the compression axis increases. The two-wave structure in diamond is expected to persist to at least 450 GPa, and to even higher stresses for short-duration experiments. The present measurements are not consistent with those of Pavlovskii (1971), for which only a single-wave shock structure was reported for shock stresses from 100 to 600 GPa.

Introduction:

Diamond has the largest resistance to plastic flow of any material currently known [8], and many have sought to predict or measure it's yield strength [9-16]. Diamond is of unparalleled utility in numerous technological applications due to its high strength, transparency, chemical inertness and high thermal conductivity. In studies of extreme states of matter, diamond is frequently used to generate static high-pressure conditions in the diamond-anvil cell, and has been proposed as a capsule material for inertial-confinement fusion experiments. In the present study, we conducted shock-wave experiments on diamond to examine its strength response to high dynamic stress.

In solids, minimum elastic energy is obtained under hydrostatic (isotropic) stress conditions [17]. When stressed anisotropically, a solid material may behave as a fluid, with deformation relaxing the stress toward hydrostatic conditions, or the material can resist deformation, maintaining a state of anisotropic stress through strength effects. The rate of relaxation depends strongly on timescale, on the mode of relaxation – whether through fracture, flow, or recrystallization – and on other factors such as temperature and whether the solid is a crystal or a glass. For shock-compressed systems, experimental timescales are short, on the order of a nanosecond, and material often responds with a strength approaching theoretical limits. Thus, shock waves are uniquely suited for studying the ideal strength response of materials.

In shock loaded solids, strength can take a number of forms. The most conspicuous of these is the Hugoniot elastic limit (HEL), the point at which shock compressed states transition from conditions of elastic, uniaxial strain to those in which

yielding occurs. This is typically associated with the formation of a two-wave shock structure as driving stress rises above the HEL, with a fast elastic precursor followed by a slower inelastic-deformation shock.

In the inelastic shock, strength is manifested differently depending on the material (Fig. 1.1) [18-21]. Brittle solid single-crystals often exhibit a loss of strength in inelastic deformation above the elastic limit. The idealized model of total strength loss beyond the elastic limit is termed *elastic-isotropic*, in the sense that compression to the elastic limit is one of elastic uniaxial strain, while compression beyond the limit produces states of isotropic stress and strain. Materials that deform in this manner tend – above the elastic limit – to show a stress vs. strain response similar to the hydrostatic isotherm known from independent measurements of elastic moduli. In other shocked solids, particularly metals, the shear strength of a material is retained during yielding beyond the elastic limit. The idealized model in this case would be one of *elastic-plastic* deformation – so named as the yielding mechanism is often one of microscopic slip and plastic flow. Shock-compressed states for such materials exhibit a constant offset from the hydrostatic response, when plotted as stress vs. density (Fig. 1.1). The behavior of most materials under dynamic loading beyond the elastic limit can be said to fall between these limiting cases of total strength loss and total strength retention. In detail, strength loss is rarely complete, and strength may also increase with applied stress or work hardening [21] or with time after passage of the inelastic wave [22].

The manifestation of strength on inelastic compression often differs considerably from that indicated by the HEL. That is, materials of high strength and high elastic limits, such as brittle solids (e.g. quartz and silicon), show the greatest tendency toward loss of

strength, whereas materials with low elastic limits, such as metals, typically retain their strength beyond the elastic limit. This effect is likely related to differences in the mode of failure. In many brittle systems, the high initial strength promotes a catastrophic relaxation of shear stress once strength has been exceeded, similar to fracturing. In one model, heat is localized in macroscopic shear zones due to the low thermal diffusivity typical of brittle solids, enhancing slip, possibly through melting [20-22]. In metals, the strength is lower and, when exceeded, the release of energy is smaller; also, the formation of thermal heterogeneities is inhibited by larger thermal conductivity. In this case, deformation is thought to occur homogenously (plastically) by dislocation and slip on the microscopic scale, and strength is ultimately retained.

Diamond is a brittle dielectric with uniquely high thermal conductivity, which would promote dissipation of thermal heterogeneities. However, diamond also has an extremely high initial strength, and thus the potential for a large energy release on yielding. Diamond therefore does not have any obvious analogue among either typical brittle solids or metals, and it is unclear what mode of deformation would be favored. Diamond's resistance to plastic flow at ambient pressure and temperature is well known [8]. However, at high pressure [16] and high temperature [8], plastic flow is known to be possible in diamond, though on significantly longer timescales than explored by shock compression.

The only prior comprehensive study of the shock-wave response of single-crystal diamond below 600 GPa was made by Pavlovskii [23]. He reported single-wave shocks propagating in the <100> orientation of diamond for shock stresses ranging from 100-600 GPa. However, subsequent observations by Kondo and Ahrens [7] on arbitrarily oriented

diamond, and Knudson et. al. [24] on <110> oriented diamond for final shock stresses between 180 and 250 GPa, showed the existence of a two-wave structure. The precursor amplitudes in these studies ranged from 62 (± 5) GPa [7] to 95 (± 5) GPa [24]. These are the largest-amplitude elastic precursors ever observed, consistent with the high strength of diamond. The observation of elastic precursors in later studies calls into question the earlier results of Pavlovskii.

A suite of laser-driven shock experiments have previously probed the high-stress Hugoniot of diamond from 500 to 3500 GPa [6, 25-28], and the melting transition beginning at ~ 600 GPa [6, 26, 28], yet the low-stress, solid-phase Hugoniot of diamond remains remarkably unexplored by dynamic experiments. Here we report a comprehensive study of the two-wave structure in diamond shocked in three primary single-crystal orientations, <100>, <110> and <111>, to final stresses ranging from 100 to 600 GPa.

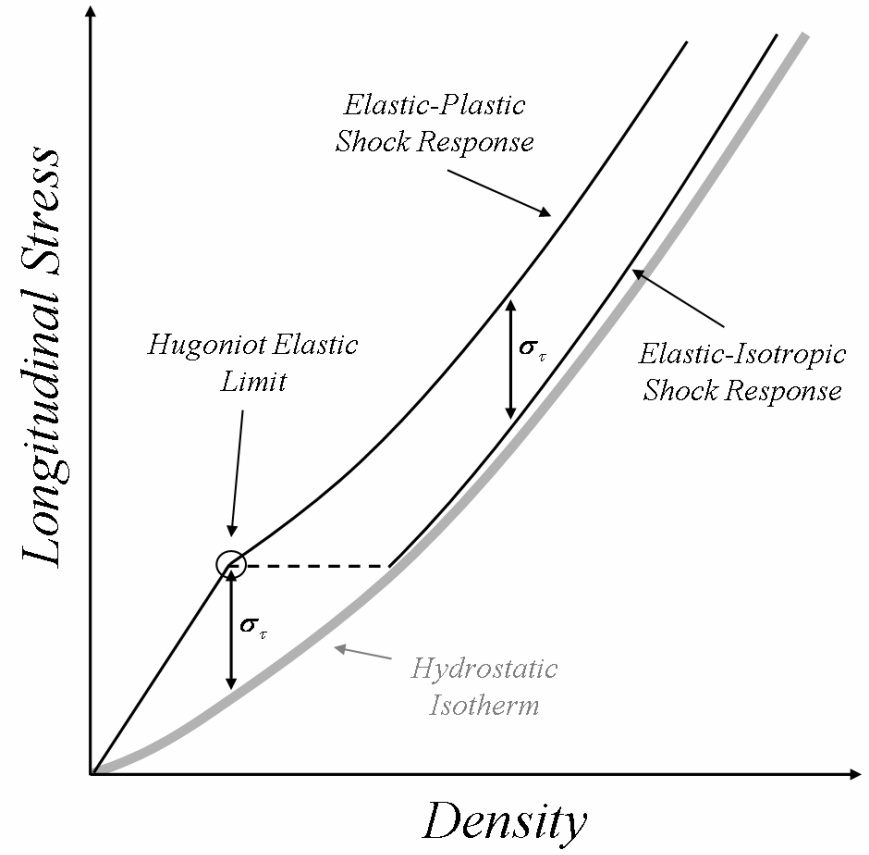

Figure 1.1. Elastic-plastic vs. elastic-isotropic shock loading models. The elastic-isotropic model shows a total collapse to hydrostatic compression above the HEL, with a small offset from the hydrostatic isotherm due to shock heating and thermal pressure. The elastic-plastic model shows a persistent offset from the hydrostat (σ_τ) due to finite shear strength which, for this simple model, has been assumed constant at high density.

Experimental techniques and observations:

Shock waves were driven by 2 beams (100 GW) of the Janus laser at Lawrence Livermore National Laboratory, and 6 beams (3 TW) of the Omega laser at the Laboratory for Laser Energetics, University of Rochester. Pulse durations were varied from 6 ns to 1 ns to produce different types of loading conditions. The 6 ns pulses produced an optimum degree of shock steadiness during the experimental timescale, while 1-4 ns pulses produced decaying shock-wave conditions.

A suite of time-resolved diagnostics were used to constrain the conditions of the shock state. Two line-imaging Velocity Interferometer for Any Reflector (VISAR) systems [29, 30] were used to obtain interferometric and travel-time velocity measurements, and a line-imaging Streak Optical Pyrometer (SOP) [31, 32] was used to measure thermal emission. In the Janus facility, all streak cameras used were Hamamatsu C7700-01 models. At the Omega facility, streak cameras were of custom design. To obtain accurate timing measurements in the streak cameras, streak images of 10-25 ns fullscale were used, and variations in sweep rate with time were accounted for. The time resolution of these diagnostics was ~ 100 ps. At ambient conditions, diamond is transparent at the visible wavelengths used by these diagnostics.

The diamond samples studied were cut for shock propagation in three primary crystallographic orientations, <100>, <110> and <111>. The <100> and <110> samples were completely transparent and inclusion-free Ia and IIa diamonds fashioned into circular discs 100-500 μm in thickness and 1 mm in diameter, with the two broad surfaces polished; these were supplied by Delaware Diamond Knives, Inc. and Harris

Diamond Co. The <111> samples were inclusion-free Ib diamonds, yellow in color, cut into 1 mm-sided squares, and ~ 200 μm thick with the broad surfaces formed by cleavage along (111) planes; these were supplied by Almax Industries. Additionally, a CVD polycrystalline diamond sample was used in several very high-stress experiments. These were of solid density, completely transparent, with a thickness of ~ 400 μm.

Crystallographic orientations are assumed to be of the orientation requested from the supplier, but it is of interest to estimate the deviation from the desired orientation. In the case of <111> diamonds, distinct cleavage planes on each broad face allow direct measurement of the angle between crystallographic orientation and the bulk surface normal, which defines the shock propagation direction; this angle was 1/4 degree or less for all <111> samples. In the case of <110> and <100> oriented samples, this angle can be estimated from the parallelism of opposing surfaces, by assuming one surface is of correct orientation and the other of incorrect orientation. For the maximum thickness variation over a 1 mm diameter observed in these diamonds (5 μm), a ~ 1/3 degree misalignment would be suggested; thus it is likely that the shock propagation direction should lie within a few degrees of the <100> and <110> orientations. For polycrystalline samples, x-ray diffraction analysis showed that the surface normal corresponded to a weak texture in the <111> orientation; that is, the (111) planes of individual crystallites were on average aligned with the direction of shock propagation.

The general target design is shown in Fig. 1.2. Diamonds were mounted on a diamond-turned aluminum base disk, 3 mm in diameter and 50 μm thick, with 8-15 μm of plastic ablator (CH) deposited on the opposite surface. In most targets, an anti-reflection (AR) coated quartz window was placed adjacent to the diamond as a reference

standard. In some targets, two ~100 μm thick diamonds of identical orientation were stacked, with a 100 nm layer of aluminum deposited on part of the interface between them, to provide an internal surface at which to study shock arrivals.

Each diamond was examined, both before and after mounting, with a Wyco optical surface profilometer (Veeco Instruments) to measure the thickness of diamond at different positions over the 1 mm wide sample. In some <111>-oriented samples, cleavage on different (111) planes often resulted in a series of steps on the surfaces. Samples with steps were either engineered such that the steps did not interfere with the measurements, or were not used. Thickness measurements reported in Table 1.1 correspond to the particular area of each diamond studied in the experiment; for stack targets, the thickness corresponds to the total thickness of the stack.

Target components were aligned, stacked with a low-viscosity Norland-63 UV-cure photopolymer glue between parts, and compressed using a Fineplacer Pico (Finetech GmbH). Compression reduces gaps between parts to a minimum defined only by surface irregularities and trapped dust. Targets with gap thicknesses larger than ~1 μm were discarded, since at larger gap thicknesses, the reverberation of the shock in the gap causes a perturbation in travel-time measurements on the order of the uncertainty. For this reason all parts were closely inspected for dirt, scratches and other defects during assembly, and gaps were characterized rigorously. Due to the high reflectivity of aluminum and diamond surfaces, interference fringes are observed in gaps when illuminated by white light. These interference fringes, in combination with surface profilometry, are used to characterize gap thicknesses over the entire target. The 100 nm

aluminum layer in the interface of stacked diamonds was too thin to significantly affect wave propagation in the present experiments.

Drive laser focii were smoothed using phase zone plate technology to generate uniform irradiation over a square region 1000 μm on a side, or a circular region 650 μm in diameter. In this way a planar shock of the same dimension as the focal spot was generated in the target. By the time the shock propagated across the target, lateral rarefaction reduced the diameter of the planar region to between 950 and 200 μm, depending on target thickness, the phase plate used, and, for the square plate, the plate rotation relative to the target. The extent of the planar region is constrained by the spatial uniformity of arrival times at a given depth in the target, as observed in VISAR records [30].

Representative VISAR records from the experiments are shown in Fig. 1.3. The interferometric measurement of velocity by VISAR is given by [29, 30]

$$\text{Velocity} = (\phi + b) \times \left(\frac{\lambda}{2\tau(1+\delta)\chi} \right) \qquad \text{(Eq. 1.1)}$$

The second term in parenthesis is referred to as the VPF, or velocity-per-fringe, in which λ is the wavelength of the VISAR probe laser (532 nm), τ is the optical delay time introduced by the etalon in one leg of the interferometer, $(1+\delta)$ is a correction for optical dispersion in the etalon, and χ accounts for index of refraction effects in the shocked target. The first term in parentheses is the number of fringes shifted, where ϕ is the fringe phase shift measured relative to the initial fringes, which are due to reflection from initially static (unmoving) surfaces, and b is the unknown integer number of base fringe

shifts. The optical delay τ used in each VISAR channel was different, allowing the number of base fringe shifts b for each VISAR to be unambiguously resolved [30].

Fig. 1.3.a shows results from an experiment on a single diamond. On shock arrival at the aluminum-diamond interface, the intensity of the fringes drops suddenly. This is due to the loss of reflected light from the aluminum base, resulting from the nontransparency of the shocked diamond. At this point, only reflection from the static free surface is visible, and thus $\phi = 0$. The free surface of diamond is strongly reflective because of diamond's high index of refraction, ~ 2.4. About 5 ns later, two shocks arrive at the free surface, identified by two consecutive shifts in the fringes. The magnitude of these shifts gives the free surface velocity, u_f, through Eq. 1.1, where $\chi = 1$ since the surface is in vacuum.

In Fig. 1.3.b, an experiment on a stacked diamond target is shown. Shock arrival events at the base and at the free surface are similar to those in Fig. 1.3.a. Shock arrival is also recorded at the aluminized portion of the internal interface, shown at the bottom of the VISAR record in Fig. 1.3.b. The first shock wave, upon arrival at this interface, is transparent to VISAR, and a fringe shift is measured. The actual velocity implied by this fringe shift is unknown, as the value for χ in this case depends on the index of refraction of shocked diamond which has not been previously measured. The arrival of the second shock at the internal interface corresponds to a sharp reduction in fringe intensity, due to the nontransparency of shocked diamond behind the second wave and loss of reflection from the aluminum layer. The fringe shift returns to $\phi = 0$ due to remaining reflection from the static free surface.

The loss of transparency of shocked diamond behind the second wave is likely due to scattering of the VISAR laser probe beam as it passes through deformed solid diamond. This is consistent with the identification of the first, transparent wave as an elastic precursor, and the second as an inelastic deformation wave. A similar situation arises with sapphire which, when shocked beyond its HEL, exhibits reduced transparency to optical probes such as VISAR due at least in part to scattering effects [33-35]. It is unlikely that diamond becomes nontransparent due to intrinsic (electronic) absorption, as the band gap of carbon is expected to remain large throughout the stress range that shocked diamond remains solid [36, 37]. The loss of transparency was not due to glue between target components becoming opaque at high pressure and temperature, because reflected light would still have been observed from diamond-glue interfaces in this case. Using broadband reflectometry [32], we found in a single experiment on <110> diamond that the loss of transparency was strong from 532 to 750 nm (Fig 1.6).

While Fig. 1.3.a and 1.3.b utilized steady-pressure drives made by 6 ns laser pulses, the record in Fig. 1.3.c used a very intense short pulse (1 ns) that produced a decaying wave. Immediately after breakout into diamond, the shock is strongly reflecting and the shock state is molten [6, 28]. With increasing time, shock velocity and stress at the shock front decrease, as does the reflectivity, until shock reflection ceases entirely (and the state immediately behind the shock front is solid). Only very weak fringes are visible after this point due to an AR coating on the free surface of the diamond. A two-wave structure is then observed at the free surface, as the free-surface reflectivity increases on shock arrival. This feature was reported previously, though with a different interpretation [30].

In general, a loss of free-surface reflectivity is observed during the arrival of the second wave. In cases where the free surface remained clean during target assembly (Fig. 1.3.a), the reflectivity is unchanged on first-wave arrival, and is followed by a reduction on second-wave arrival. When the surface was coated in a thin layer of material, either an AR coating (Fig 1.3.c) or a film deposited by outgassing from epoxy (Fig. 1.3.b), the reflectivity increased on first wave arrival, but was also followed by a strong drop in reflectivity on second wave arrival. While these thin surface layers, ~100 μm thick, affected the optical properties of the target, they did not significantly affect the compression and release response at the free surface. The observed drop in reflectivity on second-wave arrival may be related to crystal breakup, and a consequent roughening of the free surface.

Fig. 1.4 shows free-surface velocities of diamond following arrival of the first and second shocks, determined from the average of the two VISAR channels. The wave profiles of diamond on first-wave free-surface arrival feature a sharp shock with a discontinuous jump in u_f, followed by decreasing u_f with time prior to second-wave arrival. This is a common characteristic of elastic-precursor waves that is attributed to shear-stress relaxation behind the elastic shock through inelastic deformation [21, 22, 38]. On second-wave arrival, the wave profile varies in form depending on driving stress and orientation. For <100> and <110> oriented shocks at intermediate stresses, the wave profile features a sharp leading shock, and a subsequent slow rise to a limiting free-surface velocity. This form is probably due to the interaction of the two-wave structure with the free surface, which will be considered in more detail later. At low driving stresses for <100> and <110> shocks, and to intermediate stresses for <111>-oriented

shocks, the second-wave arrival consists of a slow rise in free-surface velocity, without any sharp discontinuity; at high stresses, all orientations display a sharp rise with no apparent structure.

The primary functions of the adjacent quartz window were to act as a reference for the shock conditions in the aluminum base and to provide time-resolved data on shock steadiness. For the majority of experiments conducted here, quartz is shocked into the molten regime and the shock front is reflecting and emissive [39, 40], permitting direct observations of the conditions at the shock front with VISAR and optical pyrometry.

In Fig. 1.3.a, the quartz shock front is reflecting, and shows slight variations in shock velocity (and reflectivity) with time, as indicated by changes in fringe position (and intensity) over the course of the record. Shock velocity is measured interferometrically in the VISAR with $\chi = 1.56$, which is the index of refraction of quartz at ambient conditions. The variations in shock velocity with time are due to the inherent unsteadiness of the laser drive, and are used to characterize the degree of shock steadiness and the uncertainty it induces in these experiments (Appendix A). The thermal emission variations are consistent with the variations in velocity and reflectivity. In Fig. 1.3.b, an inappropriate epoxy used to construct the target damaged the anti-reflection coating by outgassing, preventing direct observation of the weakly-reflecting quartz shock front with VISAR. In this case, the transit time of the 137 μm thick quartz window is visible, providing a measurement of the average shock velocity in the window. In such experiments with failed AR coatings, the variation in shock conditions with time was still observed in SOP records, as thermal emission penetrated the surface layer (Fig. 1.5).

For a single experiment at the lowest stress studied here, quartz was transparent behind the shock wave. In this case, the velocity of the quartz-aluminum interface was measured. This measurement depends on the index of refraction of quartz at high pressure, which is not known. In separate experiments (discussed in Chapter 3), we determined the index of refraction correction for quartz in the high-pressure regime to be $\chi = 1.16$ ($\pm$ 0.04), which is comparable to the value at low pressures of $\chi = 1.08$ [41].

For experiments above ~400 GPa, drive-decay effects cause a significant breakdown of steady-shock conditions, as shown in Fig. 1.3.c. The two-wave structure at the free surface persists until, with increasing drive stress, only a single free-surface arrival is observed, corresponding to a single, inelastic shock-wave. There are two explanations for this. One possibility is that a single-shock front decays below a critical limit during the experiment, and splits into two waves. It is also possible, that, on shock breakout into diamond, a high-amplitude, attenuating precursor wave forms ahead of the attenuating inelastic shock, in some cases being overrun by the inelastic wave before reaching the free surface and in other cases surviving, depending on the relative decay rates of the two waves. However, as our interest for these decaying-wave experiments is entirely in the state of the elastic precursor observed at the time of free-surface arrival, the state of the trailing inelastic wave does not matter significantly.

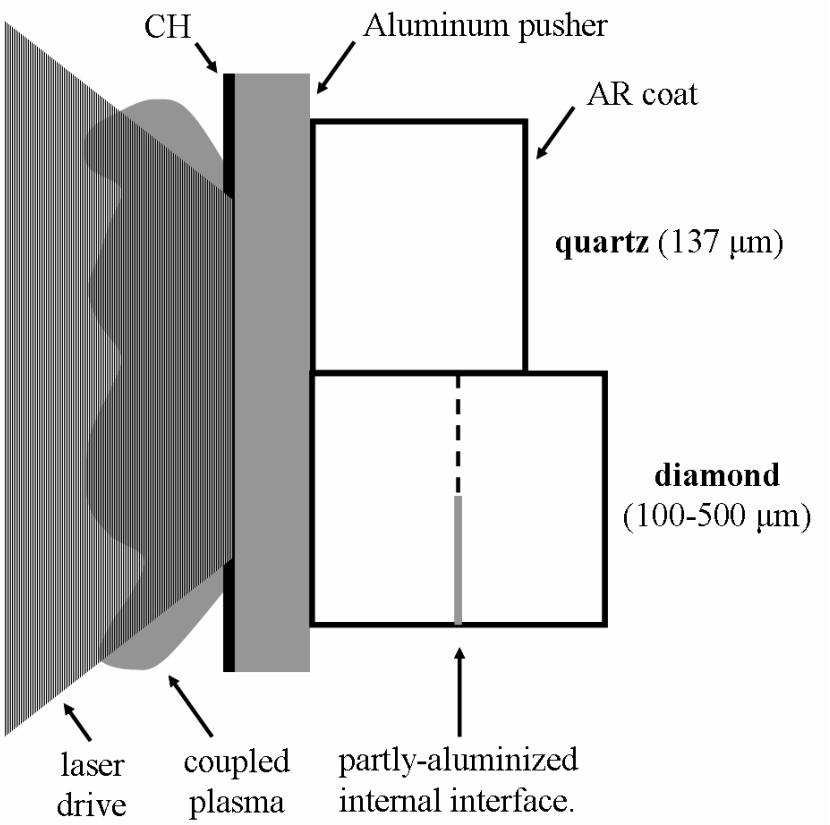

Figure 1.2. General target design. In some cases, two diamonds were stacked on each other, forming a single diamond with an internal interface, which was partially aluminized. An anti-reflection coating was used on quartz, but was damaged in some cases during target assembly. For some experiments an anti-reflection coating was also used on the diamond. Targets are situated in an evacuated chamber during the experiment. The drive laser strikes the target from the left, while VISAR and SOP view the target from the right.

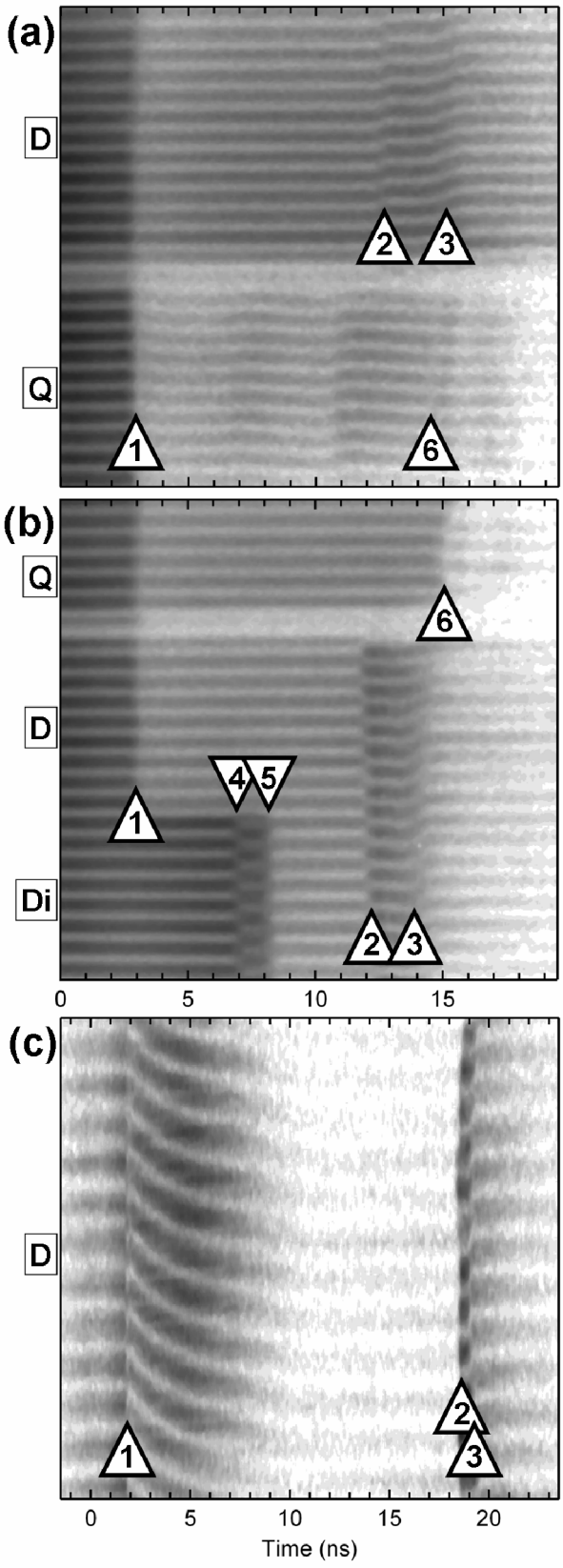

Figure 1.3. Line VISAR records of the three types of experiments used in the present study. Shot *dh14* (a) used a single diamond target, D, with an adjacent quartz reference window, Q. Shot *dh8* (b) used a stacked diamond target with a section of the internal interface aluminized, Di, and an adjacent quartz reference. Shot *43637* (c) used a single diamond target. Records (a) and (b) used a VISAR VPF (χ = 1) of 6.221 km/s/fringeshift and record (c) used a VPF (χ = 1) of 16.09 km/s/fringeshift. The vertical axis is about 950 μm fullscale for (a) and (b), and 300 μm fullscale for (c). Events are indicated by numbered triangles. 1: breakout from aluminum base, diamond and quartz are rendered opaque and reflection from aluminum ceases (reflecting shock front is visible in quartz in (a), and diamond in (c); for other cases, only an intensity drop is registered at breakout, with $\phi = 0$ since reflection comes from unmoving surfaces ahead of the shock). 2, 3: arrival of elastic, inelastic waves (respectively) at diamond free surface, fringes shift. 4: arrival of elastic wave at internal aluminized interface, wave is transparent and fringes shift. 5: arrival of inelastic wave at internal aluminized interface, wave is nontransparent and reflection from internal interface ceases. 6: arrival of shock at quartz free surface, more distinct in shot (b) due to damaged AR coating. In (c) the diamond shock is strongly decaying, and transitions from reflecting to opaque during sample transit; the reflectivity of the free surface, reduced with an anti-reflection coating, increases on shock arrival.

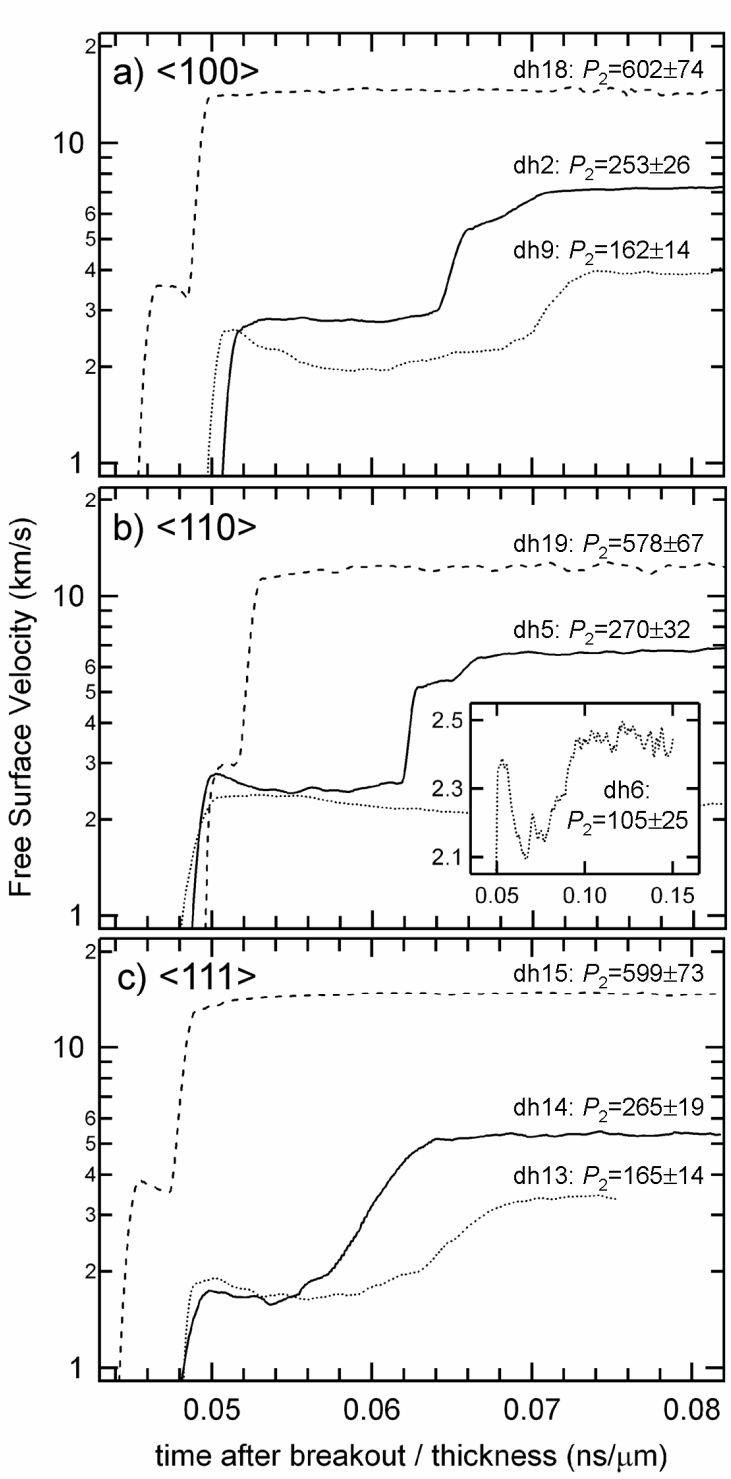

Figure 1.4. Free surface velocity u_f vs. normalized time, given as the time after the shock enters the diamond divided by the thickness of the diamond, for orientations <100> (a), <110> (b) and <111> (c). Normalization to diamond thickness results in identical arrival times for disturbances traveling at the same velocity. Ends of records, when shown, correspond to end of streak windows.

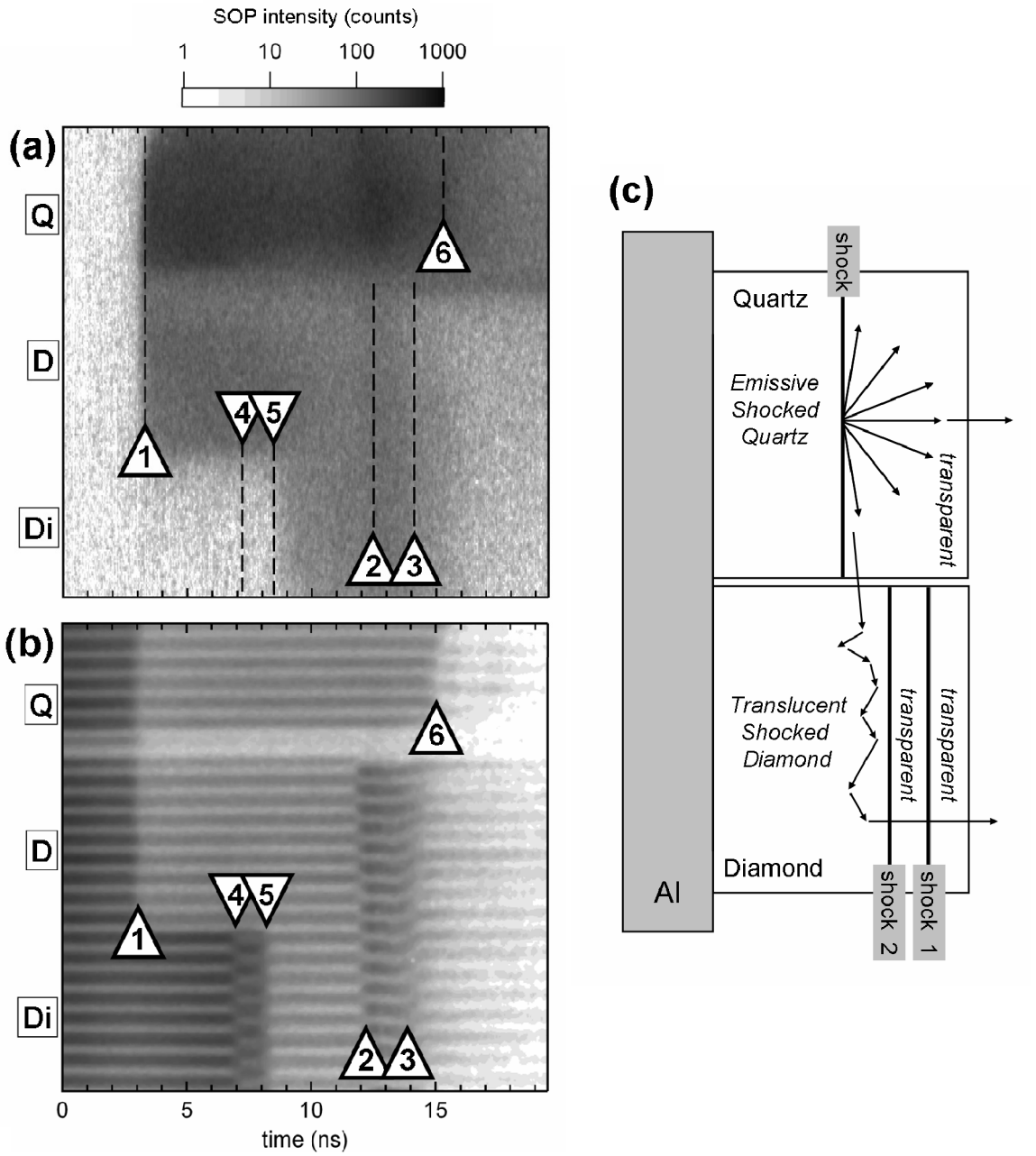

Figure 1.5. (a) Streak optical pyrometer record showing thermal emission (in counts) vs. time and target position. Corresponding VISAR record shown in (b) is the same as in Fig. 1.3.b; labeling is the same as in Fig. 1.3. The emission from the quartz emerges directly from the shock front; variations in the intensity with time between events 1 and 6 correlate with variations in shock-front velocity and stress. Between events 4 and 5 there is an absence of emission from the first wave in diamond. Emission in diamond emerges from behind the inelastic wave, and mimics the temporal variation in the quartz emission. We attribute this effect, visible in all experiments, to thermal emission from the quartz shock front scattering through the adjacent shocked diamond and into the pyrometer (c). This is due to the apparent translucence of inelastically shocked diamond and the faster shock velocity in diamond than in quartz. In other words, shocked diamond itself is not strongly emitting up to shock stresses of at least 400 GPa.

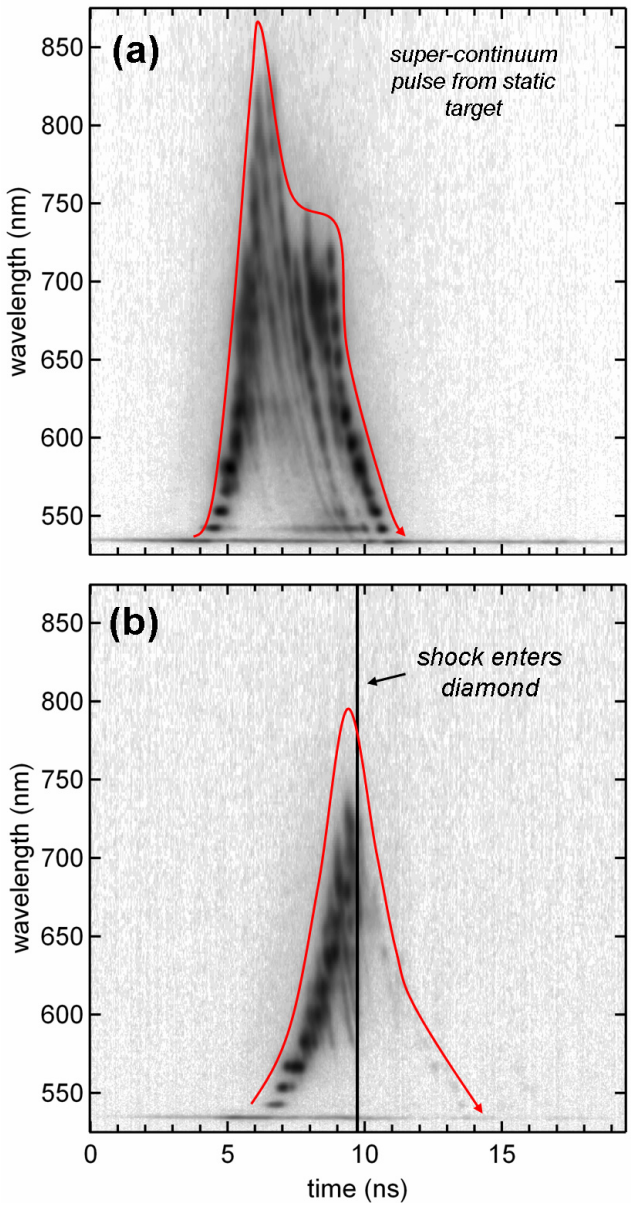

Figure 1.6. White-light reflectometry technique described in reference [32]. Image (a) shows a reference pulse reflected from aluminum, showing wavelength structure with time. The maximum wavelength at a given time is given by the red curve. Image (b) shows a similar pulse in which a strong shock breaks out from aluminum into <110>-oriented diamond at the moment of peak wavelength excursion. The rest of the pulse is strongly attenuated due to non-transparency of shocked diamond in a wavelength band between 532 nm and 750 nm. The stress in diamond is ~100 GPa.

Determination of Hugoniot states:

To determine the stresses and densities of shock-compressed states, we used the Rankine-Hugoniot equations, with shock speeds D, particle speeds u, densities ρ, volumes $V=1/\rho$, and longitudinal shock stresses P, which are equivalent to pressure in the case of strengthless, hydrostatic conditions behind the shock.

For a single shock wave, the Hugoniot equations are:

$$P_1 = P_0 + \rho_0 D_1 u_1 \qquad \text{(Eq. 1.2)}$$

and

$$\rho_1 = \rho_0 \frac{D_1}{D_1 - u_1} \qquad \text{(Eq. 1.3)}$$

where subscripts '0' and '1' indicate conditions ahead of and behind the shock front, respectively. For a two-wave system, with subscript '2' indicating conditions behind the second shock front, the description of the final state becomes:

$$P_2 = P_1 + \rho_1 (D_2 - u_1)(u_2 - u_1) \qquad \text{(Eq. 1.4)}$$

and

$$\rho_2 = \rho_1 \frac{D_2 - u_1}{D_2 - u_2} \qquad \text{(Eq. 1.5)}$$

Equations 1.4 and 1.5 reduce to the one-wave equations 1.2 and 1.3 if the intermediate state 1 is set to the initial conditions $u_1 = 0$, $\rho_1 = \rho_0 = 3.515$ g/cm^3 for diamond, and $P_1 = P_0 = 0$.

These relations assume steady-state conditions ahead of and behind the shock front, and that the shock itself is a discontinuity in P, ρ, and u. In real materials, and also

due to experimental limitations, these assumptions are not always satisfied, as will be discussed. However, in most cases, these equations are expected to be applicable given that the associated uncertainties have been considered.

The three orientations of diamond examined in the present study are the only ones expected to respond with ideal one-dimensional motion of both shock front and shocked matter for purely elastic compressions [42-44]. Other orientations could display quasi-shear waves, which are not consistent with the one-dimensional Rankine-Hugoniot relations Eq. 1.2 to 1.5. Furthermore, other orientations are likely to exhibit multiple elastic shocks.

We now describe how velocities D_1, u_1, D_2 and u_2 – and hence, the stress and density conditions behind the two shocks – are obtained. The Hugoniot is the locus of possible P-ρ-D-u states that can be achieved by shock compression of a material. In these experiments, the two-wave shock system achieves states on two separate Hugoniots – the elastic Hugoniot, in which compression is approximately elastic and uniaxial, and the inelastic Hugoniot, where significant inelastic deformation is occurring.

Measurement of u_1:

The particle velocity behind the first wave u_1 is determined from the free surface velocity u_{f1} after arrival of the first wave, using the common assumption $u_{f1} = 2u_1$ [7, 18, 45, 46]. This assumption is particularly appropriate for elastic waves as the compression and release processes are isentropic and hence reversible. The uncertainty in our measurement is estimated from the full range of particle speeds observed between first and second wave arrivals at the free surface. Due to the reduction in free-surface velocity after the initial arrival of the first shock, the upper bound on the particle velocity ($u_1 + \delta u_1$)

is that observed immediately after arrival, and the lower bound (u_1 - δu_1) is observed, typically, right before the second wave arrives at the free surface. The change in free-surface velocity with time is not large and should not have a major effect on the interpretation of measurements through the steady-wave assumption implicit in the Rankine-Hugoniot relations.

In principal, the fringe shift observed on arrival of the elastic precursor at the internal aluminized interface of stacked targets is related to u_1 through χ, which in this case depends on the index of refraction of elastically shocked diamond, which is not known *a priori*. However, measurement of u_1 at the free surface, and (ϕ + b) at the internal interface, can be used to determine χ through Eq. 1.1. We find that $\chi \sim 2$ for both <100>-and <110>-oriented diamond under large elastic-strain conditions. This implies a strong increase in the index of refraction of diamond observed along the longitudinal (wave-propagation) direction at large uniaxial strain, in contrast to the decrease in index found under hydrostatic stress [47, 48].

Measurement of D_1:

The shock velocity of the first wave D_1 is determined from the transit time through the diamond and the diamond's thickness. Both the first and second shock are presumed to originate at the aluminum-diamond interface at the moment the shock enters the diamond. The arrival time of the first shock at the free surface is identified by the first jump in free-surface velocity. For stack targets, first-wave arrival is also recorded at the internal aluminized interface, where it is identified by the shift in VISAR fringes.

The velocities of the first waves are comparable to the longitudinal elastic sound speeds in each orientation, $c_{L<100>}$=17.53 km/s, $c_{L<110>}$=18.32 km/s and $c_{L<111>}$=18.58

km/s, determined from the ambient pressure elastic constants [44, 49]. The high shock velocities of the first wave, in addition to the characteristic decay in particle velocity behind the shock and the high transparency of this wave, are evidence that the first wave is indeed an elastic precursor.

In all five experiments using stacked diamonds in which elastic-precursor transits were definitively measured for both diamonds, the velocity in the first diamond was greater than in the second (Fig. 1.7), by ~1 km/s. While the change in velocity was on the order of the measurement uncertainty, it is statistically significant that all 5 experiments exhibited this reduction in precursor speed in the second diamond; furthermore the uncertainty in these measurements is primarily systematic, such that the difference in velocity is better constrained than the magnitude. This is consistent with the observation of decreasing particle velocity behind the elastic precursor, in that both phenomena are associated with stress relaxation behind elastic shocks [21, 22, 38, 50]. As the decrease in velocity is on the order of the absolute uncertainty, we use the average of the velocities as the measurement of D_1 for stacked targets.

For a subset of our elastic-wave data at the highest stresses, where experiments produced strongly decaying shock waves, the only measurement on the elastic wave was the particle velocity u_1 made upon arrival at the free surface. To determine D_1 in these cases, various elastic Hugoniot models, fit to the elastic-wave data at lower stresses, were extrapolated into the high-stress regime and used to estimate D_1, P_1 and ρ_1. These models, including linear D-u and Lagrangian and Eulerian finite strain fits, are discussed below and are described in detail in Chapter 2. In some of the highest-stress precursor studies, CVD polycrystalline diamonds were used, which were assumed to be well

represented by the extrapolation of the <111> elastic Hugoniot. Using this approach, precursors with longitudinal stresses up to $P_1 \sim 200$ GPa are inferred.

Measurement of D_2:

The inelastic shock-wave velocity D_2 was determined in two ways: a) by shock arrival at the internal aluminized interface of a stacked target, in which the arrival was selected by the sudden loss of optical transparency and, at the lowest stresses, a visible fringe shift before transparency was lost; and b) at the free surface, where arrival was identified by the second jump in free-surface velocity. At the internal interface, the movement of the interface due to the earlier arrival of the elastic precursor was accounted for by adding to the diamond thickness an amount equal to the precursor particle velocity u_1 multiplied by the time between elastic- and inelastic-wave arrivals.

At the free surface, the effect of the earlier arrival of the elastic precursor is more complicated, as interaction between the free-surface release of the elastic precursor and the approaching inelastic wave must be considered [19, 45, 51, 52]. A schematic of this interaction is shown in Fig. 1.8: L is the sample thickness, D_1, u_1 and t_1 are the shock velocity, particle velocity and transit time of the elastic precursor, respectively; D_2 and t_2 are the shock velocity and apparent arrival time of the inelastic wave, D_{1R} is the speed of the rear-propagating rarefaction wave from the free surface release of the precursor, and D_3 is the speed of the leading wave following interaction between the waves D_{1R} and D_2 at time t_i. We seek to use this interaction to measure D_2.

We begin with the assumption that D_{1R} is a sharp (shock-like) rarefaction with $D_{1R} = D_1 - u_1$. The assumption for D_3 is often the least certain [18, 45, 51], and its

estimation will be discussed shortly. Fig. 1.8 puts several constraints on the free-surface interaction due to the first reverberation:

$$L = D_2 t_i + D_3(t_2 - t_i) - 2u_1(t_2 - t_1) \quad \text{(Eq. 1.6.a)}$$

$$L = (D_1 - u_1)(t_i - t_1) + D_2 t_i \quad \text{(Eq. 1.6.b)}$$

$$L = D_1 t_1 \quad \text{(Eq. 1.6.c)}$$

$$L \equiv D_2' t_2 \quad \text{(Eq. 1.6.d)}$$

where D_2' is the apparent second-wave velocity if the elastic precursor is not accounted for. The unknown parameters are D_2 and t_i. Solving for D_2 with Eq. 1.6.a and 1.6.b, we obtain

$$D_2 = \frac{(t_2 - t_1)(2D_1u_1 - 2u_1^2 - D_3D_1 + D_3u_1) + L(D_1 - u_1 + D_3)}{t_2(D_3 - 2u_1) + t_1(u_1 + D_1)} \quad \text{(Eq. 1.7)}$$

This correction is also described by Ahrens et. al. [51], but differs from another common formula proposed by Wackerle [45]:

$$D_2 = D_2'\left\{1 - \frac{t_2 - t_1}{t_1}\left[\frac{(D_3 - 2u_1)(D_1 - 2u_1)t_2 - D_1^2 t_1}{D_1(D_3 - 2u_1)t_2 + D_1^2 t_1}\right]\right\} \quad \text{(Eq. 1.8)}$$

We use Eq. 1.7 in our analysis. In any case, the difference in the corrections to D_2' implied by formulae 1.7 and 1.8 differ by on the order of 10%, which is not significant given other uncertainties in this analysis.

The arrival time t_2 was selected by the time of the sharpest rise in free-surface velocity – i.e. the point of maximum strain rate – during the inelastic-wave arrival. In some experiments on <100> and <110> diamond with final stresses from 200-300 GPa, the inelastic wave arrival event featured a sharp, leading discontinuity with a velocity jump nearly equal to the first jump on arrival of the elastic precursor, suggesting that this

jump corresponded to an elastic shock reverberation – that is, the first reverberation in Fig. 1.8. This first reverberation arrival was also visible in the wave profiles of Knudson [24] for shock compression to similar final stresses in the <110> orientation of diamond, and has also been observed in silicon [52, 53], aluminum [19] and MgO [20]. The reverberation shock had a slightly larger free-surface velocity jump than the first. This could be a result of irreversible structural changes, such as work hardening, due to the first elastic precursor [19], or could be a manifestation of precursor attenuation, as the reverberation shock has less time to decay than the original precursor. The absence of a sharp reverberation in <111> diamond at these same conditions suggests some difference in the reverberation process. This could be due to a longer risetime of the inelastic shock in that orientation, which would produce a broader reverberation wave instead of the sharp wave that would form on interaction with a discontinuous shock. At $P_2 < 200$ GPa, no sharp elastic reverberations are observed in any orientation.

For the estimation of D_3, we began with the approximation that $D_3 = D_1 + 2u_1$, which assumes that diamond is re-stressed following the release of the initial elastic precursor to support a new elastic wave with the same properties as the first [18, 45, 51]. This assumption seems particularly realistic for the experiments mentioned above where t_2 is identified by the arrival of an elastic-like reverberation shock at the free surface. However, by comparing the velocity D_2 measured in the first diamond of a stacked target with that determined by applying the free-surface correction, we find that the latter approach consistently yields a slower velocity. The value of D_3 which results in the best agreement between the two measurements is 77-87% of $D_1 + 2u_1$ for P_2 between 150 and 300 GPa. This could be due, in part, to systematic differences in the way inelastic-wave

arrivals were selected at the internal interface (loss of transparency) and the free surface (point of maximum strain rate), since it is possible that transparency loss occurs earlier than the maximum strain-rate point in the shock front. We considered the range of $(D_1 + 2u_1) > D_3 > (D_2 + 2u_1)$ in applying the free-surface correction, in which the lower bound was selected because it closely matched the lower suggested value of D_3.

For single-diamond targets, D_2 was determined using the free-surface correction as in Eq. 1.7. For stack targets, D_2 was determined from the uncertainty-weighted average of the free-surface correction and the first-diamond transit velocity. At $P_2 < 200$ GPa, the shock velocity obtained with the free-surface correction becomes increasingly imprecise, due to increased time between the reverberations and the uncertainty in D_3. For single targets, this increases the measurement uncertainty in D_2; for stacked targets, the weighted average is dominated by the more precisely-known transit velocity of the first diamond. This is one advantage of having an internal surface in the target at which to measure shock arrival in two-wave experiments.

At $P_2 > 400$ GPa, drive-decay effects resulted in a large range of shock velocities being achieved throughout the experiment. At these stresses, the reverberation time at the free surface is so small that the free-surface correction has a negligible effect on the shock velocity. It is observed in stacked targets that D_2 measured after first-diamond transit was significantly larger than the D_2 measured after transit of the stack. This difference could only be explained by a large reduction in shock velocity during transit. The decay in shock velocity was also apparent when the shock front was initially reflecting on breakout into diamond. Thus for $P_2 > 400$ GPa, inelastic-wave conditions are either reported with appropriately large uncertainties, or are not reported.

Measurement of u_2, P_2, and ρ_2: Impedance Matching:

We use the method of impedance matching to determine the final state of the inelastic shock, finding u_2, P_2 and ρ_2 simultaneously, using the measured shock conditions in the aluminum base, the measured elastic precursor conditions and the measured inelastic wave velocity D_2. The impedance match construction is shown in Fig. 1.9. The state of diamond immediately prior to the arrival of the inelastic shock is given by the conditions of the elastic precursor. On arrival of the inelastic wave, diamond is taken along the Rayleigh line in P-u space, which has a slope $\rho_1(D_2 - u_1)$, from the state of the elastic precursor to the final state. The intersection of the Rayleigh line with the reshock-response of aluminum defines the final state. The mirror reflection of the aluminum Hugoniot about the initial driver condition is known to accurately represent the reshock (and release) response [54] at the conditions studied here. For the aluminum Hugoniot, we used the Sesame 3700 tabular equation of state [55], which is a good description of the Hugoniot below ~500 GPa [54], the upper pressure limit in aluminum examined in this study.

The initial state of the aluminum is found by reverse impedance-matching from the quartz reference window, using the directly-measured shock conditions in quartz. We used the Sesame 7360 tabular EOS [56] which is a good representation of the quartz Hugoniot data for $P > 40$ GPa and thus for all the experiments described here. The quartz conditions are determined by a combination of interferometric velocity measurements of the shock front; velocity measurements from transit of the quartz window; constraints on shock-front stability using streak optical pyrometry; and the scaling of quartz conditions with laser energy, which was needed to establish quartz conditions in a few experiments

where a direct measurement was not possible. The measurement of the quartz conditions is a major source of uncertainty in the determination of the second-wave state.

Alternatively, u_2 could be estimated from the free-surface release velocity in the same manner as u_1 was obtained, that is by assuming that $u_2/u_{f2} = 0.5$. This assumption has often been used to determine the conditions behind the second wave in elastic-inelastic compression experiments (e.g. [46, 52, 57]). However, in diamond this assumption significantly underestimates u_2. We observe ratios of $u_2/u_{f2} \sim 0.65$ for <110>- and <100>-oriented samples and a ratio of $u_2/u_{f2} \sim 0.85$ for <111>-oriented samples. These ratios appear to be roughly constant over the stress range studied here. This was also reported by Kondo and Ahrens [7], who observed $u_2/u_{f2} \sim 0.6$ for their nearly-<111> oriented samples. The deviation from the frequently assumed behavior of $u_2/u_{f2}=0.5$ is likely related to the details of the free-surface reverberation and the strength of diamond on release, and it is beyond the scope of this study to consider this phenomenon quantitatively.

Comment on Uncertainties:

For elastic waves, uncertainties in shock velocities are primarily due to uncertainty in transit time and sample thickness. For inelastic waves, the uncertainty in shock velocity was due to a combination of transit-time uncertainty, sample thickness uncertainty, and, for arrival measurements made at the free surface, the uncertainty in the free-surface correction as given by the range of D_3.

Uncertainties in transit times are generally a combination of those due to the sweep rate of the streak camera; the reduced time resolution due to the width of the streak camera entrance slit; the reduced time resolution due to the delay associated with VISAR

etalon; ambiguities in the identification of arrival times; and variations in transit time with spatial position, which, due to the high spatial uniformity of the laser drive, were due primarily to variations in target thickness. Usually, a given arrival measurement is uncertain by ~100-200 ps, and transit-time measurements by ~150-250 ps. Diamond thicknesses are uncertain by typically 0.5-2%, primarily due to variations in thickness over the region studied in the experiment.

When determining transit times, it is critical to use a self-consistent criterion for identifying arrival times that accounts for the finite time resolution of the VISAR. For example, shock arrival at the aluminum-diamond interfaces resulted in an intensity drop; however free-surface arrival was often associated with an intensity rise. Due to the finite time-width of events in the VISAR, it would be inappropriate to define the transit time as the difference between the moment of intensity drop and the moment of intensity rise, as this does not use a consistent measure of arrival time; instead, it is more appropriate to measure the timing between two consecutive intensity drops, or two intensity rises. This is often possible, if temporal intensity profiles are integrated over spatial widths much smaller than the VISAR-fringe period. Significant systematic errors are incurred if this effect is ignored.

Unsteadiness of the laser drive provided an additional source of uncertainty. This was accounted for in quasi-steady-drive experiments by using a large uncertainty in the quartz reference conditions to account for variations in drive pressure. For decaying shots, the uncertainty in the shock-wave velocity in diamond was increased based on the decay in velocities observed in stacked targets. Estimation of these uncertainties is discussed in greater detail in Appendix A.

Uncertainties in the directly measurable quantities D_1, u_1, D_2 and D_{Al} are reported as mean values with an associated uncertainty that was selected conservatively to contain approximately two standard errors; that is, these uncertainties represent approximately a 95% confidence interval for the measured quantities.

Fig. 1.9 shows the impedance-match construction, with the first shock point established through the Rankine-Hugoniot equations and the second shock point established through impedance matching. Uncertainties in quantities are represented in two ways: by orthogonal uncertainties about a central point (error bars), and by a confidence-bounding region which appears as a polygonal shape. The confidence-bounding region encompasses all possible solutions to the Rankine-Hugoniot equations and impedance-match construction that exist within the uncertainties of the directly measurable quantities; that is, this region is approximately a 95% confidence bound. Confidence-bounding regions were established by a Monte-Carlo uncertainty-propagation method to fully account for covariance between the directly measured quantities and the calculated stresses P_1 and P_2, densities ρ_1 and ρ_2, and particle velocity u_2. It can be seen in Fig. 1.9 that orthogonal error bars fail to adequately represent the true uncertainty of the measurement. In all plots where orthogonal uncertainties misrepresent the true uncertainty, a confidence-bounding region is shown instead. In table 1.1, data has been reduced so that orthogonal uncertainties are reported for all quantities P_1, ρ_1, u_2, P_2 and ρ_2, however information is lost by using this approximation.

The confidence-bounding region is necessarily polygonal in P-u space, due to the geometry of impedance matching. In other spaces, particularly P-ρ, the confidence-

bounding region is not exactly polygonal, but in most cases can be adequately represented by a four-cornered polygonal region.

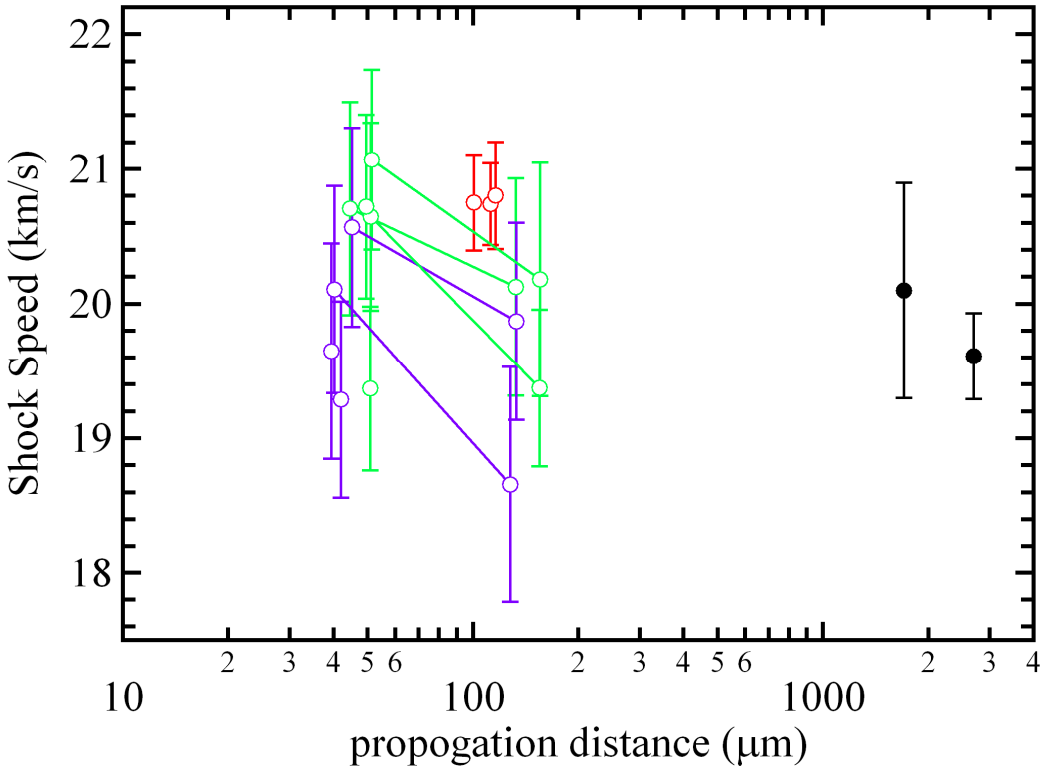

Figure 1.7. Elastic precursor velocity vs. propagation distance. Red, green and purple coloration are data on <111>, <110> and <100> orientations, respectively. Black points are data of Kondo and Ahrens [7]. Lines connect the two velocities measured in stacked-diamond targets. Elastic shock speed is defined as $(d_2 - d_1)/(t_2 - t_1)$, where d_1 and t_1 refer to the thickness and arrival time, respectively, corresponding to the first observed shock arrival, and d_2 and t_2 to the second arrival. Propagation distance is defined as $(d_2 - d_1)/2$. Uncertainties in thickness are on the order of 1% and are not plotted. To completely describe precursor variability (specifically, the variation of precursor conditions with inelastic-wave conditions) a third axis showing the conditions of the inelastic wave would be needed.

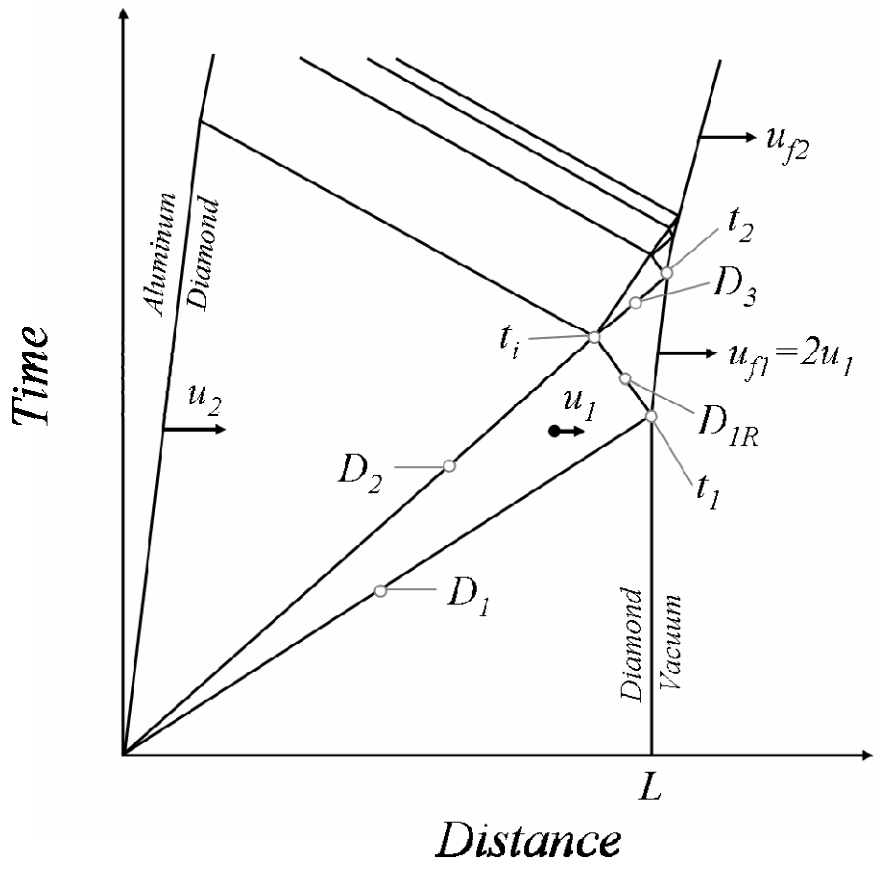

Figure 1.8. Time-distance plot of waves and reverberations due to release of the elastic precursor at the free surface before the arrival of the inelastic wave, after [19, 51, 52]. Rarefactions are approximated as discontinuous waves.

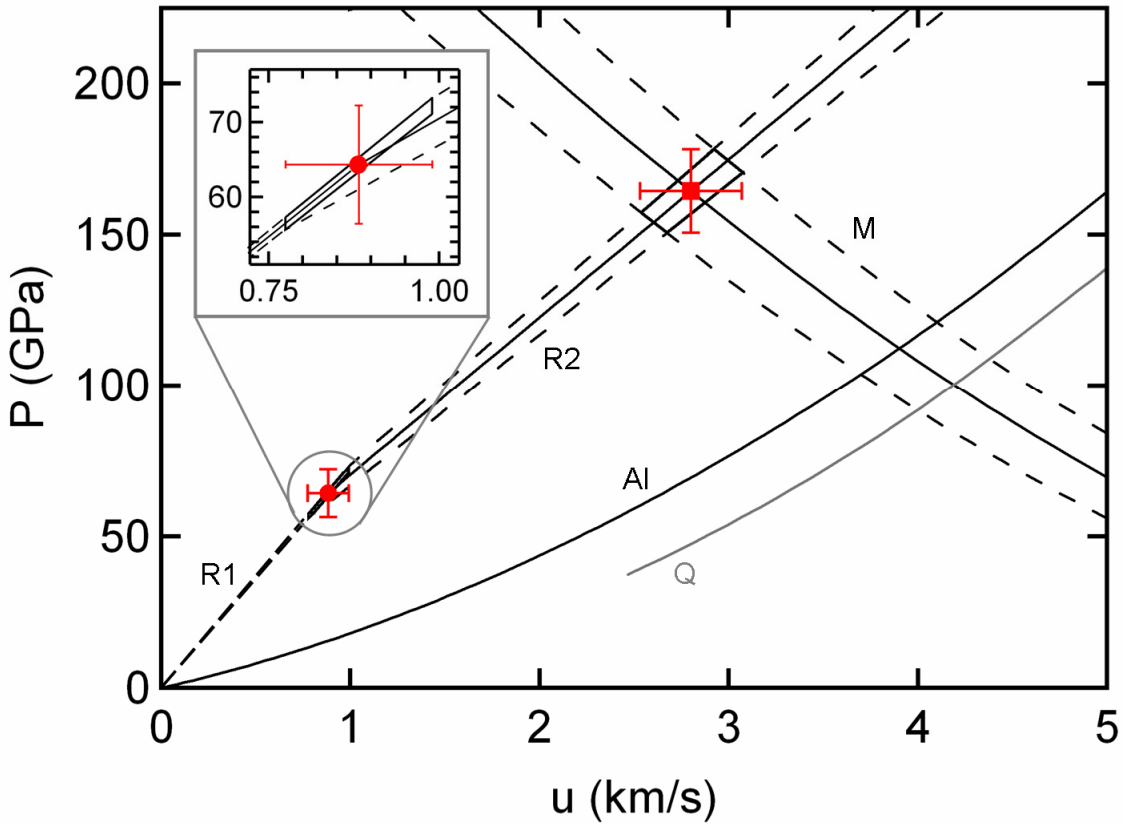

Figure 1.9. Impedance-match technique for a two-wave system, shot *dh13*. The path to the first state is indicated by Rayleigh line R1, with a slope of $\rho_0 D_1$, and the path from the first to the second state is indicated by Rayleigh line R2, with a slope of $\rho_1(D_2 - u_1)$. The Hugoniot of aluminum (Al) is reflected (M) about the initial state of Aluminum, intersecting with the quartz Hugoniot (Q) and the Raleigh line R2, determining the state in the second wave in diamond. For R1, R2 and M, the solid lines represent the central solution and the dashed lines the uncertainty at ~ 95% confidence. Uncertainties in first- and second-wave states are represented by polygonal confidence-bounding regions; orthogonal uncertainties in P and u, represented by the error bars, misrepresent the true measurement uncertainty due to covariance.

Table 1.1. Elastic Precursor and Inelastic Wave Hugoniot Measurements

			Steady Loading Experiments										Weakly Decaying		Strongly Decaying Experiments								
	Facility		**Janus**															**Omega**					
	shot		dh6	dh10	dh9	dh13 [f]	dh3	dh2 [f]	dh8	dh14	dh5	dh1	dh12	dh17	dh19 [d,f]	dh15 [d,f]	dh18 [d]	43633 [e]	43637 [e]	42454 [e]	41649 [e]	29424 [e]
	window		single	stack	stack	single	single	single	stack	single	stack	single	stack	single	stack	single	stack	single	single	single	single	single
	orientation		<110>	<110>	<100>	<111>	<100>	<100>	<100>	<111>	<110>	<110>	<110>	<111>	<110>	<111>	<100>	CVD	CVD	<110>	<110>	<110>
	Energy	J	150	354	362	377	387	738	791	726	799	791	635	698	723	736	746	1991.3	1011.7	2650.1	924.9	2239.6
	Duration	ns	6	6	6	6	6	6	6	6	6	6	4	4	4	4	4	1	1	1	1	1
	phase plate		1mm	1mm	1mm	1mm	1mm	1mm	1mm	1mm	1mm	1mm	1mm	1mm	650μm	650μm	650μm	650μm	650μm	650μm	650μm	650μm
	Intensity	W/m^2	2.50E+16	5.90E+16	6.03E+16	6.28E+16	6.45E+16	1.23E+17	1.32E+17	1.21E+17	1.33E+17	1.32E+17	1.59E+17	1.75E+17	5.45E+17	5.55E+17	5.62E+17	3.96E+18	2.01E+18	5.27E+18	1.84E+18	4.46E+18
	thickness	μm	99.1	207.9	175.9	224.0	83.8	78.8	174.7	201.3	175.6	101.8	207.7	232.0	205.6	169.8	167.3	419	419	500	500	425
	error		1.0	1.4	1.4	1.0	1.3	1.3	1.6	1.5	2.6	1.3	2.2	1.4	1.5	1.3	1.5	…	…	…	…	…
Elastic Precursor Conditions	D_1	km/s	20.72	19.90	20.22	20.74	19.29	19.65	19.47	20.75	20.42	19.37	20.74	20.81	19.55	22.43	21.60	24.72	23.34	21.59	20.87	21.33
	δD_1		0.68	0.45	0.52	0.30	0.73	0.80	0.58	0.36	0.56	0.61	0.53	0.40	0.82	0.62	1.10	0.59	0.31	1.71	0.71	1.03
	u_{f1}	km/s	2.215	2.445	2.255	1.765	2.650	2.800	2.995	1.655	2.565	2.605	2.791	1.865	3.075	3.650	3.465	4.989	3.945	5.425	3.400	4.450
	δu_{f1}		0.142	0.085	0.345	0.215	0.250	0.100	0.315	0.085	0.205	0.135	0.265	0.186	0.200	0.210	0.195	0.150	0.165	0.285	0.400	0.200
	u_1	km/s	1.107	1.223	1.128	0.883	1.325	1.400	1.498	0.828	1.283	1.303	1.395	0.932	1.538	1.825	1.733	2.494	1.973	2.713	1.700	2.225
	δu_1		0.071	0.043	0.173	0.108	0.125	0.050	0.158	0.043	0.103	0.068	0.132	0.093	0.100	0.105	0.098	0.075	0.083	0.143	0.200	0.100
	P_1	GPa	80.66	85.49	80.12	64.34	89.83	96.69	102.51	60.37	92.06	88.70	101.72	68.18	105.68	143.90	131.56	216.75	161.81	205.82	124.73	166.80
	δP_1		5.82	3.54	12.43	7.89	9.12	5.23	11.20	3.27	7.79	5.37	9.98	6.91	8.18	9.17	9.98	8.34	7.11	19.57	15.28	10.98
	ρ_1	g/cm^3	3.7135	3.7451	3.7226	3.6712	3.7743	3.7847	3.8078	3.6610	3.7505	3.7683	3.7685	3.6799	3.8150	3.8263	3.8215	3.9094	3.8395	4.0202	3.8267	3.9244
	$\delta\rho_1$		0.0151	0.0101	0.0341	0.0200	0.0283	0.0157	0.0347	0.0082	0.0213	0.0164	0.0267	0.0175	0.0252	0.0216	0.0253	0.0169	0.0156	0.0549	0.0416	0.0301
Inelastic Wave Conditions	D_2	km/s	10.76	12.71	13.64	15.12	13.41	15.21	15.86	16.49	16.44	15.40	16.45	16.90	19.77	20.62	20.81	… [c]	… [c]	… [c]	… [c]	… [c]
	δD_2		1.46	0.38	0.39	0.64	0.93	0.81	0.41	0.53	0.41	0.64	0.92	0.94	1.39	1.73	1.75	… [c]	… [c]	… [c]	… [c]	… [c]
	u_{f2}	km/s	2.432	… [a]	3.958	3.200	4.748	7.300	7.340	5.305	6.700	7.580	… [b]	… [b]	… [b]	… [b]	… [b]	… [c]	… [c]	… [c]	… [c]	… [c]
	δu_{f2}		0.100	… [a]	0.142	0.200	0.258	0.300	0.310	0.145	0.230	0.200	… [b]	… [b]	… [b]	… [b]	… [b]	… [c]	… [c]	… [c]	… [c]	… [c]
	u_2	km/s	1.779	2.869	2.891	2.799	2.995	4.384	4.317	4.392	4.418	4.763	4.423	5.156	8.322	8.154	8.180	… [c]	… [c]	… [c]	… [c]	… [c]
	δu_2		0.660	0.266	0.297	0.269	0.349	0.486	0.312	0.325	0.335	0.380	0.542	0.533	0.903	0.936	0.948	… [c]	… [c]	… [c]	… [c]	… [c]
	P_2	GPa	104.8	156.4	162.3	164.5	166.0	252.7	256.7	264.7	270.3	272.5	273.5	316.4	577.7	599.1	601.6	… [c]	… [c]	… [c]	… [c]	… [c]
	δP_2		25.0	11.8	14.1	13.9	16.4	26.3	17.5	18.9	19.4	21.1	31.4	32.4	67.5	72.4	74.3	… [c]	… [c]	… [c]	… [c]	… [c]
	ρ_2	g/cm^3	3.9911	4.3713	4.3330	4.2422	4.3794	4.8280	4.7378	4.7401	4.7288	4.9945	4.7173	5.0032	6.0750	5.7683	5.7722	… [c]	… [c]	… [c]	… [c]	… [c]
	$\delta\rho_2$		0.3929	0.1560	0.1698	0.1351	0.2319	0.3191	0.1841	0.1823	0.1811	0.2717	0.3084	0.3503	0.8101	0.7596	0.7700	… [c]	… [c]	… [c]	… [c]	… [c]
Reference Conditions	D_{Al}	km/s	9.081	10.56	10.66	10.63	10.78	12.73	12.73	12.86	12.93	13.17	12.97	13.83	17.82	17.86	17.89	… [c]	… [c]	… [c]	… [c]	… [c]
	δD_{Al}		0.710	0.27	0.28	0.27	0.30	0.42	0.28	0.30	0.31	0.32	0.49	0.46	0.72	0.72	0.72	… [c]	… [c]	… [c]	… [c]	… [c]
	D_Q	km/s	6.950	8.950	9.075	9.033	9.233	11.61	11.61	11.75	11.83	12.07	11.87	12.75	16.95	16.99	17.03	… [c]	… [c]	… [c]	… [c]	… [c]
	δD_Q		0.980	0.351	0.361	0.357	0.388	0.49	0.32	0.32	0.32	0.33	0.51	0.53	0.71	0.71	0.72	… [c]	… [c]	… [c]	… [c]	… [c]

a) inelastic wave free surface arrival missed
b) u_{f2} does not correspond to u_2 due to decaying wave conditions and is not reported
c) inelastic wave conditions vary over several Mbar during shot, specific values not estimated.
d) reported precursor conditions are lower bounds
e) precursor conditions estimated from extrapolation of finite-strain elastic models and linear *D-u* fit
f) quartz shock conditions not observed by either interferometry or window transit time; estimated from scaling of quartz conditions with laser energy

Modeling the hydrostatic Hugoniot response of diamond:

The high-pressure hydrostatic isotherm of diamond is well known from a combination of elastic constant measurements through Brillouin and Raman scattering [49, 58]; diamond-anvil cell x-ray diffraction measurements to static pressures of 140 GPa [59]; improved constraints on the ruby fluorescence static pressure scale [60]; and first-principles calculations [61, 62]. Since no phase transitions are expected in solid diamond until at least 400 GPa, and likely as high as 1000 GPa [6, 36], it is expected that the isothermal equation of state measured to 140 GPa can be reasonably extrapolated into the high-pressure regime with the appropriate equation of state model.

In making a comparison with shock wave measurements, the difference between the isotherm and shock Hugoniot at high stresses must be considered. To do this, we first assume that the final state of the shocked system is one of hydrostatic stress. In other words, the shock response of diamond will be modeled as if it were that of an elastic-isotropic solid. The extent to which the measurements deviate from this predicted hydrostatic shock response will then be used to directly determine the strength of diamond under elastic and inelastic loading.

The shock response of a material can be predicted by a thermodynamic pathway that considers isentropic compression to the final volume, V_2, followed by isochoric heating at V_2 to final pressure P_2 and internal energy E_2. The isentropic compression step can be described by a third-order Birch-Murnaghan equation of state [63], where the subscript S is used to denote isentropic conditions.

$$P_S(f) = 3K_{0S}f(1+2f)^{5/2}\left[1+(3/2)(K_{0S}^{/}-4)f\right] \qquad \text{(Eq. 1.9)}$$

Where the Eulerian finite strain $f = (1/2)[(V_0/V)^{2/3}-1]$, K_{0S} is the isentropic bulk modulus, and $K_{0S}^{/} = (\partial K_{0S} / \partial P)_S$ is the pressure derivative of the bulk modulus. The isochoric heating step can be described by the Gruneisen equation of state, $\gamma = V(\partial P / \partial E)_V$, where γ is the Gruneisen parameter, leading to

$$P_2(V_2) = P_S(V_2) + (\gamma / V_2)\left[E_2(V_2) - E_S(V_2)\right] \qquad \text{(Eq. 1.10)}$$

The internal energy of the final state E_2 is defined from the Rankine-Hugoniot equations for a 2-wave system as

$$E_2 - E_0 = \tfrac{1}{2}\left(P_2 + P_1\right)\left(V_1 - V_2\right) + \tfrac{1}{2}\left(P_1 + P_0\right)\left(V_0 - V_1\right) \qquad \text{(Eq. 1.11)}$$

With Eq. 1.11, and considering that $P_S = -(\partial E / \partial V)_S$, we can write Eq. 1.10 as

$$P_2(V_2) = \left\{1 - \tfrac{1}{2}(\gamma / V_2)(V_1 - V_2)\right\}^{-1}\left\{P_S(V_2) + \frac{\gamma}{V_2}\left[\frac{P_0(V_0 - V_1)}{2} + \frac{P_1(V_0 - V_2)}{2} + \int_{V_0}^{V_2} P_S\, dV\right]\right\} \qquad \text{(Eq. 1.12)}$$

And, with Eq. 1.9, we have

$$\begin{aligned} P_2(V_2) = \{\ 8\ \left[2V_2 + \gamma\left(V_2 - V_1\right)\right]\ \}^{-1} \\ \{\ 8\gamma\ \left[P_0\left(V_0 - V_1\right) + P_1(V_0 - V_2)\right] - 3K_{0S}V_0\ [\ 3\gamma\left(14 - 3K_{0S}^{/}\right)\left(V_0 / V_2\right)^{4/3} \\ + 3\gamma\left(3K_{0S}^{/} - 16\right)\left(V_0 / V_2\right)^{2/3} - 3\gamma\left(K_{0S}^{/} - 6\right) + 2\left(16 - 3K_{0S}^{/}\right)\left(V_0 / V_2\right)^{2/3} \\ + \left(V_0 / V_2\right)^2\left(24 + 3\gamma\left(K_{0S}^{/} - 4\right) - 6K_{0S}^{/} + \left(12K_{0S}^{/} - 56\right)\left(V_0 / V_2\right)^{-2/3}\right)\ ]\ \} \end{aligned} \qquad \text{(Eq. 1.13)}$$

In this analysis, the fact that the elastic precursor is in a state of anisotropic stress does not need to be considered explicitly; only the isotropically stressed final state is important. When there is no elastic precursor, that is, $V_1 = V_0$, and $P_1 = P_0$, this prediction describes the case of single-wave shock compression [63]. The effect of considering the precursor is to increase the thermal pressure $P_{\mathrm{Th}} = P_2 - P_S$ at a given

volume. At $P_2 \sim 150$ GPa in diamond, $P_{Th} \sim 5$ GPa for a 2-wave treatment, compared to a $P_{Th} \sim 2$ GPa for a 1-wave treatment that ignores the elastic precursor. Evidently this is due to the larger energy needed to create the 2-wave system compared to a 1-wave system, for compression to the same final volume. This can be verified by considering that the energy Eq. 1.11 can be re-written as $(E_2 - E_0) = \frac{1}{2} P_2 \left(a V_0 - (1 + a - b) V_2 \right)$, where $a = P_1 / P_2$, $b = V_1 / V_2$ and $P_0 = 0$. For elastic-isotropic states just beyond the HEL, $P_1 \approx P_2$ and $a \approx 1$, while $V_2 < V_1$ and $b > 1$. This results in higher energy for the two-wave case than for the single-wave case in which $a = b = 1$.

Contrastingly, elastic-plastic compression states just above the HEL would exhibit both $P_1 \approx P_2$ and $V_2 \approx V_1$, reducing the Hugoniot energy to values close to the 1-wave value – however, the deformed state will not be under isotropic stress and its temperature is not predicted here. Anisotropic compressions at shock pressures less than the HEL, or elastic-plastic compression states beyond the HEL, require a different approach to calculate shock heating effects [43, 64].

The predicted shock velocity and particle velocity D_2 and u_2 can now be determined from the calculated stress and density, P_2 and $\rho_2 = 1/V_2$, by rearranging the Hugoniot equations 1.4 and 1.5, giving

$$D_2 = \frac{\sqrt{(P_2 - P_1)(\rho_2 - \rho_1)\rho_1\rho_2} - \rho_1^2 u_1 + \rho_1\rho_2 u_1}{\rho_1(\rho_2 - \rho_1)} \qquad \text{(Eq. 1.14.a)}$$

$$u_2 = \frac{\sqrt{(P_2 - P_1)(\rho_2 - \rho_1)\rho_1\rho_2} + \rho_1\rho_2 u_1}{\rho_1\rho_2} \qquad \text{(Eq. 1.14.b)}$$

For inelastic shock-wave velocities $D_2 \geq D_1$, the system will be overdriven and single-wave analogues of Eqs. 1.13 and 1.14 must be used.

For the calculations of P_2, ρ_2, D_2 and u_2 presented here, we have considered the parameters of the elastic precursor P_1, ρ_1, D_1 and u_1 to be fixed at the lowest-stress precursor conditions observed for each crystallographic orientation (shots *dh14* <111>, *dh9* <100>, *dh6* <110>). The uncertainties in the precursor states are not used in the predictions for the sake of clarity. Accounting for the measurement uncertainty in the precursor state, or the scaling of the precursor state with the inelastic-wave state or propagation distance, will somewhat affect the D_2-u_2 predictions, but will not noticeably affect the P_2-ρ_2 predictions. Indeed in P-ρ space (e.g. Fig. 1.11), the predicted hydrostatic Hugoniot is essentially the same regardless of whether a low-stress precursor from <111> or a high-stress precursor from <100> or <110> is used.

The thermodynamic parameters required by our model are K_{0S}, K_{0S}' and γ. We define these parameters in what follows.

The isentropic bulk modulus K_{0S} can be obtained directly from the isentropic elastic constants of diamond at ambient pressure, known most accurately via Brillouin scattering [49], through the relation for a cubic crystal [65] $K_{0S}=(C_{11}+2C_{12})/3$, giving $K_{0S}=444.8$ (± 0.7) GPa. Alternatively, we can obtain K_{0S} from the isothermal bulk modulus obtained from static compression measurements, $K_{0T}=437.5$ (± 8.5) GPa [60], where the subscript T is used to denote isothermal conditions. The relationship between K_{0T} and K_{0S} is [66, 67]

$$K_{0T} = K_{0S}\left(1+\frac{\alpha^2 K_{0S} T}{\rho C_p}\right)^{-1} = \left(1+T\alpha\gamma\right)^{-1} \qquad \text{(Eq. 1.15)}$$

Using the volumetric thermal expansion $\alpha = 3.15\times10^{-6}$ [68], temperature $T = 300$ K, density $\rho = 3515$ kg/m^3, and the specific heat at constant pressure $C_P = 515.5$ J/kg·K [69],

it is found that $K_{0S} - K_{0T}$ = 0.3 GPa. While both measurements are consistent with each other, we use the more precise value of K_{0S} measured by Brillouin, and its uncertainty, in our model.

The Gruneisen parameter $\gamma = \alpha K_{0S}/\rho C_P$. At ambient conditions $\gamma_0 = 0.773$. In our model, as in [63], we assume that the Gruneisen parameter varies with compression in the manner of $\gamma = \gamma_0(V/V_0)$. However, at $P_2 < 400$ GPa, $V/V_0 > 0.7$, and models are not significantly different if we use a constant $\gamma = \gamma_0$.

The first pressure derivative of the bulk modulus under isentropic conditions $K'_{0S} = (\partial K_{0S}/\partial P)_S$ can be determined, as for the bulk modulus K_{0S}, from the measured elastic constants or from isothermal compression measurements, as follows. We have the following relation between $(\partial K_{0S}/\partial P)_T$, the pressure derivative of K_{0S} at constant temperature, and the second- and third-order isentropic elastic constants in a cubic crystal [65, 70]

$$\left(\frac{\partial K_{0S}}{\partial P}\right)_T = -\frac{C_{111} + 6C_{112} + 2C_{123}}{3C_{11} + 6C_{12}} \qquad \text{(Eq. 1.16)}$$

which gives $(\partial K_{0S}/\partial P)_T$ = 4.52 using third-order elastic constants obtained semi-empirically from analysis of Raman data [58]. Isothermal compression experiments have empirically determined $K'_{0T} = (\partial K_{0T}/\partial P)_T$ to range from 3.59 to 4.12 [60]. We can determine K'_{0S} from $(\partial K_{0S}/\partial P)_T$ and $(\partial K_{0T}/\partial P)_T$ with the following selected thermodynamic relations after Spetzler et. al. [67] and Barsch [66]:

$$\left(\frac{\partial K_T}{\partial P}\right)_T = \left(\frac{\partial K_S}{\partial P}\right)_T (1+\alpha\gamma T)^{-1} - \frac{K_S T}{(1+\alpha\gamma T)^2}\left[\gamma\left(\frac{\partial \alpha}{\partial P}\right)_T + \alpha\left(\frac{\partial \gamma}{\partial P}\right)_T\right] \qquad \text{(Eq. 1.17.a)}$$

where

$$\left(\frac{\partial \alpha}{\partial P}\right)_T = -\frac{1}{\alpha K_T}\left(\frac{\partial \alpha}{\partial T}\right)_p + \frac{\gamma \rho}{\alpha K_T^2}\left(\frac{\partial C_V}{\partial T}\right)_P - \frac{\alpha}{K_T} \qquad \text{(Eq. 1.17.b)}$$

$$\left(\frac{\partial K_S}{\partial P}\right)_T = \left(\frac{\partial K_S}{\partial P}\right)_S - \frac{\alpha T}{\rho C_P}\left(\frac{\partial K_S}{\partial T}\right)_P \qquad \text{(Eq. 1.17.c)}$$

and

$$\left(\frac{\partial \gamma}{\partial P}\right)_T = \gamma\left\{\frac{1}{K_S}\left(\frac{\partial K_S}{\partial P}\right)_T + \frac{1}{\alpha}\left(\frac{\partial \alpha}{\partial P}\right)_T - \frac{1}{K_T} + \frac{\gamma T}{\alpha K_S}\left[\alpha^2 + \left(\frac{\partial \alpha}{\partial T}\right)_P\right]\right\} \qquad \text{(Eq. 1.17.d)}$$

The above relations are completely constrained by experimental data, specifically $\left(\partial\alpha/\partial T\right)_P$ = 2x10^{-8} /K^2 [68], $\left(\partial C_V/\partial T\right)_P$ = 3.348 J/kg·K^2 [69], and $\left(\partial K_S/\partial T\right)_P$ = -7.2x10^6 Pa/K [71]. From Eq. 1.17.c, $(\partial K_{0S}/\partial P)_S \approx (\partial K_{0S}/\partial P)_T$, and thus the elastic constants have directly determined K'_{0S} = 4.52 by Eq. 1.16. Using all relations in Eq. 1.17, we obtain $K'_{0S} - K'_{0T}$ = 0.07, and thus K'_{0S} = 3.93 (± 0.27) based on static compression and other empirical thermodynamic data. The value of K'_{0S} obtained from the Raman-based semi-empirical third-order elastic constants is close to, but not consistent with, this value. We use the value derived from static compression and its uncertainty to model the hydrostatic isentrope (Eq. 1.9) and Hugoniot (Eq. 1.13) – except in a particular case that will be discussed.

We note that our model assumes a decrease in γ with increasing pressure and density, which is inconsistent with the positive value of the derivative $\left(\partial\gamma/\partial P\right)_T$ in Eq. 1.17.d at 300 K and ambient pressure. This is due to the large value of $\left(\partial C_V/\partial T\right)_P$ at ambient conditions, resulting from the high Debye temperature of ~1800 K for diamond. At higher temperatures, $\left(\partial\gamma/\partial P\right)_T$ will become negative [72]. In any case, in the

compression range of interest here, small changes in γ have a minor effect on the predicted Hugoniot.

The hydrostatic Hugoniot obtained from the above parameters, and its uncertainty, is presented in Figs. 1.10 and 1.11 for each of the three orientations of diamond studied here. Also shown is the isentropic compression response, which is very nearly equal to the isothermal, or 'cold', compression response, which takes the same functional form as Eq. 1.9 but uses isothermal K_{0T} and $K_{0T}^{/}$ [65].

Another commonly used equation of state to describe materials at large compression is the Vinet EOS. The deviation between the Vinet EOS and the Birch-Murnaghan EOS used in our model, P_{BM}-P_{Vinet}, is about 1-2 GPa at 150 GPa and about 10-20 GPa at 400 GPa. The choice of equation of state is a small source of error in the calculations of the hydrostatic Hugoniot relative to the uncertainties in K_{0S} and $K_{0S}^{/}$, and we do not consider it further.

In the hydrostatic model, as u_2 approaches u_1 and P_2 approaches P_1, it is predicted by Eq. 1.14 that D_2 should approach u_1. Thus D_2 is expected to be as low as ~1 km/s for stresses just in excess of the HEL. Calculating the bulk sound speed $c_B(\rho)=\sqrt{(dP/d\rho)_S}$ from the isentrope (Eq. 1.9), it is predicted that $D_2 < c_B$ until pressures of 300-400 GPa (Fig. 1.10) for an ideal elastic-isotropic response. In contrast, an elastic-plastic material response would imply, for stresses just in excess of the HEL, that $D_2 \approx c_B$ [18]. The phenomenon of shock waves traveling at less than the bulk sound speed has been observed in sapphire and silicon and is correlated with the considerable loss of strength on inelastic shock compression of those materials [18, 52].

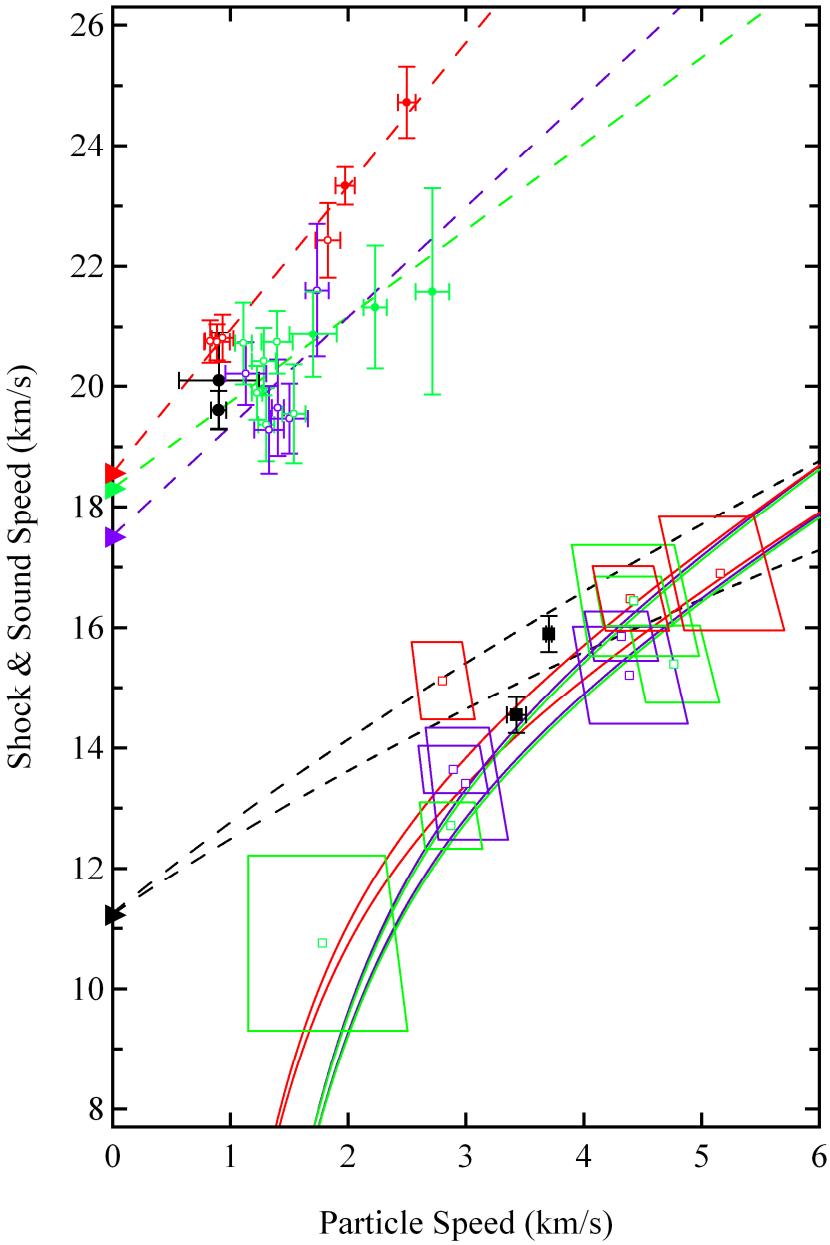

Figure 1.10. *D-u* data for diamond: Elastic-wave (circles) and inelastic-wave measurements (squares). When appropriate, uncertainties are represented by confidence-bounding regions discussed in the text. Data of Kondo and Ahrens [7] are shown as filled black circles and squares. Colored data are new results on <100> (purple), <110> (green), and <111> (red); for colored filled circles, D_1 was estimated as described in the text. Colored dotted lines are linear *D-u* fits to the elastic wave data, centered on the ambient longitudinal sound speeds (colored triangles). Colored solid lines are bounds on the predicted hydrostatic Hugoniot response. Black triangle is ambient bulk sound speed; black dotted lines are bounds on bulk sound speed at high density, plotted against u considering that $u^2 \sim (V_0 - V)$ [73]. Data of Pavlovskii [23] are not shown and are discussed separately in Appendix D.

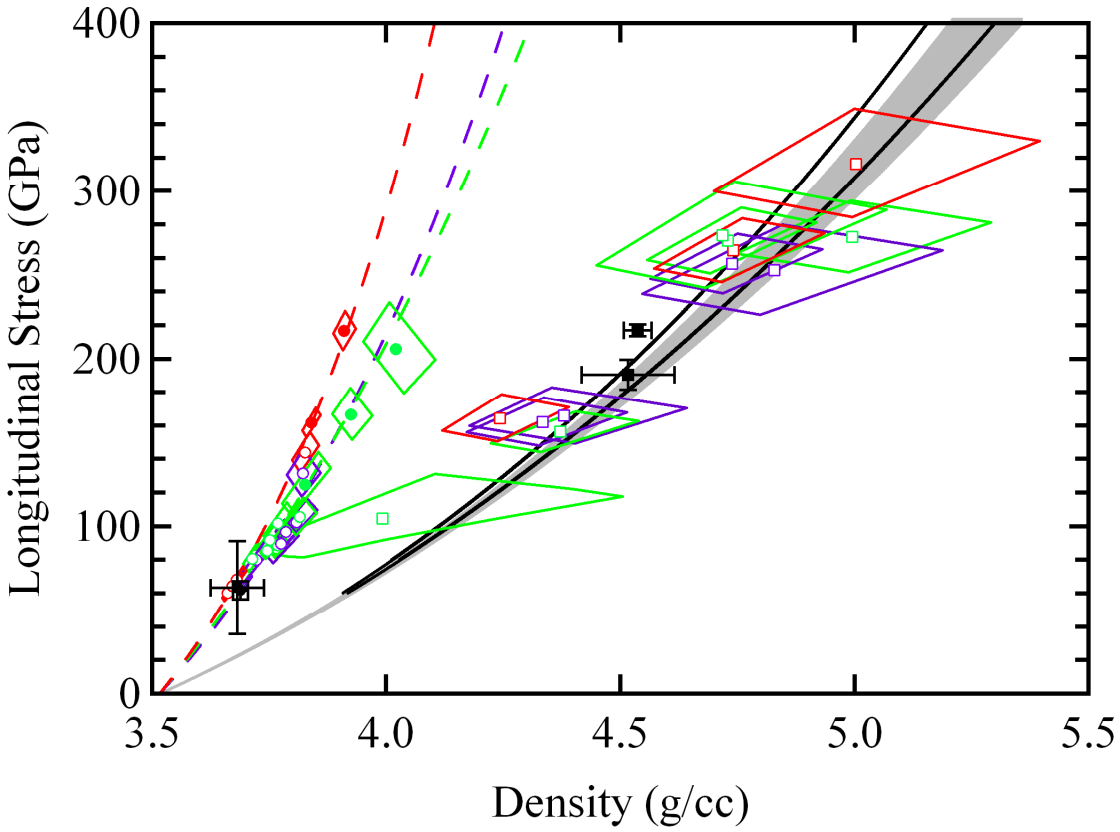

Figure 1.11. Stress vs. density plot for diamond. Symbols and coloration are the same as in Fig. 1.10. In this space, the hydrostatic Hugoniot response is nearly the same regardless of crystallographic orientation; this is given by the black lines, which are the confidence limits of the hydrostatic prediction. The grey region is the predicted isentropic hydrostatic response, which is nearly equal to the isothermal hydrostatic response. Note that the hydrostatic Hugoniot is defined only above the HEL.

Discussion:

Elastic precursor observations:

The elastic precursor measurements show a significant variation with orientation. At low final stresses, the <100> and <110> orientations exhibit precursors of similar stresses and shock velocities, while the <111> orientation exhibits precursors of lower stress and significantly faster shock velocity. The <100> and <110> precursors appear to scale more strongly in amplitude with final stress than the <111> orientation, at least initially (Fig 1.11). However, at high stress, the velocities of the <111> and <100> precursors increase substantially, while the velocity of <110> appears to remain relatively constant (Fig 1.10); this conclusion remains valid even if the precursor data based on elastic Hugoniot extrapolations is ignored. This effect may have been observed in molecular dynamics simulations on the <110> orientation [74].

It is observed that the scatter in the data from the <100> and <110> orientations is considerably more pronounced than for the <111> orientation (Fig 1.10); this could be a manifestation of sample-to-sample variation in crystallographic orientation relative to the shock propagation direction which, as discussed earlier, may have been larger for <100> and <110> oriented crystals.

The elastic-precursor data collected here compares well with that observed in previous studies. Kondo and Ahrens [7] reported a precursor with P_1=62 (± 5) GPa for final stress P_2=217 (± 4) GPa in nearly-<111>-oriented diamond, comparing well with the precursors of P_1=65 (± 8) GPa observed here for <111>-oriented samples that reached

the similar final-stress conditions. In <110>-oriented diamond, Knudson et. al. [24] observed precursors with P_1=95 (± 5) GPa for final stresses P_2=225 (± 25) GPa, comparing well with precursor stresses of P_1=91 (± 9) GPa measured here at similar final stress. Zybin et. al. [75] found a precursor of P_1=125 (± 15) in the <110> direction with molecular dynamics techniques; however, the final stress obtained in that study is not clear and thus we can not make a direct comparison with the present results.

We take the Hugoniot elastic limits of diamond to be best represented by the weakest elastic precursor observed in each orientation, considering that yielding of diamond on increasing stress is coincident with the first formation of the two-wave structure. These are $P_{HEL}^{<100>}$=80.1 (± 12.4) for the <100> orientation, $P_{HEL}^{<110>}$=80.7 (± 5.8) for the <110>, and $P_{HEL}^{<111>}$=60.4 (± 3.3) for the <111>. It would be misleading to refer to all elastic precursors as 'elastic limits', as is common in the literature, since precursor stresses in some cases exceed the HEL by more than a factor of two. As we did not observe the transition from a single-wave structure to a two-wave structure in these experiments, the actual HEL values may be somewhat lower than reported above; however, given the scaling of precursor stress with final stress, this overestimation should be on the order of the uncertainty.

The elastic-wave data presented here also provide the first measurements of the elastic Hugoniots of diamond. The evaluation of elastic Hugoniots based on the measurements is discussed in more detail in Chapter 2, but the results are briefly summarized as follows.

Work on other high-strength brittle solids suggests that a functional form based on material elasticity at finite strain is appropriate for describing elastic Hugoniots [41, 46,

57]. We find that such finite-strain models, based on independent measurements of the second- and third-order elastic constants of diamond [49, 58], describe the present elastic wave data on diamond, but in general, only when expanded to fourth order in strain. Thus, descriptions of the diamond elastic Hugoniots based on third-order expansions [44] are not entirely consistent with all the available data. The finite strain models imply a nonlinear trend in *D*-*u* space, centered on the ambient-pressure longitudinal sound speeds; in this chapter, however, we have shown only linear fits in *D*-*u* space, centered on the ambient sound speeds (Figs. 1.10 - 1.12) as these are simple guides to the eye for representing the elastic wave data.

Observations of inelastic shock states:

As for elastic compression, the response of diamond to inelastic compression depends on the shock-propagation direction.

In *D-u* space (Fig 1.10), the inelastic shock response in each orientation is expected to be anisotropic, since, as shown for the predicted hydrostatic Hugoniots, the shock and particle velocity D_2 and u_2 vary with the conditions of the elastic precursor for conditions of similar P_2 and ρ_2. Consequently, a direct comparison between the compressional response of each orientation is not possible in *D-u* space. However, by considering the deviation from or agreement with the predicted hydrostatic responses, there does appear to be some orientation dependence in the final compression states. While the <100> and <110> orientations agree well with the hydrostatic response, the <111> data is significantly offset, at least at low stress. The hydrostatic response is a prediction of the slowest velocity possible for the inelastic shock in diamond, and any waves exhibiting finite strength will travel faster than this. This is consistent with the observations, with velocities either in agreement with the hydrostatic predictions or faster. Shock velocities D_2 in the <111> orientation are comparable to the bulk sound speed $c_B(\rho_2)$, while the shock velocities in the <100> and <110> orientations are significantly less than the bulk velocity.

In *P-ρ* space (Figs. 1.11 and 1.13), the deviation from the hydrostatic response, and between different data, is not as pronounced as in *D-u* space. Fig. 1.13 shows the most precise measurements on the inelastic wave conditions, at $P_2 \sim 150$ GPa. As observed in *D-u* space, the <110> and <100> data agree with the hydrostatic predictions

while the <111> response is significantly offset. However, given the uncertainties in the measurements, it is possible that all orientations display an identical stress-strain response that is offset from the hydrostatic Hugoniot due to finite strength behind the inelastic wave. It is also possible that the compression response differs considerably in each orientation; for example, it is possible that the <100> and <110> orientations show a hydrostatic shock response, but this is not possible for the <111> orientation. Additional evidence for such an anisotropic P-ρ response will be considered below.

At u_2 > 4 km/s and P_2 > 250 GPa, data on all orientations agree with the hydrostatic predictions, however, the considerable uncertainties in this regime make it impossible to assess any finite strength effects.

The only previous Hugoniot data on diamond in which the two-wave structure was observed and accounted for in the analysis was obtained by Kondo and Ahrens [7], whose results are shown in Figs. 1.10-1.13. One datapoint in that study is clearly offset from the hydrostatic predictions, while one is in agreement. The data of Pavlovskii, for which no two-wave structures were observed, is less easy to compare to the present results, as discussed below and in Appendix D.

In conclusion, the orientations of diamond that show a definite offset from hydrostatic behavior are <111> diamond (this study), and nearly-<111> oriented diamond (Kondo and Ahrens [7]).

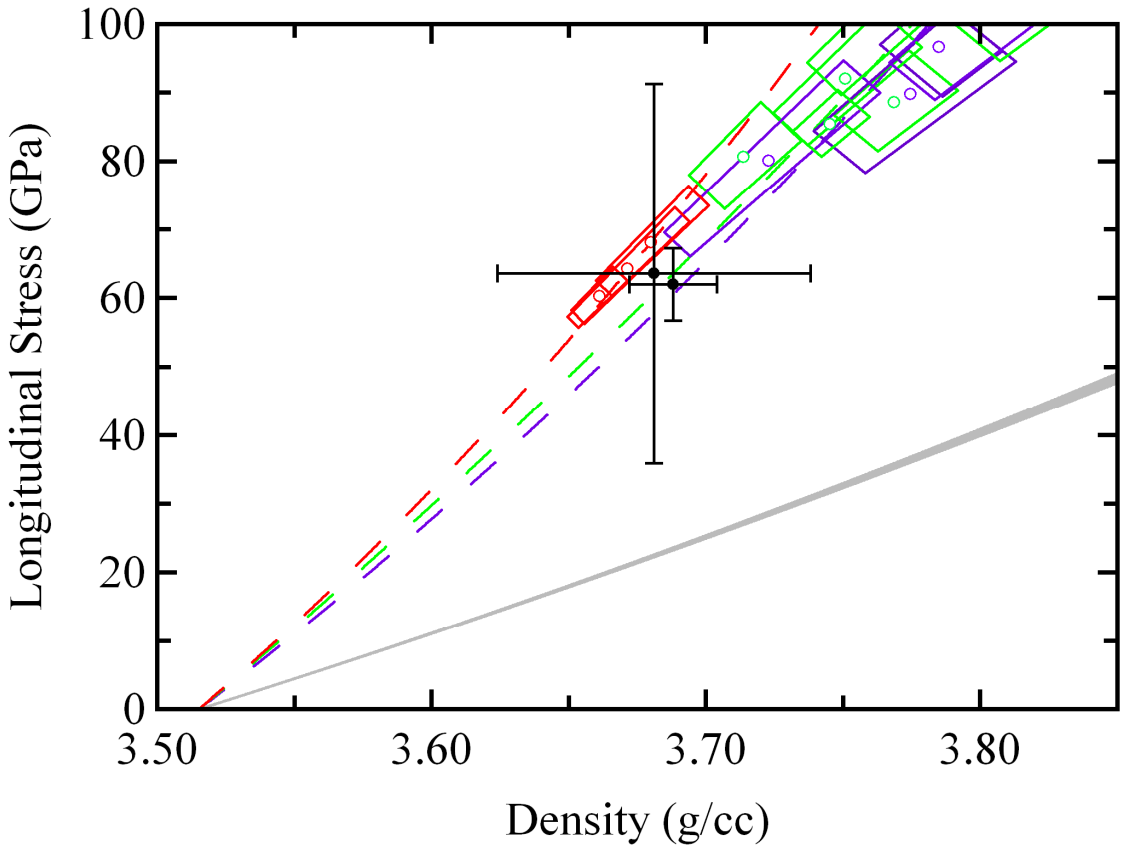

Figure 1.12. Close-up of the lowest-stress elastic precursors observed in the present study. Symbols, lines and coloration are the same as in Fig. 1.11. The lowest-stress precursors are taken to be equal to the HEL for each orientation. The deviation of these data from the hydrostatic isentrope (grey) is related to the maximum shear stress that can be supported in diamond without failure.

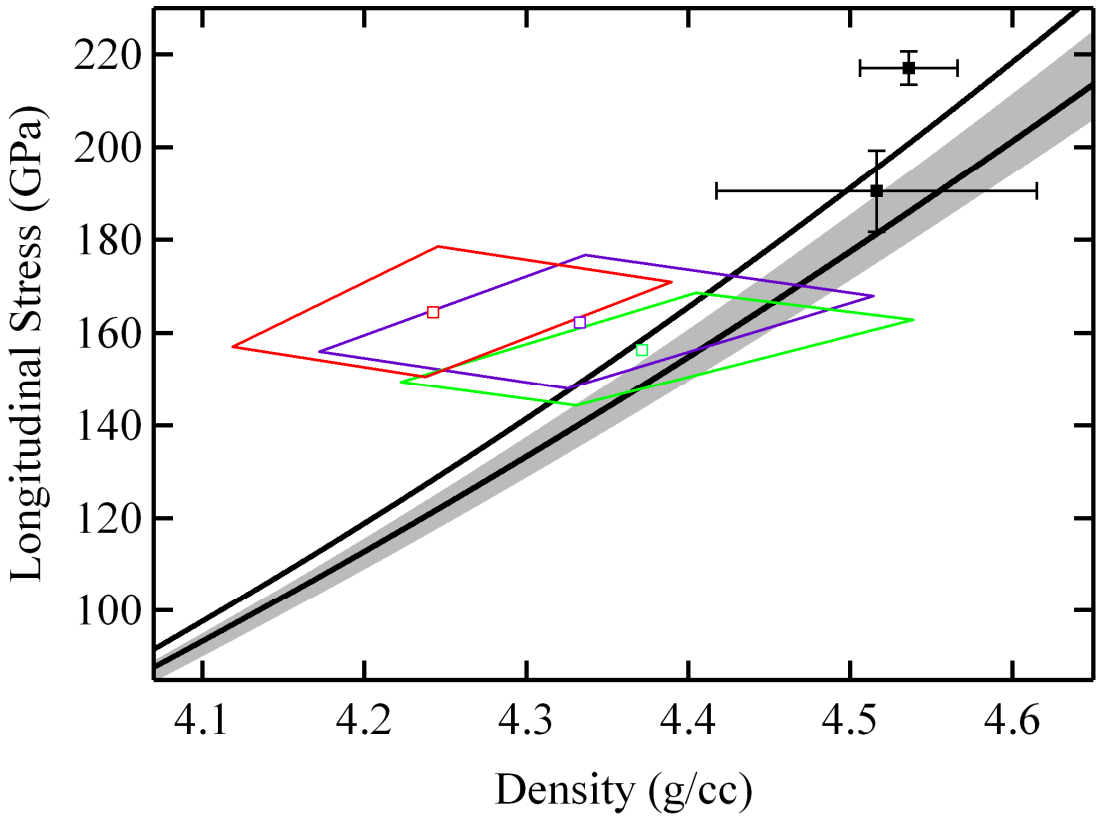

Figure 1.13. Close-up of the inelastic-compression regime that shows a clear deviation from hydrostatic response. Symbols, lines and coloration are the same as in Fig. 1.11. Three of our datapoints (with the smallest uncertainty) are shown, together with the original measurements of Kondo and Ahrens. Two datapoints show a distinct offset from the hydrostat: our shot on <111> diamond and Kondo and Ahrens' shot on nearly-<111> oriented diamond. We conclude from these measurements that, at the very least, the <111> orientation exhibits finite strength under inelastic compression.

The yield strength of diamond:

The available data provide significant information on the strength of diamond under the application of dynamic stress. This information is in two categories: the strength of diamond under elastic loading (that is, the yield point on the elastic Hugoniot or the HEL), and the strength retained during yielding.

The deviation between the measured longitudinal shock stress $P(V)=\sigma_x(V)$ and the hydrostatic pressure at the same volume $P_H(V)$, will be called the shear stress offset, after [18]

$$\sigma_\tau(V) \equiv \sigma_x(V) - P_H(V) \qquad \text{(Eq. 1.18)}$$

The shear-stress offset is directly measured in the present study, as illustrated in Figs. 1.12 and 1.13.

It is assumed in Eq. 1.18 and subsequent analysis that the thermal pressure is equivalent in the two states being compared, such that the stress offset can be attributed entirely to strength effects. Deviations from this assumption are expected to be small in the case of diamond, as will be discussed.

The mean pressure of the shocked system is defined as

$$\overline{P}(V) \equiv \tfrac{1}{3}\left(\sigma_x(V)+\sigma_y(V)+\sigma_z(V)\right) \qquad \text{(Eq. 1.19)}$$

Where σ_y and σ_z are the lateral stresses along principal stress axes. In the case of laterally isotropic stress, $\sigma_y = \sigma_z$, while for laterally anisotropic stress $\sigma_y \neq \sigma_z$. Finite strain compression models for a cubic crystal (Chapter 2) indicate that under purely elastic, uniaxial strain, the lateral stresses are isotropic for <100> and <111> compression, but not for <110>. The deviatoric stresses are defined as

$$\sigma_i^{/} \equiv \sigma_i(V) - \overline{P}(V) \qquad \text{(Eq. 1.20)}$$

where i is one of the principal axes of stress x, y or z.

For a linear-elastic, elastically-isotropic material, the mean stress $\overline{P}$ (V) in an anisotropically stressed system is equal to the hydrostatic pressure P_H(V) at the same volume and temperature [19]. However, this is not obviously the case for elastically anisotropic and nonlinear materials such as diamond. Thus we explicitly consider the deviation between the mean stress and the hydrostatic stress ΔP, given by

$$\overline{P}(V) - P_H(V) \equiv \Delta P(V) \qquad \text{(Eq. 1.21)}$$

The maximum shear stress in an anisotropically stressed system is

$$\tau_{\max} = \begin{cases} \frac{1}{2}(\sigma_x - \sigma_y) \equiv \tau_{\max}^{y} & (\sigma_y > \sigma_z) \\ \frac{1}{2}(\sigma_x - \sigma_z) \equiv \tau_{\max}^{z} & (\sigma_z > \sigma_y) \end{cases} \qquad \text{(Eq. 1.22)}$$

where $\tau_{\max}^{y}$ and $\tau_{\max}^{z}$ are the maximum shear stresses in the x-y and x-z planes, respectively (x continues to identify the shock-propagation direction). The maximum shear stress occurs at an angle of 45 degrees to the shock-compression direction.

We rewrite Eq. 1.19 as

$$\sigma_x(V) - \overline{P}(V) = \frac{4}{3}\left(\frac{\tau_{\max}^{y}(V) + \tau_{\max}^{z}(V)}{2}\right) = \frac{4}{3}\tau_{\max}^{ave}(V) \qquad \text{(Eq. 1.23)}$$

The average shear stress, $\tau_{\max}^{ave}$, is equal to $\tau_{\max}^{y} = \tau_{\max}^{z}$ for the case of laterally isotropic stress.

Combining Eqs. 1.18, 1.21 and 1.23,

$$\sigma_\tau = \sigma_x(V) - P_H(V) = \tfrac{4}{3}\tau_{\max}^{ave}(V) + \Delta P(V) \qquad \text{(Eq. 1.24)}$$

As the system is shocked through its HEL, yielding begins. The maximum shear stress within a material at this yielding point, $\tau_{\max}^{ave}(V_{HEL})$, is the largest that can be sustained by the material before inelastic deformation occurs. For inelastic compression states beyond the HEL, the shear stresses may be maintained (as in the elastic-plastic model), relaxed (as in the elastic-isotropic model) or varied with increasing pressure, as in, for example, the model of Steinberg and Guinan [76].

The magnitude of these strength effects can be examined in terms of the yield strength *Y*, given by the von Mises criterion

$$Y = (3/2)^{1/2}\left(\sigma_i^{/}\sigma_i^{/}\right)^{1/2} \qquad \text{(Eq. 1.25)}$$

For laterally isotropic stress, this reduces to

$$Y = 2\tau_{\max} \qquad \text{(Eq. 1.26)}$$

For laterally anisotropic stress,

$$Y = 2\tau_{\max}^{ave}\left(\frac{3(\sigma_y^{/})^2 + 3(\sigma_z^{/})^2 - 6\sigma_y^{/}\sigma_z^{/}}{16(\tau_{\max}^{ave})^2} + 1\right)^{1/2} \equiv 2\tau_{\max}^{ave}\Delta L \qquad \text{(Eq. 1.27)}$$

where the term ΔL accounts for the difference between the lateral deviatoric stresses. The yield strength can be evaluated at conditions of incipient yielding ($V=V_{HEL}$) or at conditions where yielding has occurred ($V<V_{HEL}$).

Two unknowns emerge from the preceding discussion: the difference between hydrostatic and mean pressure at a given volume, ΔP, and the difference between the deviatoric stresses $\sigma_y^{/}$ and $\sigma_z^{/}$ for laterally anisotropic stress systems, parameterized by ΔL, which applies specifically to the case of case of <110> diamond.

In the case of elastic strain, these terms can be calculated using finite strain models, as discussed in Chapter 2, which predict the longitudinal and lateral stresses at the condition of maximum elastic strain, the HEL. Lagrangian and Eulerian third-order uniaxial strain models were examined, using the isentropic second- and third-order elastic constants of diamond discussed previously. The hydrostat was calculated as a third-order Birch-Murnaghan isentrope (Eq. 1.9), with K_{0S} and K'_{0S} derived from the elastic constants (e.g. Eq. 1.16) for self-consistency in the calculations. The calculations for <110> diamond are shown in Fig. 1.14. At the elastic strain corresponding to the HEL in each orientation, it is found that $\Delta P_{HEL}^{<100>}$ =0.3 to -0.5 GPa, $\Delta P_{HEL}^{<110>}$ =2.4 to 0.2 GPa, and $\Delta P_{HEL}^{<111>}$ =0.9 to 0.5 GPa, where the range is due to the differences between Eulerian and Lagrangian finite strain predictions. The magnitudes of these are relatively small given the typical uncertainties in stress here. For <110> diamond, $\Delta L_{HEL}^{<110>}$ =1.003, which is entirely negligible. However, it is clear that despite using self-consistent elastic constants and strain-energy expansions to the same order in strain, the terms ΔP and ΔL are finite at all but infinitesimal strain conditions.

For inelastic strain states behind the second shock, the characterization of ΔP and ΔL is less straightforward. However, inasmuch as the HEL corresponds to the maximum deviatoric stresses possible in either an elastically-strained or inelastically-strained system (to first order), we conclude that the magnitudes of ΔP and ΔL predicted at the HEL should represent the maximum possible for inelastic strain-states as well. This interpretation ignores the possibility of increasing yield strength with work-hardening or stress, which is often observed in metals [77]. However, for diamond this is not likely, as

the offset of inelastic-wave states from the hydrostatic response is never significantly larger than the offset observed at the HEL.

It is worth noting that to accurately describe the finite-strain response of diamond under uniaxial strain conditions, fourth-order elastic models are needed (Chapter 2). However, fourth-order elastic constants are not known in their entirety, precluding the use of fourth-order models to fully predict ΔP and ΔL. The effect of using only third-order models is considered minor for the purposes of the present analysis.

Elastic Yield Strength:

The yield strength of diamond, determined by the point of yielding on the elastic Hugoniot (the HEL), is the point at which deformation occurs in the form of fracturing, plasticity or other inelastic processes. This form of strength has been studied extensively for diamond [9-16]. For example, the quasi-static yield strength and failure limit of diamond has been of longstanding interest to researchers using diamond-anvil cell technology to study matter in static-compression experiments [12, 16, 78].

We evaluate the elastic yield strength of diamond by comparing the isentropic hydrostatic response predicted by Eq. 1.9 with the HEL in each orientation (Fig 1.12). This is reasonable since elastic loading should be nearly isentropic. Under isentropic conditions, the thermal pressures are very small, and hence the difference between a uniaxial-strain isentropic state and a hydrostatic isentropic state can be attributed entirely to strength effects.

Based on the present measurements, the elastic (compressive) yield strengths are $Y_{EL}^{<100>}$=78 (± 16) GPa, $Y_{EL}^{<110>}$=78 (± 12) GPa, and $Y_{EL}^{<111>}$=60 (± 5) GPa. The yield strengths for these orientations are a significant fraction of the ambient shear modulus of

553 GPa [8], as is common in brittle solids [21]. As with the HEL, the inferred shear strength is strongly orientation dependant, suggesting that it is not appropriate to define a single yield strength for diamond, and that the yield strength depends on the configuration of loading. This anisotropy is to be expected because failure in diamond usually occurs preferentially along (111) planes, with each loading configuration providing a different combination of shear and normal stress to these planes. There is no direct analog to uniaxial strain in most technological applications: thus, different yielding limits can be expected under the stress conditions achieved in other experiments.

The critical shear stress along the (111) plane of diamond has been calculated from interatomic force models by Tyson [9] and Kelly et. al. [10], who found values of τ_{max}=91.6 and τ_{max}=121 GPa, respectively. First-principles methods have also been used to determined the critical shear stress along the (111) plane; Chacham and Kleinman [13] found τ_{max}=95 to 108 GPa for normal stresses from 0 to 50 GPa; Roundy and Cohen [14] predicted τ_{max}=93 GPa. Zhao et. al. [12], using first principals methods, found Y_{EL}~200 GPa for compression in the <100> direction. The yield strengths Y_{EL} thus obtained range from 180 to 240 GPa. This is significantly larger than we have measured, which may not be surprising as real diamonds contain defects.

The only other experimental determination of the shear strength of diamond was made by Eremets et. al. [16], who estimated Y_{EL}~120-140 GPa based on plastic deformation of diamond-anvil tips. While somewhat larger than our values, the configuration of loading in that study differs significantly from that in our measurements. Specifically, the strength inferred for diamond tips subjected to > 100 GPa stresses over very small spatial regions (in this case, about 10 μm in diameter and a few μm thick), is

not necessarily the strength of diamond stressed over its bulk and over much larger spatial regions (as in the present study, where the stressed region is two orders of magnitude larger). Scale-dependant strength of diamond has been observed previously, for example in the observed higher strength of small diamond grains and small loaded areas over large ones [8].

Finally, it is possible that third-order finite-uniaxial-strain models, used previously to constrain ΔP and ΔL, could be used to calculate directly the elastic shear strength of diamond by comparing the measured longitudinal stress at the HEL to the lateral stresses predicted by finite-strain models [11], as an alternative to the comparison to the hydrostat used earlier. This gives yield strengths in accord with the strengths determined by Eq. 1.24 and 1.27.

Inelastic Yield Strength:

For states that have been inelastically deformed beyond the elastic limit, the strength will be referred to as the inelastic yield strength, Y_{IN}. This characterizes the resistance of inelastically deforming systems to total shear-stress relaxation. In a simple elastic-plastic model, $Y_{IN}=Y_{EL}$ for all deformation states; whereas $Y_{IN}=0$ in the elastic-isotropic model. Of course, Y_{IN} is likely to depend on strain rate, and hence the timescale of any given experiment.

In our measurements, the most useful regime of inelastic compression to examine is between 100 and 200 GPa, where our measurements are most precise (Fig. 1.13). The most precise datum for each orientation is shown in Fig. 1.3, with the hydrostatic Hugoniot prediction, and the strength is taken from Eqs. 1.24 and 1.27. At a stress $P_2 \sim$

150 GPa, we find that $Y_{IN}^{<100>}$ = 0 to 72.3 GPa, $Y_{IN}^{<110>}$ = 0 to 47.6 GPa and $Y_{IN}^{<111>}$ =11.4 to 90.1 GPa.

It is reasonable to expect that the thermal pressure in the actual shocked state will be somewhat different from that on the hydrostatic Hugoniot at the same volume. However, given the relatively small magnitude of the thermal pressure on the hydrostat at the compressions considered above, we conclude that even relatively large differences in thermal pressure would not seriously affect our estimates of the inelastic yield strength. The range of uncertainty depends on the precision of our measurements, given by the confidence-bounding regions, the uncertainty in the hydrostatic Hugoniot, and the range of possible ΔP, including ΔP=0.

The magnitude of the inelastic strength is made clearer by comparing the inelastic shear strengths Y_{IN} with those inferred from the HEL Y_{EL}. For <111> compression, the strength seen in the deformation wave is 165 to 17% of the strength seen at the HEL, while for <110> the strength in the deformation wave is 72 to 0% of the strength seen at the HEL. The <111> orientation thus displays a retention of strength in the inelastic response, while whereas the <110> orientation displays some loss of strength. The data on the <100> orientation are too imprecise to constrain a loss or retention of strength.

Given the uncertainties in strength measurement, it is plausible that all orientations retain finite strength under inelastic compression, though an ideal elastic-plastic response is ruled out; it is also plausible that <100> and <110> display an ideal elastic-isotropic shock response whereas <111> exhibits an ideal elastic-plastic response. More precise measurements, as well as a closer examination of wave profiles, are needed to further understand the strength response of diamond in each orientation.

The structure of the free surface wave profiles provides qualitative evidence for an anisotropic strength response under inelastic compression. It has been noted that at P_2 ~ 250 GPa, the free-surface reverberation due to the elastic precursor in <100> and <110> diamond shows evidence for interaction with a sharp, discontinuous second shock, while the <111> reverberation shows evidence of interaction with a broader second-shock. A large loss of strength in the inelastic wave for the <100> and <110> orientations would be consistent with shear banding, rapid stress relaxation at the shock front, and a sharp shock. A retention of strength in the <111> orientation is compatible with a plastic deformation wave with a longer risetime. Thus, it is likely that the form of the free-surface reverberation is related to the strength response – and mode of strength loss – in the second wave. At lower stress (P_2 ~ 150 GPa), the lack of a leading reverberation all wave profiles, even in orientations that show evidence for strength loss, could be related to the dispersion of the inelastic compression wave due to significantly lower shock speeds than bulk sound speeds (Fig. 1.10).

The datum from Kondo and Ahrens [7] that shows a distinct offset from the hydrostat (Fig 1.13) implies a shear strength Y_{IN} =11.3 to 42.3 GPa. The other datum is consistent with this result within its uncertainty. As the direction of shock propagation in their experiments was close to the <111> direction, and since those experiments exhibited elastic precursors of similar amplitude to those observed in the present study in the <111> direction, we conclude that the finite inelastic yield strength in that experiment is consistent with our observations on the <111> orientation.

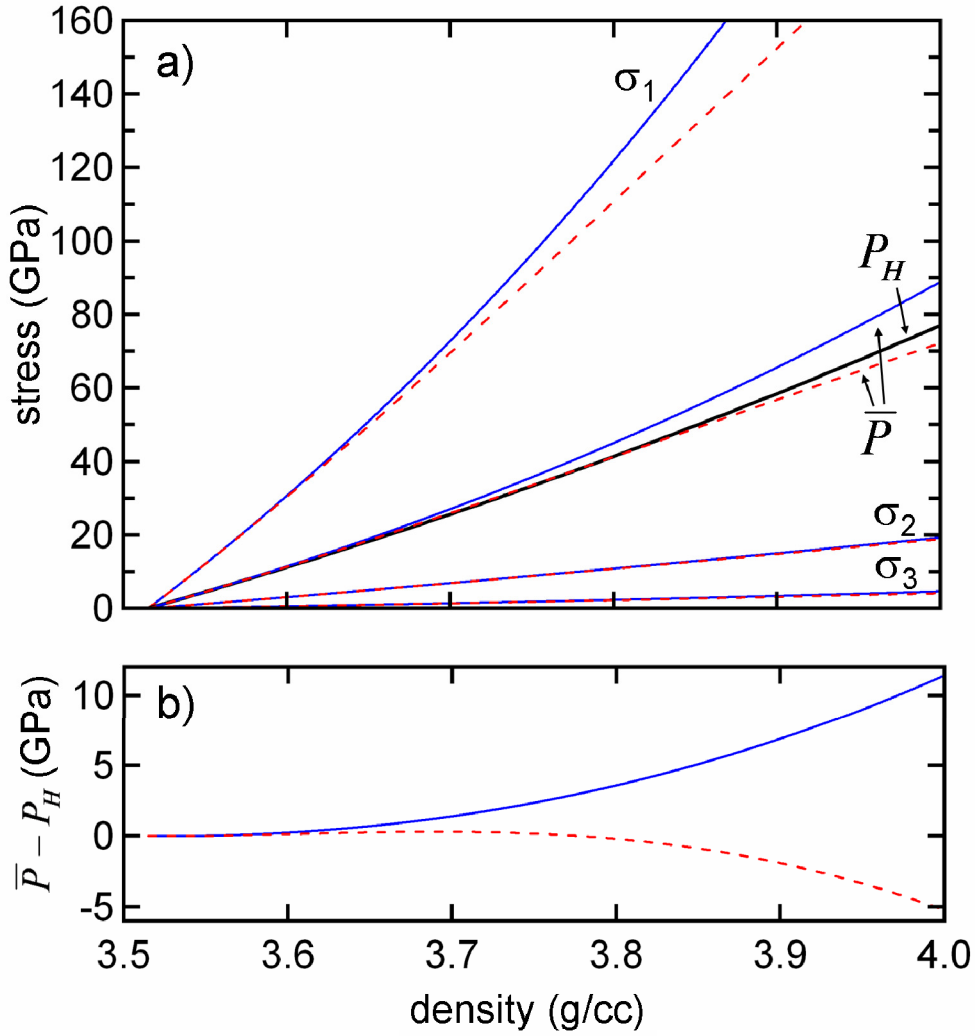

Figure 1.14. a) Finite Strain Calculation for <110> diamond. Blue solid curves are the results of the Eulerian formalism and red dotted curves use a Lagrangian formalism. The hydrostatic isentrope, with the parameters set to be consistent with the second- and third-order elastic constants, is show as a black solid line (P_H). The mean stress $\overline{P}$ computed for each formalism are shown with the same color as the principal components of stress σ_1, σ_2, and σ_3. b) $\Delta P = \overline{P} - P_H$ for the Lagrangian and Eulerian formalisms. The HEL occurs at ~3.75 g/cc in density and ~80 GPa in stress σ_1; this point does not lie on the predictions of σ_1 due to inaccuracy in the third-order finite strain models.

Limit of the 2-wave structure in diamond:

The two-wave structure in diamond is observed to persist to several hundred GPa. It is of interest to consider at what final stress the elastic precursor will be overdriven and only a single, inelastic shock will form.

We can estimate the absolute minimum overdrive stress on the Hugoniot by considering the minimum precursor amplitudes observed in this study. That is, for an experiment of long duration (or 'infinite-run'), the elastic precursor should decay to a minimum amplitude close to the HEL. Overtake is defined to occur when the inelastic wave velocity D_2 rises to equal D_1. Comparing the minimum D_1 values measured in each orientation with the hydrostatic Hugoniot predictions for D_2, we estimate the two-wave structure will persist to at least ~450 GPa for all orientations in an infinite-run experiment.

This has implications for the previous measurements by Pavlovskii on the <100> orientation [23]. Our measurements on this orientation suggest that the three lowest-stress experiments of Pavlovskii were likely to have contained elastic precursors that were apparently not observed. This is reinforced by the fact that all three experiments exhibited shock velocities less than the ambient longitudinal sound speed in the <100> orientation. The error incurred by not including the two-wave structure in the data reduction would have been substantial. In appendix D, we consider the magnitude of these errors.

It is clear from our measurements that shorter-duration experiments exhibit much faster precursors and that the two-wave structure can persist to at least several hundred GPa beyond the lower limit described above. Given the high precursor shock velocities

predicted for CVD, nearly-<111> oriented polycrystalline diamond, overtake could occur as high as 1 TPa or more. Beyond 600 GPa, it is possible that a two-wave structure will exist with a transparent elastic precursor followed by a strongly reflecting second wave in the molten carbon regime [6].

Conclusion:

The shock response of diamond is anisotropic for compression in three primary directions <100>, <110> and <111>. For elastic compressions, the elastic limits vary with orientation, as do the elastic Hugoniots. For inelastic compression, it is observed that strength is at least partially lost in the <110> orientation, whereas strength is at least partially retained in the <111> orientation. The free-surface wave profiles of diamond also vary significantly with orientation, suggestive of a longer risetime of the inelastic wave in the <111> orientation and a different mode of inelastic deformation, compared to <100> and <110>.

The different inelastic responses in each orientation could be related to the balance between the potential energy available for release in the inelastic wave and the tendency for thermal heterogeneities to dissipate due to the high lattice thermal conductivity of diamond. Specifically, the <111> orientation has a smaller potential energy $P_1[V_1 - V_H(P_1)]$ than the <110> and <100> orientations by virtue of its lower HEL and (initially) weak scaling of precursor amplitude with final stress (where $V_H(P_1)$ is the hydrostatic Hugoniot volume at pressure P_1). Thus, the rate of potential-energy conversion to heat in the inelastic shock front could be reduced in the <111> orientation, and dissipation of thermal heterogeneities therefore more efficient, resulting in higher residual strength and a more plastic deformational response.

Based on the present measurements, we find the observation of only single-wave structures in the work of Pavlovskii on <100> diamond [23] to be concerning. Equation-of-state models [6, 79] based on the original shock-wave data of Pavlovskii may be in

need of re-evaluation. The 2-wave structure in diamond persists to final stresses of at least ~450 GPa, and possibly much higher depending on experimental timescales. Given the strength effects present in diamond to these stresses, shock-wave data may not be easily integrated into equation-of-state models for carbon. Several attempts have been made to simulate the shock Hugoniot of diamond using first-principles techniques [36, 37]; however, quantitatively predicting dynamic strength effects remains a challenge for theory.

Chapter 2:

Descriptions of elastic Hugoniots by finite strain theory.

Abstract:

Finite strain theory is developed for the specific case of uniaxial strain in spatial (Eulerian) and material (Lagrangian) strain, and these formulations and compared with uniaxial strain compression data from elastic shock-wave measurements. Even at the relatively small uniaxial strain relevant to shock-wave measurements, a few percent in volume, it is found that these two treatments are not equivalent. While the Eulerian treatment is preferred for representing hydrostatic compression measurements, we find that, at present, the available data on uniaxial strain do not warrant selection of one strain formulation of another. Future high precision measurements may be able to distinguish whether one strain formulation is preferable for describing conditions of finite uniaxial strain.

Introduction:

Shock compression initially generates a state of bulk uniaxial strain in a material. When the strength of the substance has not been exceeded, uniaxial strain is purely elastic. When strength is exceeded, bulk uniaxial strain is at least partially compensated by flow at microscopic to macroscopic scales that relaxes the anisotropic stress state toward one of isotropic or hydrostatic stress. This chapter deals with the former case of purely elastic shock compression.

Here, the physical theories commonly used to treat finite strains are examined in the particular context of uniaxial strain. These theoretical models will then be compared to existing elastic shock wave data on diamond, sapphire, and quartz.

With static compression techniques, purely uniaxial strain has been achieved in materials to axial stresses on the order of a GPa, before experimental difficulties in laterally confining samples and crystal failure prevent further examination of this ideal stress-strain configuration [80]. Shock compression, on the other hand, generates nearly ideal uniaxial-strain states with axial stresses up to the 100 GPa level, as failure and shear stress relaxation are inhibited on the timescale of the experiment by rapid loading and observation. Given the large volumetric strains generated by this technique, on the order of several percent, a description of the stress-strain response of such systems must include the effects of finite strain, as opposed to the infinitesimal strain assumptions of linear elasticity.

Although a Lagrangian finite-strain approach is often used to analyze compression measurements under large uniaxial strain [41, 44, 46, 57, 81, 82], it has been empirically established that an Eulerian finite-strain formulation is more consistent with measurements of large isotropic strains. Specifically, the Eulerian approach has been found to be a better representation of experimental equations-of-state obtained from quasi-hydrostatic compression with devices such as the diamond-anvil cell, and shock compression of solids well beyond the elastic limit [65, 83-86]. Here we compare Eulerian and Lagrangian analyses of elastic shock-wave measurements to determine whether one formulation is preferred over the other when treating conditions of uniaxial strain.

In an elastically isotropic material with strength, such as a glass [57], ideal uniaxial strain can be generated in any arbitrary direction. In crystalline materials, ideal uniaxial strain is possible only in certain directions permitted by crystal symmetry to

contain pure longitudinal compression modes. It has been shown that pure longitudinal nonlinear elastic modes exist along any rotational symmetry axis for any crystal symmetry class [43]. In other, nonspecific directions, modes may be quasi-longitudinal and quasi-shear, which significantly complicates measurement and theory. Pure-longitudinal mode directions are frequently studied in elastic shock experiments, and thus provide the an ideal and extensive dataset with which to examine different finite-strain formulations.

Some of the results described in this chapter have been covered in part by previous studies. Of note is Nielson [70], the only previous researcher to have considered Eulerian finite strain for a system under uniaxial strain – coincidentally diamond, the subject of Chapter 1 of this thesis. He noted that the Eulerian approach was superior to the Lagrangian in describing the stress-strain response under both isotropic and anisotropic strain conditions, in the sense that it described the results of his first-principles calculations accurately over a larger compression range. Now that experimental results are available from elastic shock waves in diamond, as presented in Chapter 1, we seek to revisit his observations.

Finite strain theory of elasticity:

Following the approaches of Birch [65, 83], Thurston [82], Wallace [87], Fowles [46] and others, homogeneous uniaxial strain takes an initial (unstrained) point in the system located at a_I=(a_1, a_2, a_3) to a new position at x_i=(x_1, x_2, x_3) with subscripts 1, 2 and 3 enumerating a Cartesian coordinate system. The spatial (or Eulerian) coordinates x_i

will be referenced with lowercase subscripts, and the material (or Lagrangian) coordinates a_I will be referenced with uppercase subscripts, after Wiener [88].

The Jacobian, J, relating initial to final coordinates is

$$J \equiv \begin{vmatrix} \frac{\partial x_1}{\partial a_1} & \frac{\partial x_1}{\partial a_2} & \frac{\partial x_1}{\partial a_3} \\ \frac{\partial x_2}{\partial a_1} & \frac{\partial x_2}{\partial a_2} & \frac{\partial x_2}{\partial a_3} \\ \frac{\partial x_3}{\partial a_1} & \frac{\partial x_3}{\partial a_2} & \frac{\partial x_3}{\partial a_3} \end{vmatrix} = \frac{\rho_0}{\rho} \qquad \text{(Eq. 2.1)}$$

where ρ is strained density and ρ_0 is the initial (unstrained) density.

The Lagrangian (material) and Eulerian (spatial) strains, η_{IJ} and ε_{ij}, are defined as

$$\eta_{RS} = \frac{1}{2}\left(\frac{\partial x_i}{\partial a_R} \frac{\partial x_i}{\partial a_S} - \delta_{RS} \right) \qquad \text{(Eq. 2.2)}$$

and

$$\varepsilon_{rs} = \frac{1}{2}\left(\delta_{rs} - \frac{\partial a_I}{\partial x_r} \frac{\partial a_I}{\partial x_s} \right) \qquad \text{(Eq. 2.3)}$$

respectively, where δ is the Kronecker delta (δ_{ij}=1 for i=j and δ_{ij}=0 for $i \neq j$). At infinitesimal strain these definitions are quantitatively equivalent but diverge at finite strain.

As described by Murnaghan [85] and Birch [83], the material is assumed to be hyperelastic such that the Cauchy stresses T_{ij} associated with finite elastic strains can be written in terms of the internal strain energy ϕ as

$$T_{rs} = \rho \frac{\partial \phi}{\partial \eta_{PQ}} \frac{\partial x_r}{\partial a_P} \frac{\partial x_s}{\partial a_Q} = -2\rho \frac{\partial \phi}{\partial j_{PQ}} \frac{\partial a_P}{\partial x_r} \frac{\partial a_Q}{\partial x_s} \qquad \text{(Eq. 2.4)}$$

where

$$j_{PQ} = \frac{\partial a_P}{\partial x_i}\frac{\partial a_Q}{\partial x_i} \qquad \text{(Eq. 2.5)}$$

For all strain configurations considered here, we postulate that

$$\frac{\partial a_J}{\partial x_i} = \frac{\partial a_I}{\partial x_j}\delta_{iI}\delta_{jJ} \qquad \text{(Eq. 2.6)}$$

which will be verified later. Hence, Eq. 2.5 becomes

$$j_{PQ} = \left(\delta_{pq} - 2\varepsilon_{pq}\right)\delta_{pP}\delta_{qQ} \qquad \text{(Eq. 2.7)}$$

and Eq. 2.4 reduces to

$$T_{rs} = \frac{1}{J}t_{PQ}\frac{\partial x_r}{\partial a_P}\frac{\partial x_s}{\partial a_Q} = \frac{1}{J}t_{pq}\frac{\partial a_P}{\partial x_r}\frac{\partial a_Q}{\partial x_s}\delta_{pP}\delta_{qQ} \qquad \text{(Eq. 2.8)}$$

where the terms $t_{PQ} = \rho_0(\partial\phi/\partial\eta_{PQ})$ and $t_{pq} = \rho_0(\partial\phi/\partial\varepsilon_{pq})$ are referred to as *thermodynamic tensions* [82]. It is assumed here that the stresses are entirely nondissipative, which is reasonable since elastic shock compression is typically assumed to be an isentropic, nondissipative process. Thus, the thermodynamic tension t_{PQ} is the second Piola-Kirchoff stress tensor [82]; t_{pq} is unnamed.

The stress T_{ij} is positive in tension, and we convert to a stress measure σ_{ij} that is positive in compression for comparison to shock experiments.

$$\sigma_{ij} = -T_{ij} \qquad \text{(Eq. 2.9)}$$

It is assumed that the internal energy can be expanded as a power series in strain, either as

$$\rho_0\left(\phi(S,\eta) - \phi(S,0)\right) = \frac{1}{2}C_{IJKL}\eta_{IJ}\eta_{KL} + \frac{1}{6}C_{IJKLMN}\eta_{IJ}\eta_{KL}\eta_{MN} + \frac{1}{24}C_{IJKLMNPQ}\eta_{IJ}\eta_{KL}\eta_{MN}\eta_{PQ} + \cdots \qquad \text{(Eq. 2.10.a)}$$

or

$$\rho_0\left(\phi(S,\varepsilon)-\rho_0\phi(S,0)\right)= \frac{1}{2}D_{ijkl}\varepsilon_{ij}\varepsilon_{kl}+\frac{1}{6}D_{ijklmn}\varepsilon_{ij}\varepsilon_{kl}\varepsilon_{mn}+\frac{1}{24}D_{ijklmnpq}\varepsilon_{ij}\varepsilon_{kl}\varepsilon_{mn}\varepsilon_{pq}+\cdots \quad \text{(Eq. 2.10.b)}$$

where the constants C and D are isentropic elastic constants. The first-order term is absent because the stress T_{ij} is assumed to vanish in the unstrained reference state. We also have the quantitative equivalence of the second-order constants, through $C_{IJKL}=D_{ijkl}\delta_{iI}\delta_{jJ}\delta_{kK}\delta_{lL}$, since as strain goes to zero, $\eta_{IJ}=\varepsilon_{ij}\delta_{iI}\delta_{iJ}$ and $\phi(\eta)=\phi(\varepsilon)$. Higher-order constants however, differ between these strain formalisms.

In the following discussion, both the tensors for stress (Eq. 2.8) and strain (Eqs. 2.2 and 2.3) are symmetric in line with their connection to the strain energy through Eq. 10. That is, the systems are considered at mechanical equilibrium, with $T_{ij}=T_{ji}$ implying that there is no rotation of the unit cell during volumetric and shear strain. This allows the use of Voigt notation, which takes symmetry into account by replacing indices *ij* or *IJ* as follows

$$11\rightarrow 1,\ 22\rightarrow 2,\ 33\rightarrow 3,\ (12,21)\rightarrow 6,\ (13,31)\rightarrow 5,\ (23,32)\rightarrow 4 \quad \text{(Eq. 2.11)}$$

That is, tensor subscripts written as C_{IJKL} with I,J,K,L=1,2,3 may be written instead as C_{MN} in Voigt notation with M,N=1,2,3,4,5,6. We will use Voigt notation from here on to refer to the indices of elastic constants; however, we will continue to use unabbreviated indices to refer to stresses and strains. It is important to note that the typical summation conventions of tensors do not apply in Voigt notation, and the unabbreviated indices must be used for tensor analysis involving the elastic constants.

For a simple cubic system, such as diamond, there are 3 independent second-order elastic constants, which, as mentioned earlier, are equivalent for the Eulerian and Lagrangian cases, as in

$$
\begin{aligned}
C_{11} &= C_{22} = C_{33} = D_{11} = D_{22} = D_{33} \\
C_{12} &= C_{13} = C_{23} = D_{12} = D_{13} = D_{23} \\
C_{44} &= C_{55} = C_{66} = D_{44} = D_{55} = D_{66}
\end{aligned}
\qquad \text{(Eq. 2.12)}
$$

There are 6 independent third-order constants [82], written here for the Lagrangian case

$$
\begin{aligned}
&C_{111} = C_{222} = C_{333} \\
&C_{144} = C_{255} = C_{366} \\
&C_{112} = C_{223} = C_{133} = C_{113} = C_{122} = C_{233} \\
&C_{166} = C_{155} = C_{266} = C_{244} = C_{355} = C_{344} \\
&C_{123} \\
&C_{456}
\end{aligned}
\qquad \text{(Eq. 2.13)}
$$

The Eulerian case is identical with the C's replaced with D's; however, as mentioned earlier the third-order constants are not equivalent between the two formulations. All other constants not listed above vanish for cubic symmetry. For crystals of lower symmetry there are a larger number of independent elastic constants. For example simple trigonal crystals, such as quartz and sapphire, have 6 second-order constants and 14 third-order constants [89-92]. Depending on the symmetry of the strain configuration, however, a smaller number of elastic constants may appear in the internal energy expansion Eq. 2.10.

Writing out the terms in Eq. 2.10.a to third-order in Lagrangian strain for a cubic crystal, we have

$$\begin{aligned}\rho_0\phi(S,\eta)-\rho_0\phi(S,0) &= \tfrac{1}{2}C_{11}\left[\eta_{11}^2+\eta_{22}^2+\eta_{33}^2\right]+C_{12}\left[\eta_{11}\eta_{22}+\eta_{22}\eta_{33}+\eta_{11}\eta_{33}\right]\\ &+C_{44}\left[\eta_{12}^2+\eta_{21}^2+\eta_{13}^2+\eta_{31}^2+\eta_{23}^2+\eta_{32}^2\right]+\tfrac{1}{6}C_{111}\left[\eta_{11}^3+\eta_{22}^3+\eta_{33}^3\right]\\ &+\tfrac{1}{2}C_{112}\left[\eta_{11}^2(\eta_{22}+\eta_{33})+\eta_{22}^2(\eta_{11}+\eta_{33})+\eta_{33}^2(\eta_{11}+\eta_{22})\right]\\ &+C_{123}\left[\eta_{11}\eta_{22}\eta_{33}\right]+C_{456}\left[(\eta_{12}+\eta_{21})(\eta_{13}+\eta_{31})(\eta_{23}+\eta_{32})\right]\\ &+C_{144}\left[\eta_{11}(\eta_{23}^2+\eta_{32}^2)+\eta_{22}(\eta_{13}^2+\eta_{31}^2)+\eta_{33}(\eta_{12}^2+\eta_{21}^2)\right]\\ &+C_{166}\left[(\eta_{12}^2+\eta_{21}^2)(\eta_{11}+\eta_{22})+(\eta_{13}^2+\eta_{31}^2)(\eta_{11}+\eta_{33})+(\eta_{23}^2+\eta_{32}^2)(\eta_{22}+\eta_{33})\right]\end{aligned} \quad \text{(Eq. 2.14)}$$

where the constants C_{MN} and C_{MNO} are the second- and third-order elastic constants in Voigt subscript notation, and strain terms are denoted with standard indices for the purposes of differentiation with respect to strain in determining t_{PQ} and t_{pq}. It should be noted that the expansion in Eq. 2.14 differs from that found in an early work by Birch [83] on the subject of finite strain, due to his use of antiquated definitions of the third-order elastic constants [82, 87].

The second- and third-order elastic constants are often known from infinitesimal-compression (e.g., wave-velocity) experiments on materials at ambient conditions and relatively low stresses using ultrasonic, Brillouin scattering, and Raman scattering techniques. In general, these studies report third-order Lagrangian elastic constants, that is C_{MNO}. Third-order Eulerian elastic constants, D_{mno}, while not typically reported, can be related to the third-order Lagrangian constants for the crystal systems and strain configurations relevant to this study. Birch [83] suggested an approach to accomplish this, in which the exact relationship between the Lagrangian and Eulerian constants could be obtained by equating the internal energy expansions of Eqs. 2.10.a and 2.10.b and comparing terms of identical order in strain. Using this method, we have obtained

complete relationships between the third-order Lagrangian and Eulerian elastic constants for a cubic crystal (for details, see Appendix B)

$$\begin{aligned} D_{111} &= 12C_{11} + C_{111} \\ D_{112} &= 4C_{12} + C_{112} \\ D_{123} &= C_{123} \\ D_{166} &= C_{11} + C_{12} + 4C_{44} + C_{166} \\ D_{144} &= 2C_{12} + C_{144} \\ D_{456} &= 3C_{44} + C_{456} \end{aligned} \qquad \text{(Eq. 2.15)}$$

For compression in certain high-symmetry directions of non-cubic crystals, such as *a*- and *c*-axis of trigonal crystals, we also have the relevant Eulerian elastic constants

$$D_{mmm} = 12C_{MM} + C_{MMM} \qquad \text{(Eq. 2.16)}$$

where *m*,*M* are Voigt pairs of tensor indices, with $m=M=1$ for the *a*-axis direction of a trigonal crystal and $m=M=3$ for the *c*-axis direction.

Fourth-order elastic constants have been determined through shock-wave experiments [41, 46, 57], hydrostatic compression experiments [65], and first-principles calculations [70, 81], as well as other techniques [57]. Fourth-order elastic effects, however, are frequently not significant when describing moderate hydrostatic compressions of materials [86, 93], and it remains to be seen whether they are necessary for small uniaxial compressions.

Differences between Lagrangian and Eulerian treatments of finite strain:

Given an internal energy defined as an infinite power series in strain (Eq. 2.10) the treatments of finite strain through the Lagrangian and Eulerian approaches would be theoretically equivalent. These treatments become inequivalent in practice when the internal energy is truncated at a certain order of strain. Under hydrostatic stress, the

Eulerian treatment – in the form of the Birch-Murnaghan equation – emerges as the more powerful because of it's empirical consistency with independent measurements of elastic moduli and static compression data when expanded to only third- or fourth-order in strain [65, 86, 93]. Lagrangian descriptions to equivalent orders of strain are found to be empirically inconsistent with the measurements. While this inconsistency can be resolved by expanding the internal energy to higher orders in the case of Lagrangian strain [65], the relative simplicity of the Eulerian description has led to it being the preferred method for describing and interpreting finite-strain data under hydrostatic conditions. Other successful equations of state, such as the Vinet model, closely match the Eulerian finite-strain model [86]. The underlying physical explanation for the differences between Lagrangian and Eulerian strain formulations has been discussed elsewhere [85, 86].

For strongly anisotropic stress and strain conditions, the relative value of these finite strain approaches is not clear. For a system under uniaxial strain – which is, in ideal circumstances, the condition of strain and stress applied by elastic shock waves – the discrepancies between the Lagrangian and Eulerian approaches have only been occasionally discussed [70], and in most analyses of shock data the Lagrangian approach has been used without consideration of alternative strain formulations [41, 44, 46, 57, 81, 82]. There could be several reasons for this. Firstly, it may be tacitly assumed that the elastic uniaxial strains possible in materials are so small – on the order of several % in volume – that the Lagrangian and Eulerian treatments are essentially identical. Secondly, it has been suggested that the Eulerian formalism is valid only in certain special cases, such as that of an isotropic medium under hydrostatic stress, where the Eulerian strain

definition satisfies the condition of frame-indifference [94-98]. A rank two tensor quantity G, such as material strain (Eqs. 2.2 and 2.3), is considered to be frame-indifferent if it transforms according to

$$G^* = Q \cdot G \cdot Q^T \qquad \text{(Eq. 2.17)}$$

where Q is any arbitrary orthogonal transformation tensor with a transpose Q^T [98]. Since the Eulerian strain tensor Eq. 2.3 does not, in general, satisfy this requirement [94-98], and since to these author's knowledge only the special case of hydrostatic stress has been shown to lead to a frame-indifferent Eulerian strain, it would seem possible that Eulerian strain is does not satisfy frame-indifference under anisotropic strain conditions.

However, it is found that neither of the above concerns are legitimate; the differences between the Lagrangian and Eulerian finite-strain formalisms are considerable even at strains of a few percent, and the Eulerian strain tensor is found to conform to frame-indifference under uniaxial strain as well as under isotropic strain, as will be discussed.

Given that third-order Eulerian elasticity is usually sufficient to describe hydrostatic compression to strains of many tens of percent, it might be surprising to find that fourth-order (or higher) elasticity is necessary for uniaxial strain to only a few percent. Previous shock-wave and first-principles studies [41, 46, 57, 70, 81] have generally concluded that indeed, higher-order elasticity, represented by a fourth-order elastic constant, is necessary to fit the uniaxial stress-strain response – however, most of these studies only evaluated the fourth-order constants in terms of Lagrangian strain. It stands to reason, in analogy with the findings under isotropic strain conditions, that an Eulerian approach to uniaxial strain may provide a simpler description of the uniaxial

stress-strain response – perhaps limited to only third-order in strain. However, as will be demonstrated here, the need for higher-order elasticity in uniaxial strain is robust, regardless of the strain formulation used.

Finite uniaxial strain:

In diamond, a cubic crystal, the only crystallographic directions allowed by symmetry to propagate pure-longitudinal infinitesimal strain modes are <100>, <110> and <111> [42]. In trigonal crystals, such as quartz and sapphire, symmetry dictates that pure infinitesimal strain modes can only exist in the *a*- and *c*-axis directions [46, 57]. It was found in incremental finite strain models that these directions, corresponding to axes of rotational symmetry in the crystal, are also able to sustain purely longitudinal shock waves for an ideal elastic material [43].

In pure longitudinal mode directions, infinitesimal strain is represented by sound wave propagation, and finite strain associated with elastic shock wave compression. As progressively weaker shock waves are considered, the sound-wave velocities serve as an important reference point at zero strain. Such sound waves are related to the second-order elastic constants of a material [42]. For the <100> direction in cubic crystals, and *a*- and *c*-axis compression of trigonal crystals, the longitudinal sound velocity V_l is

$$V_l = \sqrt{\frac{C_{MM}}{\rho_0}} \qquad \text{(Eq. 2.18.a)}$$

where M is a Voigt index and ρ_0 is the ambient density. The index M=1 for a cubic crystal strained in the <100> orientation and for a trigonal crystal strained along the *a*-axis, while M=3 for a trigonal crystal strained along the *c*-axis.

For <110> strain in a cubic system, the longitudinal sound velocity is

$$V_l = \sqrt{\frac{C_{11} + C_{12} + 2C_{44}}{2\rho}} \qquad \text{(Eq. 2.18.b)}$$

while for <111> strain we have

$$V_l = \sqrt{\frac{C_{11} + 2C_{12} + 4C_{44}}{3\rho}} \qquad \text{(Eq. 2.18.c)}$$

For elastic shock waves, with shock speed D and particle speed u, we expect that $D(u=0) = V_l$.

As the sound velocity in the <100> direction of a cubic crystal is similar in form to the sound velocity along the high symmetry axes of trigonal crystals, we will also find that the constitutive relations developed for finite uniaxial strain in the cubic <100> direction and along the high-symmetry axes of trigonal crystals are identical in form. Therefore, by developing constitutive relations for the <100>, <110> and <111> cubic orientations, we will have a suite of formulations that will apply to many of the solids studied to date. Development of these uniaxial strain constitutive relations has been partially completed in previous studies using Lagrangian [44, 46, 70] and Eulerian [70] formulations.

The finite strains associated with uniaxial strain in cubic directions <100>, <110>, and <111> can be written as

$$\eta_{IJ}^{<100>} = \begin{bmatrix} \eta & 0 & 0 \\ 0 & 0 & 0 \\ 0 & 0 & 0 \end{bmatrix}, \quad \eta_{IJ}^{<110>} = \begin{bmatrix} \eta & \eta & 0 \\ \eta & \eta & 0 \\ 0 & 0 & 0 \end{bmatrix}, \quad \eta_{IJ}^{<111>} = \begin{bmatrix} \eta & \eta & \eta \\ \eta & \eta & \eta \\ \eta & \eta & \eta \end{bmatrix} \qquad \text{(Eq. 2.19.a)}$$

for Lagrangian strain and

$$\varepsilon_{ij}^{<100>} = \begin{bmatrix} \varepsilon & 0 & 0 \\ 0 & 0 & 0 \\ 0 & 0 & 0 \end{bmatrix}, \quad \varepsilon_{ij}^{<110>} = \begin{bmatrix} \varepsilon & \varepsilon & 0 \\ \varepsilon & \varepsilon & 0 \\ 0 & 0 & 0 \end{bmatrix}, \quad \varepsilon_{ij}^{<111>} = \begin{bmatrix} \varepsilon & \varepsilon & \varepsilon \\ \varepsilon & \varepsilon & \varepsilon \\ \varepsilon & \varepsilon & \varepsilon \end{bmatrix} \qquad \text{(Eq. 2.19.b)}$$

for Eulerian strain. The validity of these definitions will be addressed later.

Defining a primed coordinate system aligned with the axis of uniaxial compression, we have

$$\eta_{IJ}^{/} = \begin{bmatrix} \eta^{/} & 0 & 0 \\ 0 & 0 & 0 \\ 0 & 0 & 0 \end{bmatrix} \qquad \text{(Eq. 2.20.a)}$$

and

$$\varepsilon_{ij}^{/} = \begin{bmatrix} \varepsilon^{/} & 0 & 0 \\ 0 & 0 & 0 \\ 0 & 0 & 0 \end{bmatrix} \qquad \text{(Eq. 2.20.b)}$$

for the Lagrangian and Eulerian strain. Quantities in the primed and unprimed coordinates are related by a coordinate transformation of the form

$$K_{ij} = R_{ki} R_{lj} K_{kl}^{/} \qquad \text{(Eq. 2.21)}$$

with the inverse transformation

$$K_{ij}^{/} = R_{ik} R_{jl} K_{kl} \qquad \text{(Eq. 2.22)}$$

where K_{ij} is a second-rank tensor, such as the strain η_{IJ} and ε_{ij}, the Cauchy stress T_{ij}, or the thermodynamic stresses t_{IJ} and t_{ij}, and where R_{ij} is a rotation matrix.

For <100> uniaxial strain, the crystallographically-based coordinate system is already aligned with the compression axis, and the transformation matrix to the primed system is $R_{ij}=\delta_{ij}$, that is

$$R_{ij}^{<100>} = \begin{bmatrix} 1 & 0 & 0 \\ 0 & 1 & 0 \\ 0 & 0 & 1 \end{bmatrix} \qquad \text{(Eq. 2.23.a)}$$

For <110> and <111> strains, the transformation matrices are

$$R_{ij}^{<110>} = \begin{bmatrix} \frac{1}{\sqrt{2}} & \frac{1}{\sqrt{2}} & 0 \\ -\frac{1}{\sqrt{2}} & \frac{1}{\sqrt{2}} & 0 \\ 0 & 0 & 1 \end{bmatrix} \qquad \text{(Eq. 2.23.b)}$$

and

$$R_{ij}^{<111>} = \begin{bmatrix} \frac{1}{\sqrt{3}} & \frac{1}{\sqrt{3}} & \frac{1}{\sqrt{3}} \\ -\frac{1}{\sqrt{6}} & -\frac{1}{\sqrt{6}} & \frac{2}{\sqrt{6}} \\ \frac{1}{\sqrt{2}} & -\frac{1}{\sqrt{2}} & 0 \end{bmatrix} \qquad \text{(Eq. 2.23.c)}$$

The reason for using the primed coordinate system is that with respect to this system the stress variables are directly related to the longitudinal shock stress, and the definition of strain is particularly straightforward. The relationship between the initial $a_I^{/}$ and final $x_i^{/}$ coordinates can be written simply as

$$\begin{aligned} x_1^{/} &= \gamma a_1^{/} \\ x_2^{/} &= a_2^{/} \\ x_3^{/} &= a_3^{/} \end{aligned} \qquad \text{(Eq. 2.24)}$$

where $\gamma=\rho_0/\rho=J$ by Eq. 2.1. With this relation, we can write the strains in Eq. 2.20 as

$$\eta_{11}^{/} = \eta^{/} = \frac{1}{2}\left[\left(\frac{\rho_0}{\rho}\right)^2 - 1\right] \qquad \text{(Eq. 2.25)}$$

and

$$\varepsilon_{11}^{/} = \varepsilon^{/} = \frac{1}{2}\left[1 - \left(\frac{\rho}{\rho_0}\right)^2\right] \qquad \text{(Eq. 2.26)}$$

with all other $\eta_{IJ}^{/}$ and $\varepsilon_{ij}^{/}$ equal to zero.

By applying the rotations in Eq. 2.21 and 2.23, we obtain the strain parameters referenced to the real (crystallographic) coordinate system. For <100> strain, the primed and unprimed terms are identical, that is

$$\eta_{IJ}^{<100>} = \eta' \begin{bmatrix} 1 & 0 & 0 \\ 0 & 0 & 0 \\ 0 & 0 & 0 \end{bmatrix} \text{ and } \varepsilon_{ij}^{<100>} = \varepsilon' \begin{bmatrix} 1 & 0 & 0 \\ 0 & 0 & 0 \\ 0 & 0 & 0 \end{bmatrix} \quad \text{(Eq. 2.27)}$$

For <110> strain, coordinate rotation gives

$$\eta_{IJ}^{<110>} = \frac{1}{2}\eta' \begin{bmatrix} 1 & 1 & 0 \\ 1 & 1 & 0 \\ 0 & 0 & 0 \end{bmatrix} \text{ and } \varepsilon_{ij}^{<110>} = \frac{1}{2}\varepsilon' \begin{bmatrix} 1 & 1 & 0 \\ 1 & 1 & 0 \\ 0 & 0 & 0 \end{bmatrix} \quad \text{(Eq. 2.28)}$$

and for <111> strain, coordinate rotation gives

$$\eta_{IJ}^{<111>} = \frac{1}{3}\eta' \begin{bmatrix} 1 & 1 & 1 \\ 1 & 1 & 1 \\ 1 & 1 & 1 \end{bmatrix} \text{ and } \varepsilon_{ij}^{<111>} = \frac{1}{3}\varepsilon' \begin{bmatrix} 1 & 1 & 1 \\ 1 & 1 & 1 \\ 1 & 1 & 1 \end{bmatrix} \quad \text{(Eq. 2.29)}$$

These are consistent with the initial definition of strain in Eq. 2.19.

However, in light of the earlier caveat that in general, Eulerian strain formalisms are not frame-independent, it stands to reason that the coordinate transformation used above, Eq. 2.21 – which is equivalent to the condition for frame indifference Eq. 2.17 – might not actually be valid in the case of Eulerian strain. Thus, we seek to verify the Eulerian parts of Eqs. 2.28 and 2.29 by a different approach. We first assume that the rotation Eq. 2.21 is valid for Lagrangian strain, as is expected due to general frame-indifference of the Lagrangian strain tensor. We then obtain a set of relationships between the coordinates x_i and a_I in the crystallographic reference frame, similar to Eq. 2.24, by taking the Lagrangian components of Eqs. 2.28 and 2.29, the strain definitions

Eqs. 2.2 and 2.25, and algebraically solving for the relationship between x_i and a_I that yields a state of uniaxial strain.

This relationship, for <100> strain, is simply Eq. 2.24 with the primes removed. The results for <110> and <111> uniaxial compression are

$$\begin{aligned} x_1 &= \tfrac{1}{2}[a_1 - a_2 + \gamma(a_1 + a_2)] & a_1 &= \tfrac{1}{2\gamma}[x_1 + x_2 + \gamma(x_1 - x_2)] \\ x_2 &= \tfrac{1}{2}[a_2 - a_1 + \gamma(a_1 + a_2)] & a_2 &= \tfrac{1}{2\gamma}[x_1 + x_2 + \gamma(x_2 - x_1)] \\ x_3 &= a_3 & a_3 &= x_3 \end{aligned} \qquad \text{(Eq. 2.30)}$$

and

$$\begin{aligned} x_1 &= \tfrac{1}{3}[2a_1 - a_2 - a_3 + \gamma(a_1 + a_2 + a_3)] & a_1 &= \tfrac{1}{3\gamma}[x_1(1 + 2\gamma) + (x_2 + x_3)(1 - \gamma)] \\ x_2 &= \tfrac{1}{3}[2a_2 - a_1 - a_3 + \gamma(a_1 + a_2 + a_3)] & a_2 &= \tfrac{1}{3\gamma}[x_2(1 + 2\gamma) + (x_1 + x_3)(1 - \gamma)] \\ x_3 &= \tfrac{1}{3}[2a_3 - a_1 - a_2 + \gamma(a_1 + a_2 + a_3)] & a_3 &= \tfrac{1}{3\gamma}[x_3(1 + 2\gamma) + (x_1 + x_2)(1 - \gamma)] \end{aligned} \qquad \text{(Eq. 2.31)}$$

respectively. As before, $\gamma=\rho_0/\rho=J$. Now, from the $x_i(a_I)$ in Eqs. 2.30 and 2.31, the ε_{ij} (Eq. 2.3) can be determined in the crystallographic coordinates directly, leading to the Eulerian parts of Eqs. 2.28 and 2.29 that were originally obtained by coordinate transformation of the Eulerian strain. Thus, under uniaxial strain, the Eulerian strain tensor is legitimately transformed (in this case rotated) by Eq. 2.21, and thus appears to satisfy the condition of material frame indifference given by Eq. 2.17. Additional transformations using Eq. 2.17, such as rotation and translation, will also be valid due to homogeneity of strain.

The $x_i(a_I)$ relations in Eqs. 2.24, 2.30 and 2.31 also satisfy Eq. 2.6, which was originally presented without proof.

Using the definitions of internal energy given in Eq. 2.10, the stresses $\sigma_{ij}^{/}$ for the <100> orientation, where the primed and crystallographic coordinate systems are identical, are obtained by considering Eqs. 2.8, 2.9, 2.10, 2.24, and 2.27:

$$\begin{aligned}
\sigma'_{11} &= -\tfrac{\rho_0}{\rho}\eta'[C_{11} + \tfrac{1}{2}\eta' C_{111} + \cdots] \\
\sigma'_{22} &= \sigma'_{33} = -\tfrac{\rho}{\rho_0}\eta'[C_{12} + \tfrac{1}{2}\eta' C_{112} + \cdots] \\
\sigma'_{12} &= \sigma'_{13} = \sigma'_{23} = 0
\end{aligned} \qquad \text{(Eq. 2.32.a)}$$

for the Lagrangian approach and

$$\begin{aligned}
\sigma'_{11} &= -\left(\tfrac{\rho}{\rho_0}\right)^3 \varepsilon'[C_{11} + \tfrac{1}{2}\varepsilon' D_{111} + \cdots] \\
\sigma'_{22} &= \sigma'_{33} = -\tfrac{\rho}{\rho_0}\varepsilon'[C_{12} + \tfrac{1}{2}\varepsilon' D_{112} + \cdots] \\
\sigma'_{12} &= \sigma'_{13} = \sigma'_{23} = 0
\end{aligned} \qquad \text{(Eq. 2.32.b)}$$

for the Eulerian. All shear stresses vanish and the lateral stresses are equal due to the assumed alignment of the uniaxial compression with the primed (shock) coordinate frame. There are two ways to derive the stresses σ'_{ij} for the <110> and <111> uniaxial strain orientations. One is to determine the Cauchy stress tensor T_{ij} in the crystallographic reference frame using Eqs. 2.8 and 2.10, and the $x_i(a_I)$ in Eqs. 2.30 and 2.31, after which T_{ij} can be rotated to the primed frame with Eq. 2.22. The other is to determine the thermodynamic stress tensors t_{IJ} and t_{ij} in the crystallographic reference frame from Eq. 2.10, rotate the thermodynamic stress into the primed frame with Eq. 2.22, and then using the $x_i(a_I)$ of Eq. 2.24, calculate T'_{ij} from the t'_{IJ} and t'_{ij} with Eq. 2.8. Both methods give identical results; the second approach is outlined by Boteler [44].

That is, for <110>

$$\begin{aligned}
\sigma'_{11} &= -\tfrac{1}{2}\tfrac{\rho_0}{\rho}\eta'[C_{11} + C_{12} + 2C_{44} + \tfrac{1}{4}\eta'(C_{111} + 3C_{112} + 12C_{166}) + \cdots] \\
\sigma'_{22} &= -\tfrac{1}{2}\tfrac{\rho}{\rho_0}\eta'[C_{11} + C_{12} - 2C_{44} + \tfrac{1}{4}\eta'(C_{111} + 3C_{112} - 4C_{166}) + \cdots] \\
\sigma'_{33} &= -\tfrac{1}{2}\tfrac{\rho}{\rho_0}\eta'[2C_{12} + \tfrac{1}{2}\eta'(C_{112} + C_{123} + 2C_{144}) + \cdots] \\
\sigma'_{12} &= \sigma'_{13} = \sigma'_{23} = 0
\end{aligned} \qquad \text{(Eq. 2.33.a)}$$

and

$$\begin{aligned}
\sigma_{11}^{/} &= -\tfrac{1}{2}\left(\tfrac{\rho}{\rho_0}\right)^3 \varepsilon^{/}[C_{11}+C_{12}+2C_{44}+\tfrac{1}{4}\varepsilon^{/}(D_{111}+3D_{112}+12D_{166})+\cdots] \\
\sigma_{22}^{/} &= -\tfrac{1}{2}\tfrac{\rho}{\rho_0}\varepsilon^{/}[C_{11}+C_{12}-2C_{44}+\tfrac{1}{4}\varepsilon^{/}(D_{111}+3D_{112}-4D_{166})+\cdots] \\
\sigma_{33}^{/} &= -\tfrac{1}{2}\tfrac{\rho}{\rho_0}\varepsilon^{/}[2C_{12}+\tfrac{1}{2}\varepsilon^{/}(D_{112}+D_{123}+2D_{144})+\cdots] \\
\sigma_{12}^{/} &= \sigma_{13}^{/} = \sigma_{23}^{/} = 0
\end{aligned} \qquad \text{(Eq. 2.33.b)}$$

The lateral stresses are not equal for <110> strain, and the rotation matrix chosen for this orientation (2.23.b) has aligned the primed axes with the directions of principal stress – that is, all lateral shear stresses vanish.

Correspondingly, for <111> we have

$$\begin{aligned}
\sigma_{11}^{/} &= -\tfrac{1}{3}\tfrac{\rho_0}{\rho}\eta^{/}[C_{11}+2C_{12}+4C_{44} \\
&\qquad +\tfrac{1}{6}\eta^{/}(C_{111}+6C_{112}+24C_{166}+2C_{123}+12C_{144}+16C_{456})+\cdots] \\
\sigma_{22}^{/} &= \sigma_{33}^{/} = -\tfrac{1}{3}\tfrac{\rho}{\rho_0}\eta^{/}[C_{11}+2C_{12}-2C_{44}+\tfrac{1}{6}\eta^{/}(C_{111}+6C_{112}+2C_{123}-8C_{456})+\cdots] \\
\sigma_{12}^{/} &= \sigma_{13}^{/} = \sigma_{23}^{/} = 0
\end{aligned} \qquad \text{(Eq. 2.34.a)}$$

and

$$\begin{aligned}
\sigma_{11}^{/} &= -\tfrac{1}{3}\left(\tfrac{\rho}{\rho_0}\right)^3\varepsilon^{/}[C_{11}+2C_{12}+4C_{44} \\
&\qquad +\tfrac{1}{6}\varepsilon^{/}(D_{111}+6D_{112}+24D_{166}+2D_{123}+12D_{144}+16D_{456})+\cdots] \\
\sigma_{22}^{/} &= \sigma_{33}^{/} = -\tfrac{1}{3}\tfrac{\rho}{\rho_0}\varepsilon^{/}[C_{11}+2C_{12}-2C_{44}+\tfrac{1}{6}\varepsilon^{/}(D_{111}+6D_{112}+2D_{123}-8D_{456})+\cdots] \\
\sigma_{12}^{/} &= \sigma_{13}^{/} = \sigma_{23}^{/} = 0
\end{aligned} \qquad \text{(Eq. 2.34.b)}$$

and lateral stresses are isotropic as in the <100> case.

For high-symmetry uniaxial strain in the <100> direction of a cubic crystal (e.g. Eq. 2.32) and, for example, in the *a*- and *c*-axis directions of trigonal crystals, the fourth-order term of the longitudinal stress σ_{L} ($\sigma_{11}^{/}$ in the case of <100> cubic strain) contains a single elastic constant, C_{MMMM} or D_{mmmm}, as in

$$\sigma_{\mathrm{L}} = -\tfrac{\rho_0}{\rho}\eta^{/}[C_{MM}+\tfrac{1}{2}\eta^{/}C_{MMM}+\tfrac{1}{6}\left(\eta^{/}\right)^2 C_{MMMM}+\cdots] \qquad \text{(Eq. 2.35.a)}$$

and

$$\sigma_{\mathrm{L}} = -\left(\frac{\rho}{\rho_0}\right)^3 \varepsilon^{/}\left[D_{mm} + \tfrac{1}{2}\varepsilon^{/} D_{mmm} + \tfrac{1}{6}\left(\varepsilon^{/}\right)^2 D_{mmmm} + \cdots\right] \qquad \text{(Eq. 2.35.b)}$$

where M and m are Voigt pairs of indices denoting a high-symmetry direction, such as M,m=1 for the trigonal a-axis and cubic <100> direction, and M,m=3 for the trigonal c-axis direction. Some effort has gone into measurement of C_{MMMM} from shock data for certain high symmetry directions in crystals [41, 46, 57].

Eqs. 2.33 and 2.34 for <110> and <111> uniaxial strain, however, become complicated when extended to fourth-order, and shock experiments in these orientations (which usually measure only $\sigma_{11}^{/}$) can only constrain sums of fourth-order constants. Consequently we cannot expect to resolve most of the individual fourth-order elastic constants from shock data, and since independent measurements of fourth-order elastic constants are generally not available, we will not concern ourselves with the combination of constants appearing in the fourth-order terms of Eqs. 2.33 and 2.34, and consider only a single fourth-order constant to represent that combination in our analysis of <110> and <111> cubic shock data.

Comparison to elastic shock wave data:

To relate the uniaxial strain constitutive relations to shock wave systems, we consider the Hugoniot equations (Chapter 1) and rewrite them as

$$\begin{aligned} P &= \sigma_{11}^{/} = \sigma_{\mathrm{L}} \\ D &= \sqrt{\frac{P}{\rho_0\left(1-\frac{\rho_0}{\rho}\right)}} \\ u &= \frac{P}{\rho_0 D} = \sqrt{\frac{P}{\rho_0}\left(1-\frac{\rho_0}{\rho}\right)} \end{aligned} \qquad \text{(Eq. 2.36)}$$

Thus, for a given change in density ρ/ρ_0 in uniaxial strain, the shock stress P, shock speed D, and particle speed u are defined.

It is expected that as the infinitesimal strain limit (u=0, ρ/ρ_0=1) is approached, D will converge with the ambient longitudinal sound speeds, given by Eqs. 2.18.

The elastic Hugoniot can be determined by data from elastic shock waves with stresses below the Hugoniot elastic limit (HEL), and by elastic precursor shocks forming at or near the HEL and ahead of a plastic deformation wave [41]. In this manner, the entire elastic compression range possible for a material can be explored experimentally, inasmuch as the HEL represents a fundamental limit on purely elastic response. Several elastic Hugoniot models will be considered:

1) Third-order finite uniaxial strain models with the second- and third-order elastic constants taken from the literature, using Lagrangian ("L3 lit"), and Eulerian ("E3 lit") formulations.
2) Third-order models with second-order constants from the literature, and third-order terms fit to the data. Often in fitting third-order terms, only a sum of elastic constants is fit; individual constants may be undetermined. These models are labeled as "L3 fit" and "E3 fit" for Lagrangian and Eulerian formulations, respectively.
3) Fourth-order models with second- and third-order constants taken from the literature, and the fourth-order term fit to the data, are labeled "L4" and "E4" for Lagrangian and Eulerian formulations, respectively.
4) Linear D-u fits to the elastic shock data, centered on the longitudinal sound speeds.

Given the typical precision of the shock measurements, it is usually not realistic to fit for more than one finite-strain term, third- or fourth-order, at a time; we do not examine this possibility here. Second-order finite-strain and linear-elastic models are not useful for comparison to the measurements for reasons that will be discussed.

Materials:

Sapphire

The finite strain response of single-crystal sapphire has been considered previously in [18, 57], and elastic shock data are available from [18, 33, 99, 100]. Both *a*- and *c*-crystallographic axes display nearly identical elastic responses [57] (these directions are also referred to as the *x*-axis or 90° orientation and the *z*-axis or the 0° orientation, respectively). For the current analysis of sapphire, we take the second-order elastic constants from [90] and the third-order constants from [89] (Lagrangian) and Eq. 2.16 (Eulerian). All are based on ultrasonic measurements under pressure (some of the published values have changed due to adopting current crystallographic conventions [101], but this does not affect C_{11}, C_{111}, D_{111}, C_{33}, C_{333}, and D_{333}, relevant to the present study).

The data and finite strain theories are shown in Fig. 2.1. For this material only third-order finite strain predictions, based on the literature elastic constants, are needed, as these agree satisfactorily with the data for both the Lagrangian and Eulerian approaches. Linear *D*-*u* fits also represent the data well. There is no convincing reason to examine the possibility of a fourth-order elastic contribution, given the scatter in the

measurements; this contrasts with previous reports of fourth-order elastic effects in sapphire by Graham [57].

Quartz

The finite strain response of quartz has been considered previously in [41, 46, 81], with elastic shock data available from [41, 45, 46]; as a trigonal crystal, the orientations of quartz can be specified as described for sapphire, though recognizing that quartz is enantiomorphic. The second-order elastic constants are from [92] and the third-order constants are taken from [91] (Lagrangian) and Eq. 2.16 (Eulerian); they are based on ultrasonic measurements.

For quartz, it appears that fourth-order elasticity is needed to fit the data using both Eulerian and Lagrangian formalisms (Fig. 2.2). The most useful orientation here is the *c*-axis orientation, for which high precision measurements of the low-stress elastic Hugoniot exist [41]. In this orientation, third-order elasticity, whether using the ultrasonically-determined or fitted C_{333} and D_{333} fail to describe the elastic shock data. Similarly, a linear fit fails to represent the data. Thus, only fourth-order elasticity can reasonably match the measurements in this orientation. Both Lagrangian and Eulerian fourth-order fits match the nonlinearity of the low-stress, high-precision data [41], and while the high-stress extrapolation of these theories differ, the data are not precise enough to favor one over the other.

Similarly, for the *a*-axis orientation, third-order fits using the known constants C_{111} and D_{111} fail to reproduce the data, and fourth-order elasticity must be invoked. High-precision experiments on the *a*-axis elastic Hugoniot, particularly at low stresses

where the deviations between different models are substantial, could help discriminate between Eulerian and Lagrangian analyses.

Diamond

For diamond, the finite strain response under uniaxial compression was considered previously [44] to predict the elastic Hugoniots of diamond [44, 102, 103]. However, no elastic Hugoniot measurements existed at that time to confirm these predictions. New elastic Hugoniot data in the form of elastic precursor measurements have been presented in Chapter 1 for the pure-longitudinal mode directions of diamond, <100>, <110> and <111>. With this data, we may reconsider how finite strain theory may be used to describe these elastic Hugoniots.

For diamond, the second-order elastic constants were determined most accurately by Brillouin scattering in [49]. Third-order Lagrangian elastic constants were determined by analysis of Raman data in [58, 104] and we use the presumably more accurate values of [58] as recommended by Boteler [44, 103]. Third-order Eulerian constants are determined through Eq. 2.15.

As third-order constants were determined by a relatively nonstandard technique for diamond, we consider their consistency with other datasets, specifically, measurements of the isothermal hydrostatic response of diamond measured with static compression [59, 60]. This analysis can be found in Chapter 1. It was concluded that the third-order isentropic elastic constants of [58], yielding a bulk modulus pressure derivative of $\partial K_{0S} / \partial P$ =4.52, are inconsistent with $\partial K_{0S} / \partial P$ suggested by static compression measurements of 3.93±.27. Thus, it is expected that there will be some improvement on the individual third-order isentropic elastic constants in the future.

Nonetheless, the relatively close agreement of these determinations suggests that use of the existing constants will be sufficient for the present study.

In the case of shock compression in the <100> and <111> directions of diamond, it appears that as for quartz, fourth-order elasticity is needed to represent the data when third-order constants are presumed known (Fig. 2.3). The same is true for the <110> data in the Eulerian formalism, but for the Lagrangian the third-order description is sufficient. Only in the case of <100> compression does the fourth-order finite-strain theory constrain directly a fourth-order elastic constant, yielding $C_{1111}\approx$380 TPa and $D_{1111}\approx$170 TPa for diamond (Fig. 2.3.a).

In addition to the models based on literature constants, it is also seen that linear *D-u* fits and third-order finite strain models with fitted third-order parameters represent the shock data reasonably well. Models diverge significantly at low stress, and thus accurate shock data from this regime could further discriminate between the them.

A number of first-principles and molecular dynamics computations have been conducted that describe diamond under uniaxial strain conditions [70, 74, 75, 81, 105, 106]. The results of some of these simulations are plotted in Fig. 2.3. The early first principles calculations of Nielson [70] for uniaxial strain in the <100> and <110> directions were obtained directly from the author [107] for maximal precision, which is needed to accurately convert the data into *D-u* space; Nielson's data for <110> was transformed into shock coordinates with Eq. 2.22. The u=0 velocity limits were obtained from Nielson's computed second-order elastic constants. It is interesting to note that modern calculations of uniaxial strain in the <100> direction [81] are largely similar to

those of Nielson, and that neither appear to accurately represent the data. Nielson's results for strain in <110>, however do appear to agree with measurements.

Also shown are recent results from McLaughlin et. al. [74] which simulate through molecular dynamics the conditions of elastic shock waves propagating in the <110> direction. Interestingly, those results predict elastic shock waves that exhibit constant wave velocity with increasing stress and particle velocity. This is consistent with our measurements for the <110> orientation and the predictions of finite strain models, which show a weak or even negative scaling of shock speed with particle speed.

Linear elasticity:

For very small strain, it might be expected that the constitutive relations obtained here will converge with the infinitesimal or linear theory of elasticity, as represented by Hooke's Law [98]

$$\sigma_{ij} = C_{ijkl}\theta_{kl} \qquad \text{(Eq. 2.37)}$$

where θ_{kl} is the classical infinitesimal strain tensor, defined as the change in length of a line Δl divided by the length of the line l. For uniaxial compression, the longitudinal stress in the primed frame can be denoted as $\sigma_{11}^{/}$ and the strain as $\theta^{/}$, in the manner discussed for finite-strain models. The linear elastic constitutive relations implied by Eq. 2.37 can be represented by two limiting strain definitions, which are equivalent at infinitesimal strain but diverge at large strain: $\theta^{/}=(\rho/\rho_0-1)$ and $\theta^{/}=(1-\rho_0/\rho)$. The latter of these is equivalent to the definition of a linear medium, after Thurston [108].

At infinitesimal strain, the finite strain tensors ε_{ij} and η_{IJ} reduce to the classical strain tensor θ_{ij}, and it is plausible that the longitudinal stresses in Lagrangian and

Eulerian treatments (e.g. $\sigma_{11}^{/}(\eta^{/})$ and $\sigma_{11}^{/}(\varepsilon^{/})$ in Eqs. 2.32-2.34) will converge with the linear infinitesimal strain relation 2.37 and with each other. It may be further postulated that at infinitesimal strain, the higher-order terms of the finite strain relations will be negligible; that is, these relations can be represented reliably at small strain by eliminating all higher-order terms in the expansion, leaving only the second-order term.

However, the above is not the case for several reasons, which are illustrated graphically in Fig 2.4, using the example of <111> uniaxial strain in diamond. It can be seen in this representative case that the various constitutive relations do not exhibit a unique linear elastic dependence at smalls strain to which all relations converge. Evidently, subtle differences in the strain definitions ε, η, and θ, are enough to perturb the predicted shock response even at infinitesimal strains. Additionally, the leading factors (ρ_0/ρ) and $(\rho/\rho_0)^3$ in the Lagrangian and Eulerian descriptions of $\sigma_{11}^{/}$, respectively, are significant at all but zero strain and contribute to the divergence of these formulations from each other and from the linear relations, which contain no prefactors. Finally, as evidenced by the third-order models in Fig. 2.4, higher-order terms are never negligible in the finite strain expansions, as they contribute significantly to the constitutive response even for small strain.

Furthermore, it is clear from Fig. 2.4 that the only way for Eulerian and Lagrangian finite-strain formulations to converge at any compression is when expanded to at least the third order in strain.

Discussion:

In studying the results of Figs. 2.1, 2.2, and 2.3 for sapphire, quartz, and diamond, it appears that, in general, fourth-order elastic effects must be accounted for in descriptions of uniaxial strain elastic shock data, regardless of whether a Lagrangian or Eulerian strain formalism is used. This conclusion remains convincing even if consistency with independent measurements of the third-order elastic constants is not required, as is illustrated by the case of *c*-cut quartz. The main features of this conclusion are as follows:

i) Third-order finite strain fits tend to be unrealistic, regardless of whether third-order elastic parameters are taken from the literature, or whether these parameters are fit to the data. The failure of third-order models, using literature third-order elastic constants, is visible in both quartz and diamond for most crystallographic orientations. The failure of third-order models with fitted third-order constants is most apparent in quartz; in *c*-cut quartz, where the data is of the highest precision and extends over the entire elastic compression range, the E3 fit and L3 fit models clearly fail to represent the data; in *a*-cut quartz, the E3 fit model has an unphysical high stress extrapolation, with a strongly negative slope in D-u space. In fact, most third-order models exhibit negative D-u and P-ρ slopes at high u and ρ, beyond the graph limits in Figs. 2.1-2.3 and 2.4. The unphysical high-pressure behavior of Lagrangian third-order models was observed previously [78, 109, 110], though the interpretation presented by those studies – that this behavior is related to fundamental material strength – is not well supported.

ii) Fourth-order finite strain fits, overall, seem to provide the best representation of shock data. In most cases, the fourth-order fits are similar in both the Lagrangian and Eulerian formalisms and both represent the data equally well. The most stringent test at present is *c*-cut quartz, which features the highest precision low-stress data, and clearly shows that both Lagrangian and Eulerian fourth-order descriptions fitting the curvature of the low stress data, as well as the more scattered high-stress results.

iii) The differences between Eulerian and Lagrangian models – whether third- or fourth-order, are often substantial, such as in the case of the fourth-order models for *a*-cut quartz. Thus, despite the small strains of only a few percent being considered here, it is not appropriate to treat the Lagrangian and Eulerian models as equivalent. It is possible that future high-precision measurements of elastic Hugoniots will serve to discriminate between these strain formalisms, but there is no convincing reason to select one over the other based on the uniaxial-strain data analyzed here.

iv) A possible exception to the viability of fourth-order elastic models can be found in <110> diamond, where the best-fit Eulerian (L4) model shows a negative trend in shock velocity with increasing particle velocity. However, as suggested by the measurements (Chapter 1) and by molecular dynamics calculations [74], a weak or flat scaling of shock speed with stress in this orientation may not be entirely unreasonable. Furthermore, as the elastic constants of diamond may be improved on in the future, this observation is tentative.

Given that third-order Eulerian elasticity is usually sufficient to describe hydrostatic compression to strains of many tens of percent, it may be surprising that fourth-order elasticity is necessary for uniaxial strains to only a few percent.

The appearance of higher-order effects in uniaxial strain could result from fundamental differences in the behavior of matter under finite uniaxial strain and finite hydrostatic strain. First, during hydrostatic compression, crystal structures often remain constant on compression or experience relatively small changes in unit cell parameters, provided there is no phase transition, whereas uniaxial strain forces the crystal structure to undergo a change in symmetry on compression. For example, a cubic crystal under uniaxial strain becomes tetragonal when strained in the <100> direction, orthorhombic under strain in the <110> direction, and trigonal under strain in the <111> direction. Secondly, under anisotropic stress and strain, the stability of different crystal structures could be altered from that known for hydrostatic conditions, and anisotropic-strain-specific phase transitions are possible [111-116]. Thus, elastic descriptions based on the ambient crystal structure may fail to describe the material at finite uniaxial strain, which could manifest as an appearance of strong higher-order effects in finite strain descriptions.

Finally, it is possible that the combination of elastic constants, including fourth-order constants, that define the second pressure derivative of the bulk modulus in hydrostatic compression, $\partial^2 K / \partial P^2$ [65], are such that the effect of fourth-order elasticity is minor in hydrostatic strain relative to uniaxial strain, in which the equivalent fourth-order elastic terms can be quantitatively more significant. This is certainly the case with the relative magnitude of the third-order elastic contribution in hydrostatic and uniaxial strain, as shown in Fig. 2.5. That is, at a given volume compression, the difference

between linear elastic models and nonlinear elastic, third-order models are sometimes significantly larger under uniaxial strain compared to hydrostatic strain. It is possible that the same may be true for the differences between third- and fourth-order terms. This interpretation is consistent with certain orientations of uniaxial strain (e.g. diamond <110>) showing very little fourth-order contribution whereas others (e.g. diamond <100> and <111>) show significant contributions. However, without a complete set of fourth-order constants, it is not possible to evaluate this possibility quantitatively.

The necessity of including fourth-order elasticity in treatments of uniaxial strain complicates the application of finite strain models to define the full stress state of shock compressed systems. That is, while empirical fourth-order models can describe the elastic Hugoniots of highly nonlinear elastic materials, they are unable to predict lateral stresses, as the required fourth-order constants – or the appropriate combinations thereof – are not measured or known independently.

Conclusion

In contrast to hydrostatic compression experiments, where Eulerian third-order finite strain models are often sufficient to represent compression data to many tens of percent in strain, it appears that third-order elasticity – whether in the Eulerian or Lagrangian approach – is insufficient to regularly describe uniaxial strain compression data to even a few percent in strain. By extending the Eulerian and Lagrangian finite-strain models to fourth order, both finite strain approaches can agree satisfactorily with existing measurements. Despite the relatively small strains discussed here, the quantitative differences between Lagrangian and Eulerian approaches are significant and

independent elasticity measurements combined with high-precision elastic shock-wave experiments are needed to further discriminate between these models.

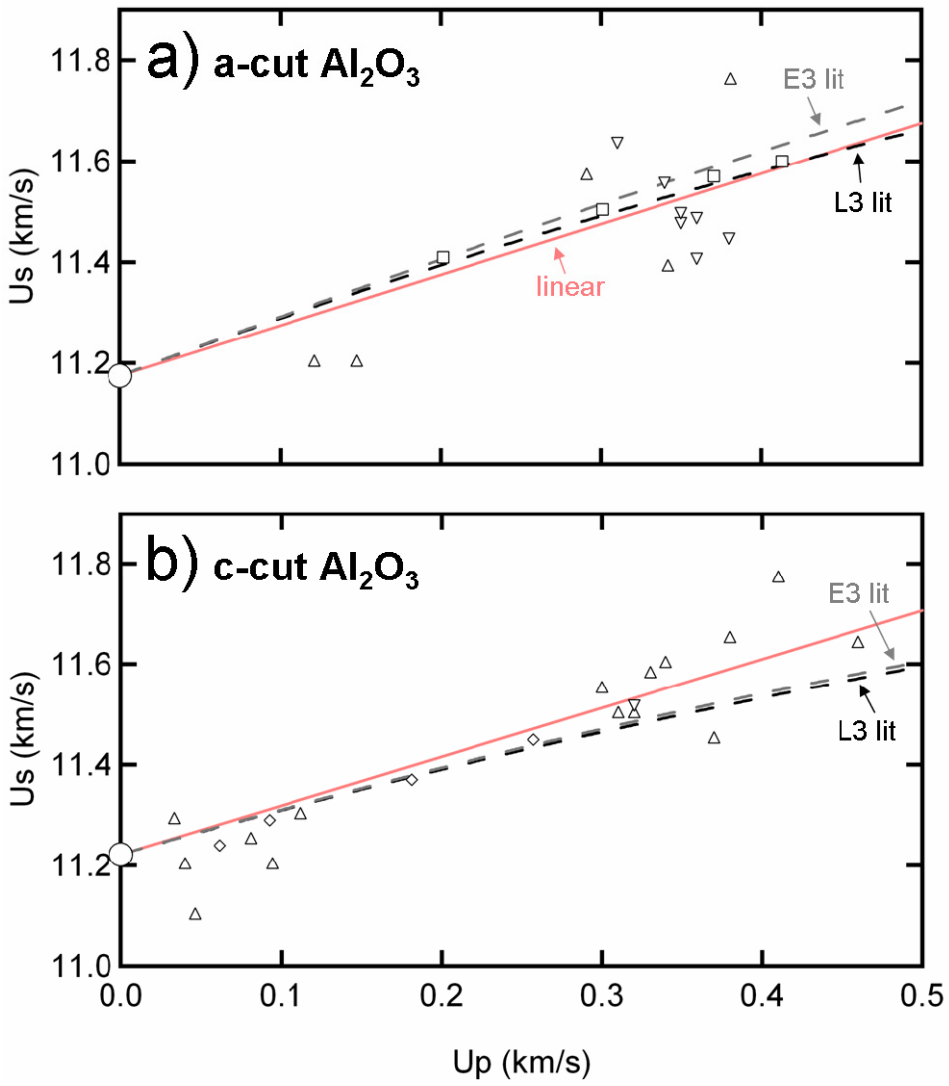

Figure 2.1. Sapphire elastic shock data and finite strain theories for uniaxial strain in (a) *a*-axis and (b) *c*-axis directions. Shock data is from [18] (upward triangles), [100] (downward triangles), [99] (squares), and [33] (diamonds). Large circles are ambient sound speeds taken from the elastic constants [90] and Eq. 2.18.a. Black dashed line is a Lagrangian third-order strain model (L3 lit) and the grey dashed line is an Eulerian third-order strain model (E3 lit), with the third-order elastic constants are taken from the literature [89] and Eq. 2.16. Red line is a linear fit to the data. Third-order elasticity is sufficient to describe this material, given the precision of the measurements.

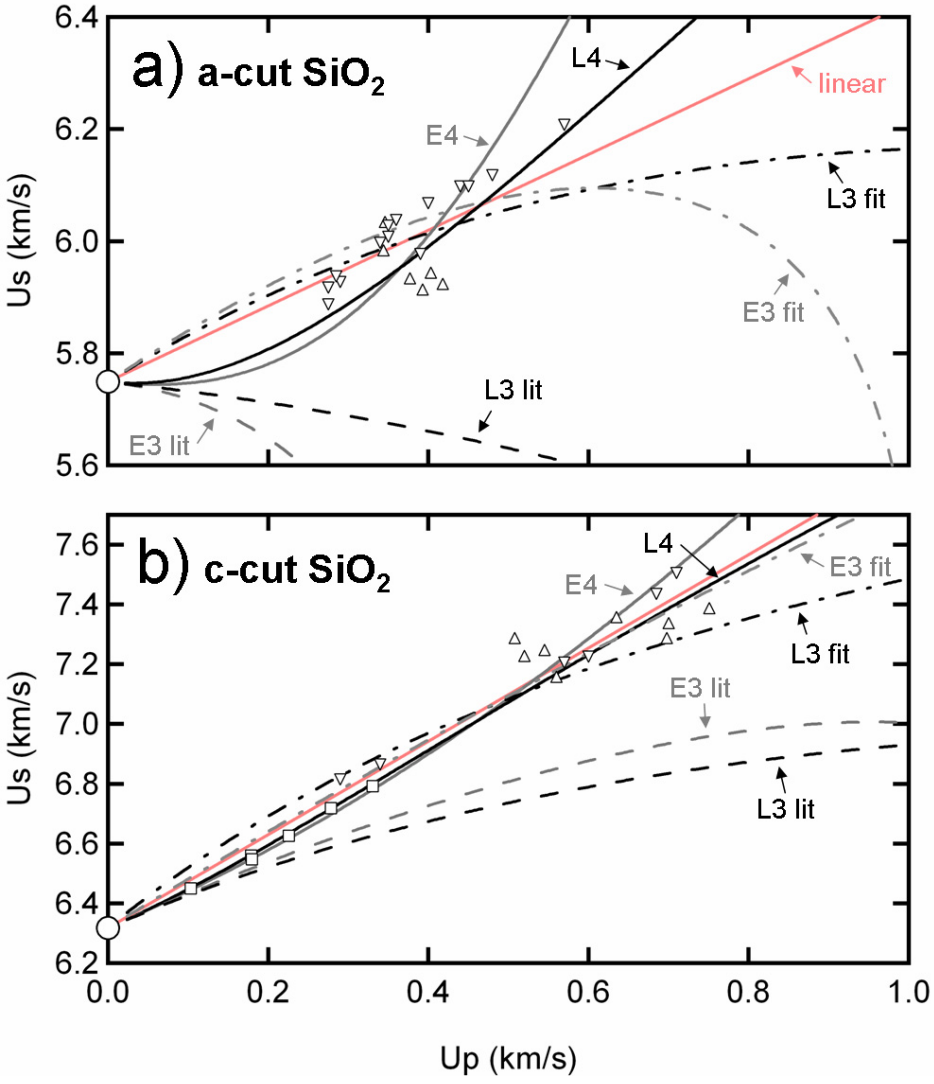

Figure 2.2. Quartz elastic shock data and finite strain theories for uniaxial strain in (a) *a*-axis and (b) *c*-axis directions. Shock data is from [46] (upward triangles), [45] (downward triangles), and [41] (squares). Large circles are ambient sound speeds taken from the elastic constants [92] and Eq. 2.18.a. Black lines are Lagrangian (L) strain models, grey lines are Eulerian (E) models, red line is a linear fit. Dashed lines (L3 lit, E3 lit) are third-order models with the elastic constants taken from the literature [91] and Eq. 2.16. Dashed-dotted lines (L3 fit ,E3 fit) are third-order models with the third-order parameter fit to the data. Solid lines (L4, E4) are fourth-order models with the fourth-order constant fit to the data [41, 46] and the third-order constants taken from the literature. For *c*-cut quartz, the data of [41] is very precise, and only fourth-order models can reasonably agree with this data and the higher stress, less precise measurements.

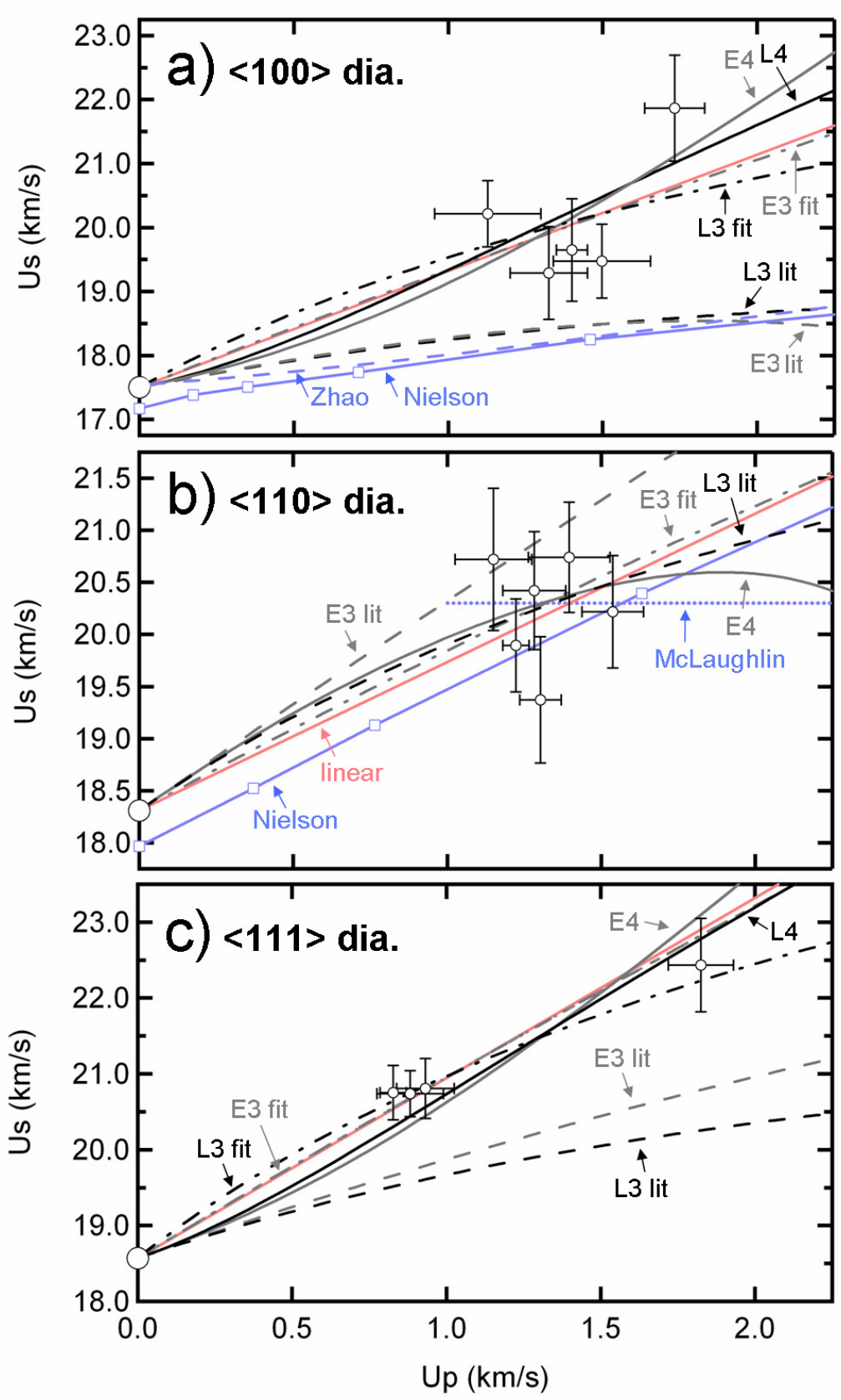

Figure 2.3. (caption on next page)

Figure 2.3. Diamond elastic shock data and finite strain theories for uniaxial strain in (a) <100>, (b) <110> and (c) <111> directions. Data is from Chapter 1. Large circles are ambient sound speeds taken from elastic constants [49] and Eq. 2.18. For finite strain theories, line types and notations are the same as in Fig. 2.2. Third-order literature elastic constants (L3 lit, E3 lit, L4, E4) are taken from ref. [58] and Eq. 2.15. Blue lines are computational results of Nielson [70, 107] (solid line and blue squares), Zhao [12] (dashed line), and McLaughlin [74] (dotted line). In <100> and <111> diamond, higher-order elastic effects are needed to accurately represent the data, assuming the literature third-order constants are accurate. In <110> diamond, a third-order description with the literature third-order elastic constants is possible in the Lagrangian theory. Computational results are in reasonably agreement with the data in the case of <110> strain but diverge significantly in the case of <100> strain.

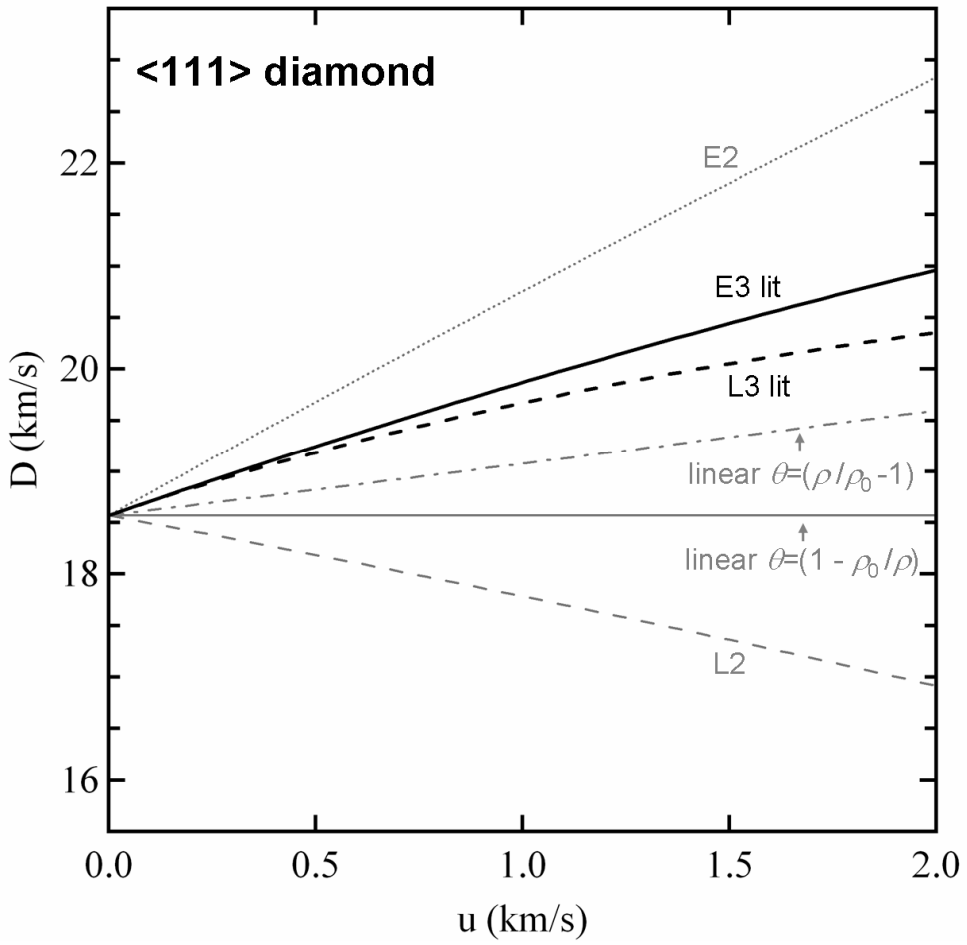

Figure 2.4. Comparison of finite strain theories to linear strain, in the representative case of <111> uniaxial strain in diamond. Linear strain expansions are given by Hooke's law with two extreme definitions of the strain (solid and dashed-dotted grey lines); the solid line is the definition of a linear medium [108]. The dotted and dashed grey lines are the Eulerian (E2) and Lagrangian (L2) models truncated to second order in strain. The "E3 lit" and "L3 lit" models are the same as in Fig. 2.3.c.

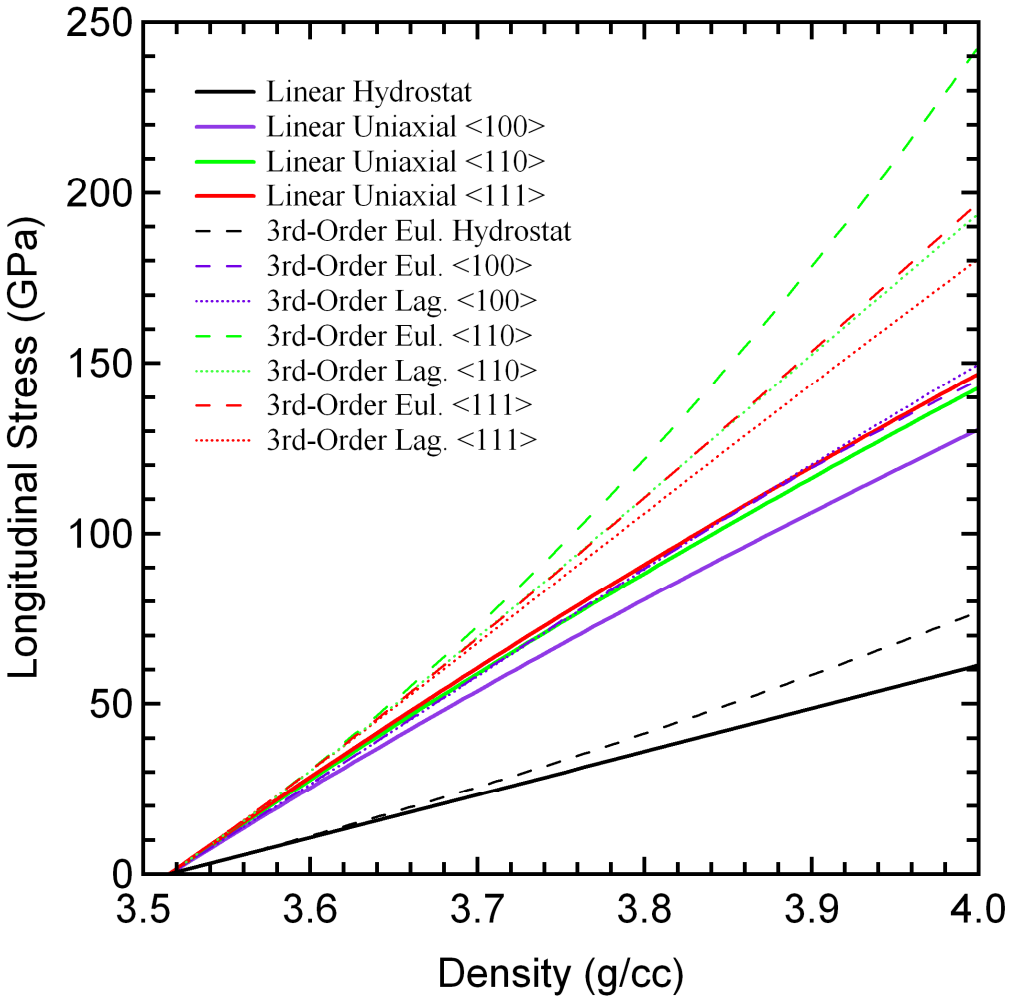

Figure 2.5. Comparison of linear elastic to third-order finite strain models for diamond. Solid lines are linear elastic predictions; solid black line is linear elastic hydrostatic model from the definition of the bulk modulus $K = \rho(\partial P / \partial \rho)$; solid red, green, and purple lines are linear elastic uniaxial strain models after Thurston [108], for <111>, <110> and <100>, respectively. Dashed lines are Eulerian third-order models; dotted lines are Lagrangian models. The third-order Eulerian model for hydrostatic compression is the Birch-Murnaghan equation (Chapter 1); the equivalent third-order Lagrangian model is not shown.

Chapter 3:

Optical properties of silica through the shock melting transition.

Abstract:

Under shock compression, α-quartz is found to transition from transparent to opaque and reflecting at a pressure of ~80 GPa on the Hugoniot. The VISAR index of refraction correction for transparent quartz at high pressure is found to be 1.16 (± 0.04). This is consistent with the expected high pressure index of refraction of silica. Quartz is thus found to be a good reference material for shock experiments using interferometric techniques to measure velocity, both below 80 GPa by virtue of its optical transparency and above 80 GPa by virtue of the reflectivity of the shock front.

Introduction:

The high pressure behavior of SiO_2 has long been of interest in the field of high-pressure physics and planetary science, due to the variability of its molecular structure under different pressure and temperature conditions and its ubiquity in planetary settings.

In shock research, silica has long been used as an optical window, at low pressures where silica is transparent [33, 41] and shock compression is elastic; and also at high pressures, where silica has been shocked into the molten and electronically conducting (metallic) regime [39, 40]. However, the transition from well-characterized transparent states at low pressure to opaque and reflecting states at high pressure has not been studied. Silica has also become important as an impedance-match standard for shock experiments due to its well-characterized Hugoniot [39, 40, 56, 117].

Here, we briefly review experimental observations on silica as it is shock compressed incrementally from its transparent state and into the reflecting regime, using α-quartz as a starting material.

Experiments:

Shock waves were generated in quartz samples using the JANUS laser at Lawrence Livermore National Laboratory. The details of this experiment are similar to those presented for diamond in Chapter 1 of this thesis. Phase plates of 1mm width were used to load a maximum area of the target. Pulse lengths of 6 ns were used for maximal shock steadiness. Dual VISAR channels were used to unambiguously characterize fringe shifts. The method of VISAR analysis was covered in Chapter 1.

The target design is shown in Fig. 3.1. Quartz samples were anti-reflection (AR) coated on the free surface so that weak reflections from within the shocked sample could be observed. The quartz was mounted on an aluminum disk having a step. The transit velocity of the step provides a check on the shock conditions in quartz through impedance matching. Quartz was mounted with transparent Stycast 1266 heat cure epoxy; the gap between the quartz and aluminum was up to several microns thick and filled with the epoxy. At high shock pressures, epoxy may become opaque, reducing or eliminating reflection from the aluminum. A gold layer (100 nm) was deposited directly on a section of the base of the quartz before mounting, to provide an ideal reflecting interface during the experiment. Gold was selected due to its high reflectivity and chemical inertness.

The primary means of establishing shock conditions in quartz was through velocity interferometry (VISAR). A VISAR record of a key experiment is shown in Fig. 1.2.a. The arrival of the shock varies slightly with position on the target due to variations in the plastic (CH) layer thickness; the shock is thus slightly tilted with respect to the

target and optics, which is accounted for in the analysis. Between events 1 and 2 in the VISAR record, reflected light is dominantly from the base of the quartz, from either aluminum or gold surfaces. Between 2 and 3, there is a transition to dominant reflection from the quartz shock front, as the intensity from the quartz base drops off due to extinction of light transmitted through a progressively thicker region of shocked quartz. After event 3, reflected light is entirely from the quartz shock front.

This representative experiment shown in Fig. 3.2 is analyzed in detail below. This experiment represents the culmination of a number of experiments on quartz at low and high pressures.

Measurements:

In this unique experiment, both the particle velocity (at the base of quartz) and the shock velocity (after reflection from the base of quartz is completely extinct) are visible. The shock velocity at the quartz shock front is measured absolutely, using the index correction for a reflecting shock $\chi = n_0 = 1.546$ in Eq. 1.1. The particle velocity at the base of quartz is not known *a priori*, as χ in this case depends on the high-pressure index of refraction of quartz, which has been previously measured only at low pressures [41]. The nearly simultaneous observation of the shock front velocity D_Q with the apparent velocity u_a of the quartz base (defined as the velocity obtained by setting $\chi = 1$) allows us to measure χ, and also the high-pressure index of refraction of quartz.

The apparent velocities and the true velocities in this experiment are shown in Fig. 1.2.b. The velocity of the quartz shock front indicates that the pressure of this experiment is ~80 GPa. This is consistent with the conditions expected from impedance matching

from the aluminum, in which conditions were measured by step transit. Since the shock is somewhat unsteady, the condition at the quartz shock front is not directly related to the condition observed at the base. Specifically, we can write the following relationship between the time of measurement of D_Q at the shock front ($t_{shock\ front}$) and the time at the base at which the corresponding particle velocity u_Q can be observed (t_{base}).

$$t_{base} = \left(\frac{c_Q + u_Q - D_Q}{c_Q} \right) t_{shock\ front} \qquad \text{(Eq. 3.1)}$$

where c_Q is the sound speed in quartz. At 80 GPa, the sound speed in quartz has been measured to be 12 to 14.5 km/s [118]. The first visibility of the shock front occurs at t = 1.6 ns after shock breakout; D_Q = 8.19 (± 0.06) km/s at this time. The corresponding time at the base at which to measure particle velocity is t=1.01-1.11 ns through Eq. 3.1, where u_Q is determined from the quartz Hugoniot [56] and D_Q. At this time, the apparent velocity u_a at the quartz base is 4.35 (± 0.15) km/s. Then, considering that $\chi = u_a/u_Q$, we find that χ = 1.16 (± 0.04) for transparent quartz at ~80 GPa. This is close to the low-pressure correction, χ = 1.08 [41].

The index correction is related to the index of refraction through [119]

$$n = \alpha + (n_0 - \alpha)\frac{\rho}{\rho_0} \qquad \text{(Eq. 3.2)}$$

where the density ρ ~ 4.87 g/cc at 80 GPa, and the initial density of quartz ρ_0 = 2.65. This formula gives n = 1.90 (± 0.08) as the high-pressure index of refraction of quartz.

In addition to the index of refraction, we are also able to determine other optical characteristics of quartz at high pressure, specifically the reflectivity of the shock front and the degree of transparency of shocked quartz. These are measured by tracking the intensity of VISAR fringes with time. Due to variation in the VISAR laser-probe

intensity, the fringe intensity has to be normalized to this variation before any quantitative intensity measurements are made.

The degree of transparency was analyzed by the Beer-Lambert law

$$T = e^{-\alpha L} \qquad \text{(Eq. 3.3)}$$

where T is the fraction of transmitted light through a distance L in a material having a coefficient of attenuation α. The Beer-Lambert parameter α was calculated by tracking the decay in VISAR fringe intensity between events 1 and 2 in Fig. 3.2. This decay was due to two-pass absorption through an increasing thickness of shocked quartz with time. We use the formula

$$\alpha = -\frac{1}{2\Delta d}\ln\left(\frac{I_f - I_i}{I_i} + 1\right) \qquad \text{(Eq. 3.4)}$$

where initial intensity I_i and final intensity I_f are the fringe intensities measured at times t_i and t_f, respectively, and the change in shocked thickness between t_i and t_f is Δd. For a quasi-steady shock this is

$$\Delta d = \int_{t_i}^{t_f} \left[D(t) - u_i(t)\right] dt \qquad \text{(Eq. 3.5)}$$

using the time-dependent shock velocity $D(t)$ and interface velocity $u_i(t)$. Reflection in the two-pass method occurred from the shocked base, off either gold or the aluminum/epoxy interface. The gold layer was used specifically to avoid problems with glue becoming opaque at high pressure, preventing reflection from the aluminum, and also to minimize the possibility of reactions at the base of the quartz, which could affect optical properties. The above analysis assumes that the reflectivity of the base remains constant in time and that α is constant throughout the shocked sample and in time:

reasonable approximations for this quasi-steady shocked system. At 80 GPa, we measure $\alpha = 0.12\ (\pm\ 0.03)\ \mu m^{-1}$.

Shock-front reflectivity is calculated by the absolute magnitude of reflected light after event 3 in Fig. 3.2, compared with the initial reflectivity from the base of the quartz. Initial reflectivity of surfaces was calculated to be ~87% for aluminum against Stycast 1266 epoxy (region QA in Fig. 3.2) and 72% for gold against quartz (region QG), using the Fresnel relation described below.

Discussion:

As shown in Fig. 3.3, the index of silica at these conditions compares reasonably well with the index of refraction of the high-density silica polymorph stishovite [120], first principles predictions of the high-pressure index of stishovite [121], and extrapolation of low pressure behavior [33, 41, 120].

The source of opacity – and reflectivity – in these experiments is also of interest. The loss of transmitted light at λ = 532 nm, parameterized by the Beer-Lambert coefficient α, could be due to either electronic absorption processes, scattering from heterogeneities (e.g. shear bands [122]), or both. If light-loss is entirely due to absorption in the material, then α is the absorption coefficient and is related to the extinction coefficient k by

$$k = \frac{\alpha\lambda}{4\pi} \qquad \text{(Eq. 3.6)}$$

With the index of refraction n, k is related to the reflectivity of a planar interface with a dielectric of index n_0 and $k_0 \approx 0$ (such as a gas where n_0=1, or unshocked quartz ahead of the reflecting shock front, where n_0=1.546) through the Fresnel equation

$$R = \frac{(n - n_0)^2 + k^2}{(n + n_0)^2 + k^2} \qquad \text{(Eq. 3.7)}$$

The shock reflectivity measured directly here at ~80 GPa is R = 2.3 (± 0.6)%. This is slightly higher than was reported previously at these conditions, R = 0.5 (± 0.2)% [40]. If k = 0 – that is, if all loss of light in transmission is due to scattering – then we calculate R=1.1 (± 0.4)% from Eq. 3.7. If k is nonzero, we may estimate its maximum magnitude by assuming all extinction associated with the Beer-Lambert coefficient is due to absorption; hence, that Eq. 3.6 applies, giving k = 0.0051 (± 0.0013). The effect of this on the calculated reflectivity is negligible.

The value of reflectivity determined from direct measurements of the shock front and that predicted from the high-pressure index of refraction appear to be relatively consistent; however, these measurements differ beyond their uncertainties. This is likely due to the difficulty in measuring shock reflectivity, particularly at the percent-level. Meanwhile the magnitudes of n and k are better constrained, particularly the observation that k must be negligible in the calculation of reflectivity. Thus we conclude that, at stresses of about 80 GPa, the shock reflectivity is due entirely to the increase in the index of refraction of silica at high pressure.

Based on the above analysis, it is not clear whether the mode of transparency loss at 80 GPa is due to absorption, scattering or some combination of the two. However, above 80 GPa, quartz is totally nontransparent – transmitted light is completely attenuated after shock-breakout into quartz, on a timescale faster than the resolution of our diagnostics.

Above ~100 GPa, quartz becomes entirely molten (and hence, homogenous) [40, 117] and light should not be scattered in such a medium, indicating that absorption is the most likely mechanism for nontransparency at these conditions. Also, the reflectivity of the shock front begins increases considerably, exceeding several percent at a few hundred GPa. The rising reflectivity is correlated with progressive chemical dissociation of liquid silica and a rise of electronic conductivity with pressure and temperature [40], consistent with the conclusion that electronic absorption is the dominant cause of optical extinction in the molten state.

It is interesting to note that the loss of transparency occurs at or near the shock-melting transition. Sound-velocity data appear to show melting beginning above ~90 GPa, and a shock temperature anomaly (superheating) suggests that melting occurs over a small range in shock pressure at ~110 GPa [118]. Given observations on other materials, such as diamond, which transition from an insulator to a metal upon shock melting [6, 36, 37], it is possible that a similar phenomenon is occurring in quartz. The appearance of strong absorption below the melt transition could be related to the presence of thin, molten shear bands in solid silica, which form to accommodate shear-stress relaxation behind the shock front [22, 122].

Conclusion:

We have verified that quartz changes from transparent to opaque in the vicinity of its melting transition. The loss of transparency correlates with the appearance of measurable reflectivity at the shock front, ensuring that quartz is a good reference window for shock experiments over its entire Hugoniot. However, shock-front

reflectivity at pressures of ~80 GPa is caused by an increase in the index of refraction of silica at high pressure, and is not related to the loss of transparency – that is, the reflectivity increase is not due to a change in the electronic conductivity of silica at pressures of ~100 GPa. This contrasts with the higher-pressure behavior of SiO_2, in which electronic conduction plays a strong role in the reflectivity.

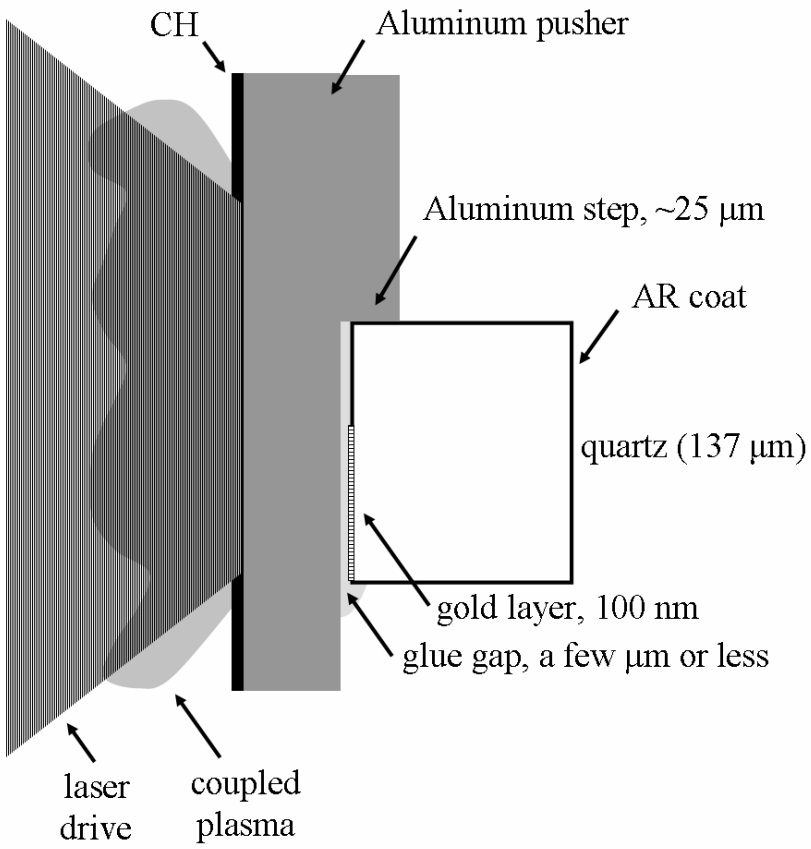

Figure 3.1. Quartz target design. The quartz window was AR-coated on the free surface, and partially coated with 100 nm of gold on the base; it was attached to an aluminum base with Stycast 1266 heat-cure epoxy. The aluminum base was diamond-turned, with a 25 μm step; base thickness was 50 μm on the low side on which the quartz was mounted; 10-15 μm of plastic (CH) was deposited on the drive side of the base for optimum coupling to the laser pulse.

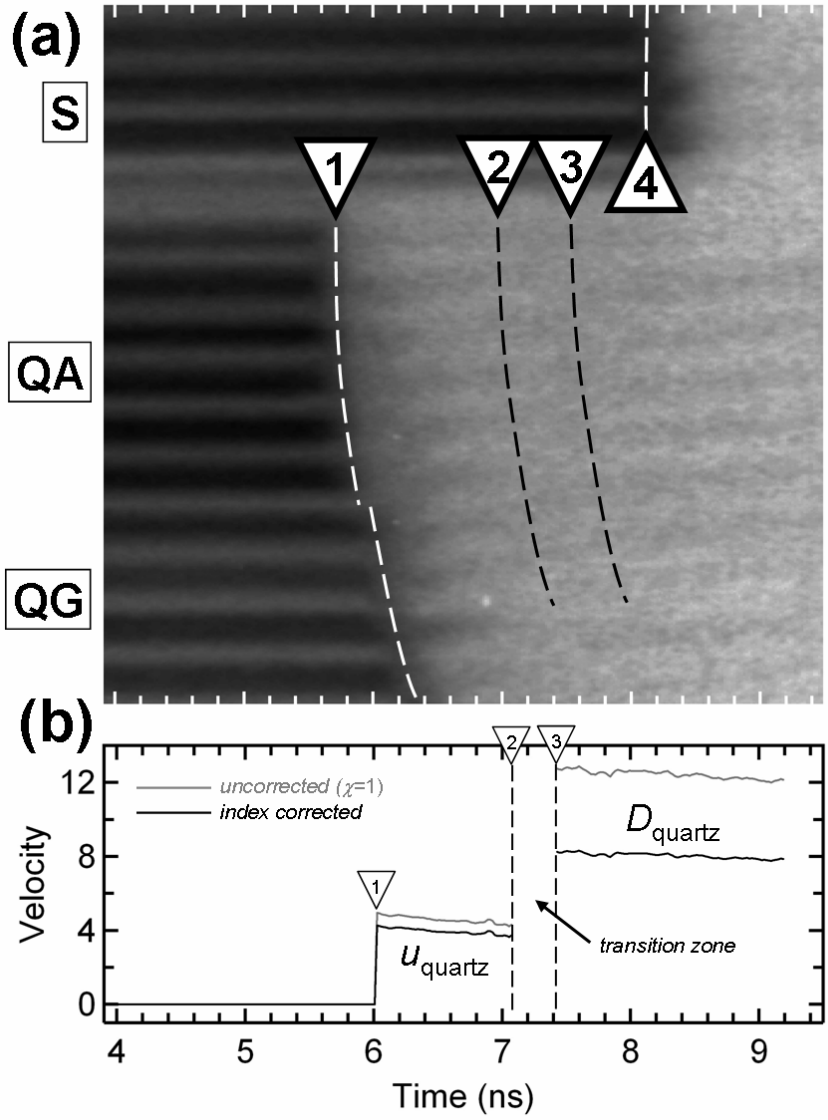

Figure 3.2. Experiment on alpha-quartz at the boundary between transparent and opaque on the Hugoniot, P ~ 80 GPa. (a) VISAR image of shot qug3. Spatial dimension (vertical) is about 800 microns fullscale. Region S: aluminum step; region QA: quartz on aluminum with glue interlayer; region QG: same as QA with gold layer directly deposited on quartz. Events are 1: breakout from aluminum base, step in breakout due to gap between parts; 2: reflection from base has dropped and become equal to shock reflectivity; 3: only quartz shock front reflection visible; 4: shock in aluminum breaks out of step. (b) velocity record, corrected for timing variations with spatial position. Velocity in transition zone (between events 2 and 3) is undefined due to equal reflection from base and shock front, which blurs the VISAR interference pattern due to unequal velocities. The shot energy was 265 J, the pulselength 6 ns and the phase plate 1mm in width.

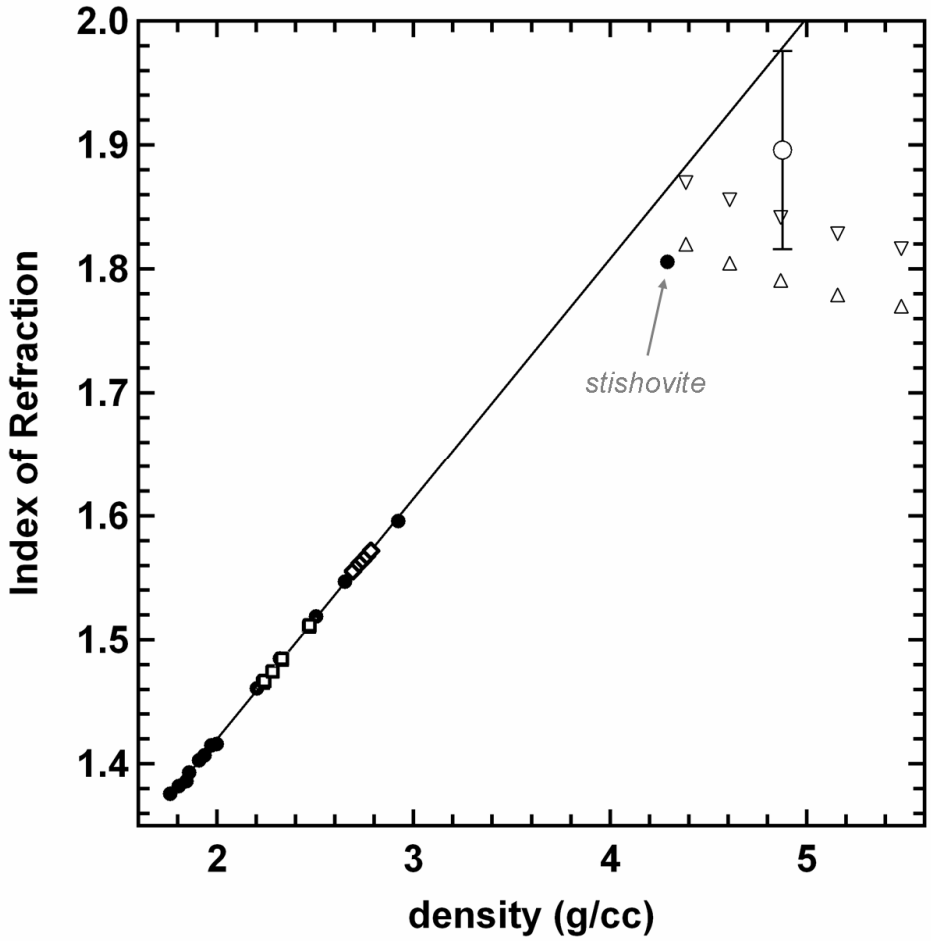

Figure 3.3. Index of refraction of SiO_2 vs. density. Dark circles are index of silica polymorphs reported by Marler [120]. Open squares and diamonds are shock data on fused silica [33] and α-quartz [41], respectively. The highest-density silica polymorph, stishovite, is octahedrally-coordinated and diverges from the linear behavior of the tetrahedrally-coordinated polymorphs at low density, given by the line. First principles predictions of the index of stishovite are shown for the *x*- (upward triangles) and *z*- (downward triangles) axes [121]. Our measurement of the index of refraction of shocked quartz at high density is the open circle with the error bar.

APPENDICES

Appendix A: Evaluation of shock steadiness.

Due to the generally unsteady conditions of laser-driven loading, it is important to evaluate to what extent these laser-driven experiments are suitable for Hugoniot measurements, particularly those on the second wave, which could be significantly affected by variations in drive-pressure with time. The objective is to verify that ideal conditions of shock steadiness are achieved. In particular, we must be wary of the rarefaction wave, initiated on termination of the laser drive, catching up to the shock front on the experimental timescale. With sample-transit times of up to 12 ns, and laser drive pulses 1-6 ns in duration, unsteady loading, particularly in the form of shock attenuation, is observed to play some role in these experiments.

We have observed clear evidence of shock attenuation in experiments of 1- to 4-ns pulse duration. The shock conditions of these experiments have relatively larger uncertainties due to this effect, and should be considered approximate. Our main concern here is the analysis of quasi-steady, 6-ns pulse experiments.

The quartz window served as a reference for shock steadiness, by permitting direct observation of the velocity of the quartz shock front during the experimental timescale. In targets where free-surface reflectivity was too high to observe the shock velocity directly, the pyrometer still recorded shock thermal emission, allowing the relative steadiness or unsteadiness of the shock to be evaluated. For example, the difference between the 4-ns experiments and the 6-ns experiments at the same laser energy is clearly visible in the thermal emission records; in the 6-ns shots, emission

varies around a mean value during the experiment, while in the 4-ns shots, emission continuously decreases.

The unsteadiness in these experiments may feature rarefaction, ramp and reshock behavior, and is defined by a complicated interplay of laser-plasma coupling and target design. These details result in a state, that, even for experiments that have avoided rarefaction following the termination of the laser drive, exhibits some degree of temporal fluctuation in shock speed, stress and temperature.

Measurements of the quartz shock front conditions with time can constrain the steadiness of the shock in diamond via the following comparison. At time t_Q in the quartz, there is a time t_D in diamond at which the drive pressure variations experienced by the quartz shock front have also been experienced by the diamond shock front (where t_Q and t_D are zero at the time the shock breaks out of the aluminum base). This relationship can be expressed as:

$$t_Q = \left(\frac{c_Q}{c_Q + u_Q - D_Q} \right) \left(\frac{c_D + u_D - D_D}{c_D} \right) t_D \qquad \text{(Eq. A.1)}$$

where D_Q, u_Q and c_Q are the quartz shock speed, particle speed and sound speed, respectively, and D_D, u_D and c_D are the diamond shock speed, particle speed and sound speed. It has been assumed that a given pressure perturbation reaches the base of the quartz and diamond simultaneously. For most experiments here, quartz is shocked beyond its melting point [40], and c_Q can be given by the bulk sound speed $c_{B=}\sqrt{(dP/d\rho)_S}$; this can be estimated from the slope of the quartz Hugoniot in P-ρ space, or by measurements of the sound velocity at low stress [118, 123]. The choice of c_D depends on whether diamond assumes elastic behavior or fluid-like behavior during

sound propagation. For fluid-like behavior, c_D=c_B, which can be evaluated from the slope of the isentrope (Eq. 1.9) at the volume of the final shock state (Fig. 1.10). For elastic behavior, c_D can be estimated by assuming an isotropic elastic medium, for which the longitudinal sound velocity is $c_L=\sqrt{(K+4G/3)/\rho}$ (where K is the bulk modulus and G the shear modulus). Recognizing that $c_B=\sqrt{K/\rho}$ and G=3K(1-2υ)/2(1+υ) (where υ is Poisson's ratio) we have for diamond (υ~0.1) c_L=1.57c_B.

To illustrate the use of Eq. A.1, we consider the conditions of the steady-drive experiments at P_2 ~ 250 GPa in the present study, as given by shot *dh14* in Fig. 1.3.a. For c_D, we consider the extreme cases of bulk sound speed and elastic sound speed. This gives a relation of t_Q ~ 0.5 t_D for the bulk case and t_Q ~ 1.2 t_D for the elastic case. For thin (100 μm) targets, t_D = 6 ns after the inelastic shock transits the target; this corresponds to t_Q = 3 (7.2) ns for bulk (elastic) c_D, a ±2 (4)% velocity variation in the quartz shock front and a ±6 (11)% variation in stress at the front. To first order, we expect the same relative variation in stress at the diamond shock front to t_D = 6 ns. For thicker targets (200 μm), t_D = 12 ns after inelastic shock transit, corresponding to t_Q = 6 (14.4) ns, a variation in quartz shock velocity of ±5 (6)% and a variation on shock front stress of ±15 (16)%. In some cases, particularly for elastic c_D, it would be necessary to observe the quartz shock front beyond the end of the streak window, or after it arrives at the free-surface, for a full constraint on shock steadiness by this technique.

This effect of unsteadiness is accounted for in impedance-match analysis by considering an uncertainty in the reference conditions of quartz and aluminum that accounts for the above variations.

In the case of transparent quartz, the pressure variations at the base of the quartz are observed through changes in the particle velocity at this interface. The analogous relation to Eq. A.1 is

$$t_Q = \left(\frac{c_D + u_D - D_D}{c_D} \right) t_D \qquad \text{(Eq. A.2)}$$

Only a single shot in the present study exhibited a transparent shock in quartz, shot *dh6*.

Elastic precursor waves are not significantly affected by drive unsteadiness for most conditions studied here; instead, elastic waves vary in amplitude due to internal relaxation. Above the HEL, elastic waves propagate ahead of a slower, high-amplitude inelastic shock, into which pressure perturbations from the drive surface are absorbed as they propagate forward. These perturbations should alter the conditions of the inelastic wave, while the elastic precursor wave, insensitive the amplitude of the inelastic wave, behaves as it would under steady-loading conditions.

Appendix B: **Relationships between Lagrangian and Eulerian third-order elastic constants.**

Analytical Approach

Birch [83] suggested an analytic means of obtaining relations between Lagrangian and Eulerian elastic constants, as he was aware that typically only the Lagrangian constants are known. In that work, he obtained partial relations between the third-order Eulerian elastic constants, D_{mno}, and the third-order Lagrangian elastic constants C_{MNO} for a cubic system. The relations obtained in that study are not completely correct due to his use of antiquated third-order elastic constant notation [82, 87] in his free-energy expansion (Eq. 12 in that study). With a modern version of Birch's Eq. 12 (Eq. 2.14 here) and using new strain systems defined in the present study (uniaxial strain in <100>, <110> and <111> directions), we extend Birch's analysis to obtain complete relationships between the Lagrangian and Eulerian elastic constants for a cubic crystal, given in Eq. 2.15.

First, consider the internal energy expansions for Lagrangian and Eulerian strain in Eqs. 2.10.a and 2.10.b. For a given strain, Birch postulated that the internal energies should be equivalent. The Lagrangian and Eulerian definitions of strain used in these expansions (Eqs. 2.2 and 2.3) cannot be immediately equated, and we will consider a more fundamental (absolute) definition of strain that circumvents the differences in these strain definitions to allow different order terms in the energy expansions to be equated. These can be obtained as follows.

Birch considered a system of hydrostatic compression with slight infinitesimal offsets from pure hydrostaticity. The coordinate displacements in this system were written as

$$\begin{aligned} x_1 &= (1-\alpha)[(1+\beta_{11})a_1 + \beta_{12}a_2 + \beta_{13}a_3] \\ x_2 &= (1-\alpha)[\beta_{12}a_1 + (1+\beta_{22})a_2 + \beta_{23}a_3] \\ x_3 &= (1-\alpha)[\beta_{13}a_1 + \beta_{23}a_2 + (1+\beta_{33})a_3] \end{aligned} \qquad \text{(Eq. B.1)}$$

The inverse of this coordinate definition $a_I(x_j)$ can be obtained algebraically, but it is important to note that any second-order terms of β_{ij} should be retained for reasons that will be explained later. In this system, α describes the uniform (isotropic) strain, and the β_{ij} describe small anisotropic perturbations from the isotropic strain state.

Eq. B.1 and its inverse determine the Lagrangian and Eulerian strain through Eqs. 2.2 and 2.3. Thus, the internal energy expansions in Eq. 2.10 can be rewritten as functions of the strain parameter α and the perturbations β_{ij}. Significant algebra reduces these strain-energy functions to terms consisting of different powers in α and β_{ij}.

As we are only interested in the third-order parameters, the internal energy expansions are truncated at the third order in Eulerian and Lagrangian strain. However, this does not correspond to truncation at the third order in the strain parameter α, as can be seen when the expansions are written in terms of α. A large number of higher-order terms in α appear. For the lowest order in α, only the second-order elastic constants are involved. For the next highest order in α, both the second- and third-order constants are involved. For the next-highest order in α, second-, third- and fourth-order constants will be involved, and so on. The numerous higher-order terms arising in this treatment, however, contain only the contributions from the second- and third-order elastic constants,

due to the initial truncation, and are thus missing the contribution from fourth-order and higher elastic constants. That is, the higher-order terms represent incomplete contributions from higher-order elasticity, and so we are limited to looking only at the first two orders in α.

Next, the system can be specified to have a variety of strain configurations. The simplest is that all $\beta_{ij} = 0$: in other words, the system is under hydrostatic stress. This reduces the Eulerian and Lagrangian strain energy formulae to a small number of terms. Terms of identical order can then be equated. In this case, we find that

$$D_{111} + 2D_{123} + 6D_{112} = 12C_{11} + 24C_{12} + C_{111} + 2C_{123} + 6C_{112} \qquad \text{(Eq. B.2)}$$

Next, consider a system in which $\beta_{12} \neq 0$ and all other $\beta_{ij} = 0$. The strain-energy formulae are compared again, and we find

$$D_{144} + 2D_{166} = 2C_{11} + 4C_{12} + 8c_{44} + C_{144} + 2C_{166} \qquad \text{(Eq. B.3)}$$

In this case, the terms being equated to obtain Eq. B.3 contain quadratic β_{12} factors, which is why we must retain quadratic β_{ij} terms during the course of the analysis.

Finally, consider a system in which $\beta_{11} \neq 0$ and all other $\beta_{ij} = 0$. This leads to

$$D_{111} + 2D_{112} = 12C_{11} + 8C_{12} + C_{111} + 2C_{112} \qquad \text{(Eq. B.4)}$$

where again quadratic β_{ij} appear in the terms being compared.

It seems that in forming these three relations we have exhausted the potential of the strain configuration defined by Birch (Eq. B.1) for the purposes of relating the Lagrangian and Eulerian third-order constants. Three more independent relations are needed to absolutely define the D_{mno} in terms of the C_{MNO} and C_{MN}. Fortunately, we have defined three additional strain configurations in this study, for uniaxial strain in <100>, <110> and <111> in a cubic crystal.

Now, instead of using B.1 and its inverse, we use Eqs. 2.24, 2.30 and 2.31 to define the Lagrangian and Eulerian strains in Eqs. 2.2 and 2.3, replacing the parameter γ with (1 - α) in analogy with Birch's treatment. As before, we rewrite the internal energy expansions Eq. 2.10 in terms of α, and equate like terms of α, ignoring incomplete higher-order terms. Note that the strain parameter α now describes uniaxial strain (as opposed to isotropic strain).

For <100> uniaxial strain we obtain

$$D_{111} = 12C_{11} + C_{111} \qquad \text{(Eq. B.5)}$$

For <110> we have

$$D_{111} + 3D_{112} + 12D_{166} = 24C_{11} + 24C_{12} + 48C_{12} + C_{111} + 3C_{112} + 12C_{166} \qquad \text{(Eq. B.6)}$$

and for <111> we have

$$\begin{aligned} &D_{111} + 6D_{112} + 2D_{123} + 12D_{144} + 24D_{166} + 16D_{456} = \\ &\quad 36C_{11} + 72C_{12} + 144C_{44} + C_{111} + 6C_{112} + 2C_{123} + 12C_{144} + 24C_{166} + 16C_{456} \end{aligned} \qquad \text{(Eq. B.7)}$$

Solving Eqs. B.2-B.7, we are able to define all D_{mno} as in Eq. 2.15.

The simplest uniaxial-strain configuration for a cubic crystal, that of <100> strain, is mathematically identical to uniaxial strain in certain high-symmetry directions of non-cubic crystals, such as *a*- and *c*-axis compression of trigonal crystals. The displacement equations are also given by Eq. 2.24, and consequently the Lagrangian and Eulerian strains Eqs. 2.2 and 2.3 and the strain-energy relations Eqs. 2.10.a and 2.10.b are identical in form to the case of <100> strain. Hence, as in B.5, we may write

$$D_{mmm} = 12C_{MM} + C_{MMM} \qquad \text{(Eq. B.8)}$$

for such high-symmetry directions, where *m* and *M* are Voigt pairs of indices, with *m,M* = 1 for the *a*-axis of a trigonal crystal, and *m,M* = 3 for the *c*-axis.

Computational Approach

We can also consider a computational means of obtaining the relationship between the Lagrangian and Eulerian third-order constants. In this approach, we generate the internal energy vs. strain function from Eq. 2.10.a using the known Lagrangian third-order constants, and find the best fit of this internal energy using Eq. 2.10.b, fitting for the third-order Eulerian elastic constants.

Considering the uniaxial-strain configurations, we have for <100> strain, expanded to third order, the following strain energy relation.

$$\rho_0\left[\phi(S,\eta)-\phi(S,0)\right]=\frac{1}{2}C_{11}\eta^2+\frac{1}{6}C_{111}\eta^3+\cdots \qquad \text{(Eq. B.9)}$$

This relation is identical to the Eulerian one with third-order C constants replaced by D. Note that the third-order term here contains only a single elastic constant, C_{111} or D_{111}, and hence, as in Fig. B.1, the D_{111} constant is determined by comparing the Lagrangian and Eulerian energy expansions.

For <110> and <111> strain, fitting can only resolve a combination of third-order Eulerian elastic constants, as in the third-order terms of the energy expansions

$$\rho_0\left[\phi(S,\eta)-\phi(S,0)\right]= \frac{1}{2}\left[\tfrac{1}{2}C_{11}+\tfrac{1}{2}C_{12}+C_{44}\right]\eta^2+\frac{1}{6}\left[\tfrac{1}{4}C_{111}+\tfrac{3}{4}C_{112}+3C_{166}\right]\eta^3+\cdots \qquad \text{(Eq. B.10)}$$

for <110> strain and

$$\rho_0\left[\phi(S,\eta)-\phi(S,0)\right]=\frac{1}{2}\left[\tfrac{1}{3}C_{11}+\tfrac{2}{3}C_{12}+\tfrac{4}{3}C_{44}\right]\eta^2 +\frac{1}{6}\left[\tfrac{1}{9}C_{111}+\tfrac{2}{3}C_{112}+\tfrac{2}{9}C_{123}+\tfrac{4}{3}C_{144}+\tfrac{8}{3}C_{166}+\tfrac{16}{9}C_{456}\right]\eta^3+\cdots \qquad \text{(Eq. B.11)}$$

for <111> strain.

Using a large number of strain configurations, as in the previous section of this Appendix, we might be able to use this technique to reveal all the individual elastic constants computationally. However, as shown in Fig. B.1, the agreement of the simpler analytical predictions with the computational results suggests that further work to this end is redundant, and less precise.

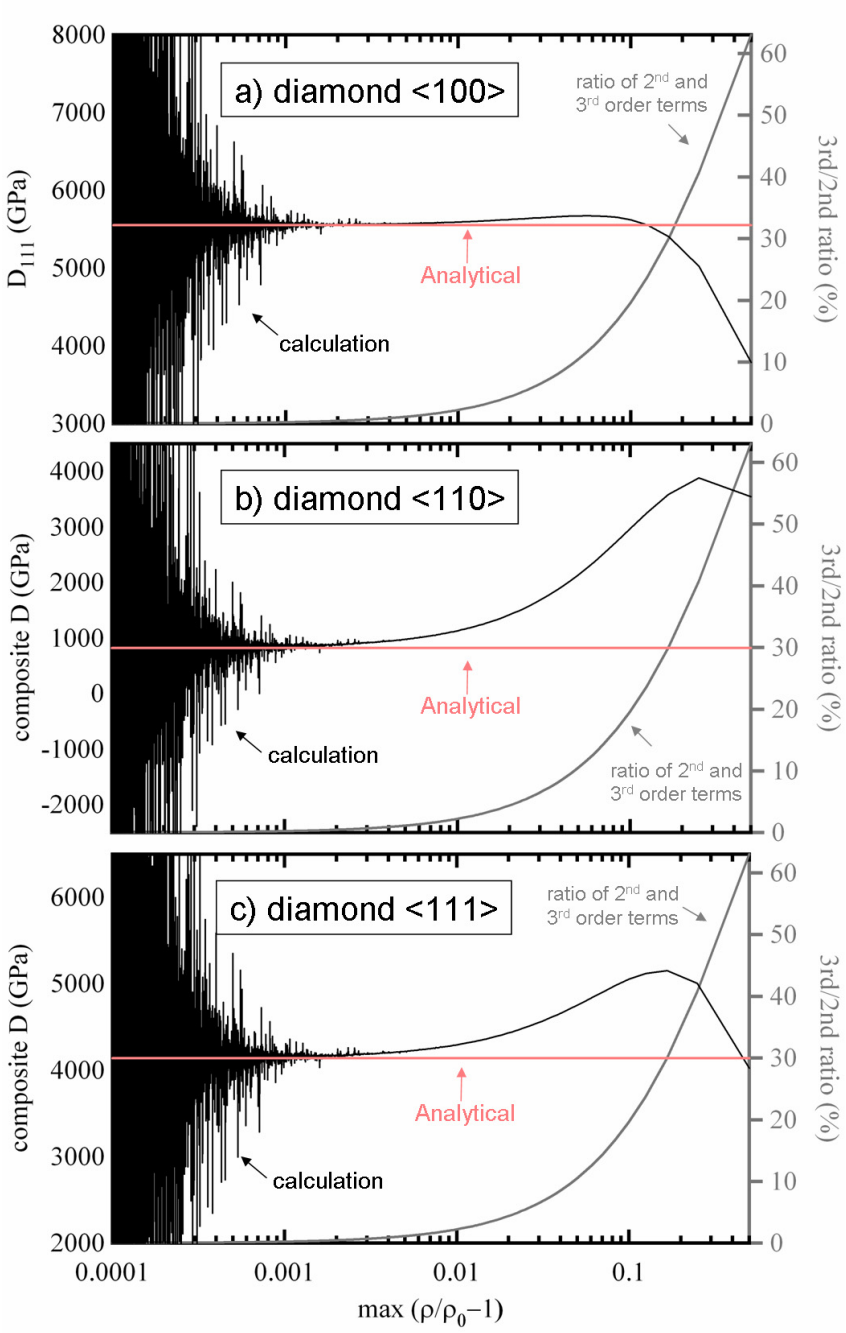

Fig B.1 Results of computational method to determine elastic constants for strain in the (a) <100>, (b) <110> and (c) <111> directions in diamond, plotted against the maximum strain used in the computation. The black lines show the computational results, which are highly uncertain at low strain. The red line is the result expected from the analytical approach discussed in the text. The grey line is the ratio (in %) of the magnitude of the third-order term to the second-order term in the energy expansion. As the third-order term approaches the magnitude of the second-order term, the agreement with the analytical approach degrades, which is expected since the computational approach implicitly assumes that each term in the energy expansion is negligible with respect to the lower-order terms.

Appendix C: Elastic Hugoniot Models in Polynomial Form

$$Us^{Linear}_{<100>} = 17.53 + 1.82Up$$
$$Us^{Linear}_{<110>} = 18.32 + 1.43Up$$
$$Us^{Linear}_{<111>} = 18.58 + 2.38Up$$

$$Us^{E4}_{<100>} = 17.53 + 0.7665Up + 0.9571Up^2 - 0.1197Up^3$$
$$Us^{E4}_{<110>} = 18.32 + 1.977Up - 0.225Up^2 - 0.09733Up^3$$
$$Us^{E4}_{<111>} = 18.58 + 1.316Up + 0.8412Up^2 - 0.1126Up^3$$

$$Us^{L4}_{<100>} = 17.53 + 1.121Up + 0.8569Up^2 - 0.1966Up^3$$
$$Us^{L3}_{<110>} = 18.32 + 1.980Up - 0.4401Up^2 + 0.04841Up^3$$
$$Us^{L4}_{<111>} = 18.58 + 1.629Up + 0.6627Up^2 - 0.1587Up^3$$

All finite-strain elastic Hugoniot models require a fourth-order term except for the Lagrangian model in the case of <110> compression, for which only terms to third order are needed. The development of these models is discussed in Chapter 2.

Appendix D: Corrections to the Pavlovskii Hugoniot

No report of elastic precursors or two-wave structures appeared in the earliest study of the shock response of single-crystal diamond by Pavlovskii [23]. Even ignoring the present measurements, this is highly suspicious, as the ambient longitudinal sound speed in the <100> orientation exceeds the reported shock speeds in that study for all but the highest stress datapoint. Because Pavlovskii's study has been frequently used in equation-of-state modeling, it is of interest to evaluate these measurements in light of the present results.

Here we attempt to re-interpret that data by accounting for the effects of the two-wave structure on Pavlovskii's experiment. In doing so, we make the following assumptions, in part due to limited information available regarding the experiment:

a) Elastic precursors and two-wave structures were present in Pavlovskii's experiments. We further assume that the elastic precursor did not trigger the electrical contact used to measure shock arrival, while the arrival of the inelastic wave did. Kondo and Ahrens [7] found that their electrical contacts did not respond to the first wave in diamond.

b) The apparent velocity of the inelastic wave reported by Pavlovskii, D_2' (after Eq. 1.6.d), would have been affected by the earlier arrival of the elastic precursor at the contact. To account for this effect, we assume that Pavlovskii's measurement used an electrical contact mounted on a free-surface of the diamond sample, a common arrangement for the study of brittle solids by Russian researchers of this time period [124, 125]. The effect of the elastic precursor on D_2' can then be assumed to take the form of the free-surface correction discussed earlier. Using Eqs. 1.6.a to 1.6.d, the corrected shock velocity D_2

can be found from Pavlovskii's measurement of $D_2^{/}$ and an assumed elastic precursor condition:

$$D_2 = \frac{D_1 D_3 (2D_2^{/} - D_1) + u_1 (2u_1 - D_3)(D_2^{/} - D_1) + D_1^2 D_2^{/} - D_1 u_1 (3D_2^{/} - 2D_1)}{D_1 (D_2^{/} + D_3 - 2u_1) + u_1 D_2^{/}} \quad \text{(Eq. D.1)}$$

Use of this correction assumes that the contact interacted negligibly with the free-surface reverberation, and that the free surface was in contact with vacuum. As for our measurements, we consider a range for D_3 of ($D_1 + 2u_1 \geq D_3 \geq D_2 + 2u_1$) in applying this correction. We also examined the alternative but less likely possibility that the electrical contact was embedded in the diamond. This correction has the form

$$D_2 = \frac{\rho_0}{\rho_1} D_2^{/} + u_1 \quad \text{(Eq. D.2)}$$

Again, it is assumed that the contact does not significantly interact with shock propagation. The correction implied by Eq. D.2 is not significantly different from that given by Eq. D.1.

c) We take the magnitude of the elastic precursor to be the lowest-stress value observed in the present study for the <100> orientation, P_1 = 80.12 (± 12.43) GPa. It does not significantly alter the results to account for precursor scaling with final stress; and, because Pavlovskii's experiments were of much longer duration that our own, it is reasonable to assume the precursor had relaxed to a minimum value during his experiment.

With these assumptions, Pavlovskii's original measurements were reanalyzed as follows. First, the initial iron driver conditions were recovered through impedance matching without a precursor state, using Pavlovskii's data and the iron Hugoniot [126]. The mirror reflection of the iron Hugoniot about the initial state was used to represent the

re-shock and release response. The iron-driver initial state was then impedance-matched to diamond with an assumed precursor state. The results are shown in Fig. D.1.

An uncertainty of 0.025 km/s was added to the iron driver reference shock velocities before impedance matching. However, the major sources of uncertainty in this approach, beyond any possible systematic errors due the assumptions made, are the uncertainty in the free surface correction, and the uncertainty in the precursor state. The relatively high precision of Pavlovskii's reported data is thus significantly reduced by this analysis.

While significant assumptions have been made here, we believe this is the best possible attempt to reinterpret the data of Pavlovskii without knowing further experimental details. Clearly questions remain. For example, we have ignored possible interactions of electrical contacts with the shock waves. For a variety of contacts used by Pavlovskii and his coworkers in the 1960s and 1970s for free-surface shock detection, this assumption may be inappropriate. For example, if the contact had sufficient mass and took up a sufficient area on the free surface, or if the contact was imbedded in a matrix such as paraffin coating the free surface, then a different correction would be called for which includes the impedance of the material lying on the surface. Furthermore, the nature of the detection, and how shock arrivals were selected, remains a mystery. It is unclear why two of the references [124, 125] provided by Pavlovskii for the experimental arrangement in [23] also are cited in a work on silicon and germanium by the same author [127], in which elastic precursors were detected. Thus, we must consider our corrections to be approximate, and, at least, illustrative of the errors likely

present in Pavlovskii's study. It is clear that even with this correction, Pavlovskii's results do not come into agreement with our own (Fig. D.1.a).

The highest-stress data-point in Pavlovksii's study is insensitive to correction for the elastic precursor. This is true if the elastic precursor is overdriven, which is the case if we use the lowest amplitude elastic precursor from the present study; it is also true when the scaling of precursor conditions with inelastic-wave conditions is considered, since $D_1 \sim D_2 >> u_1$ and, consequently, 2-wave impedance matching gives a similar result to 1-wave impedance matching (ignoring the precursor). Thus, we consider the highest-stress Hugoniot datum reported by Pavlovskii, at a stress of about 600 GPa, to be relatively accurate.

The corrected data of Pavlovskii show a strong offset from the hydrostat at low stress conditions, whereas at high stresses the data appear to converge with the hydrostat, suggesting strength is reduced at higher stresses. The relatively close agreement of Pavlovskii's original data with the hydrostatic response at low stresses (Fig D.1.b) is most likely spurious, given the magnitude of the errors suggested by the present correction.

Table D.1 Pavlovskii values corrected for the two-wave structure.

Pavlovskii (1971)			Assumed Elastic Limit				Corrected Pavlovskii Data							
shot	D_2' (km/s)	D_{Fe} (km/s)	D_1 (km/s)	δD_1 (km/s)	u_1 (km/s)	δu_1 (km/s)	D_2 (km/s)	δD_2 (km/s)	u_2 (km/s)	δu_2 (km/s)	P_2 (GPa)	δP_2 (GPa)	ρ_2 (g/cm^3)	$\delta \rho_2$ (g/cm^3)
1	14.18	6.994	20.22	0.52	1.128	0.173	13.96	0.49	1.839	0.074	113.9	5.5	3.94	0.06
2	14.94	8.065	20.22	0.52	1.128	0.173	14.82	0.37	2.655	0.068	157.7	5.6	4.18	0.06
3	17.33	11.08	20.22	0.52	1.128	0.173	17.37	0.10	5.102	0.041	320.0	4.1	4.92	0.04
4	20.50	14.53	... [a]		... [a]		20.50		8.200		590.9		5.86	

[a] precursor overun by plastic wave, results are pavlovskii's original

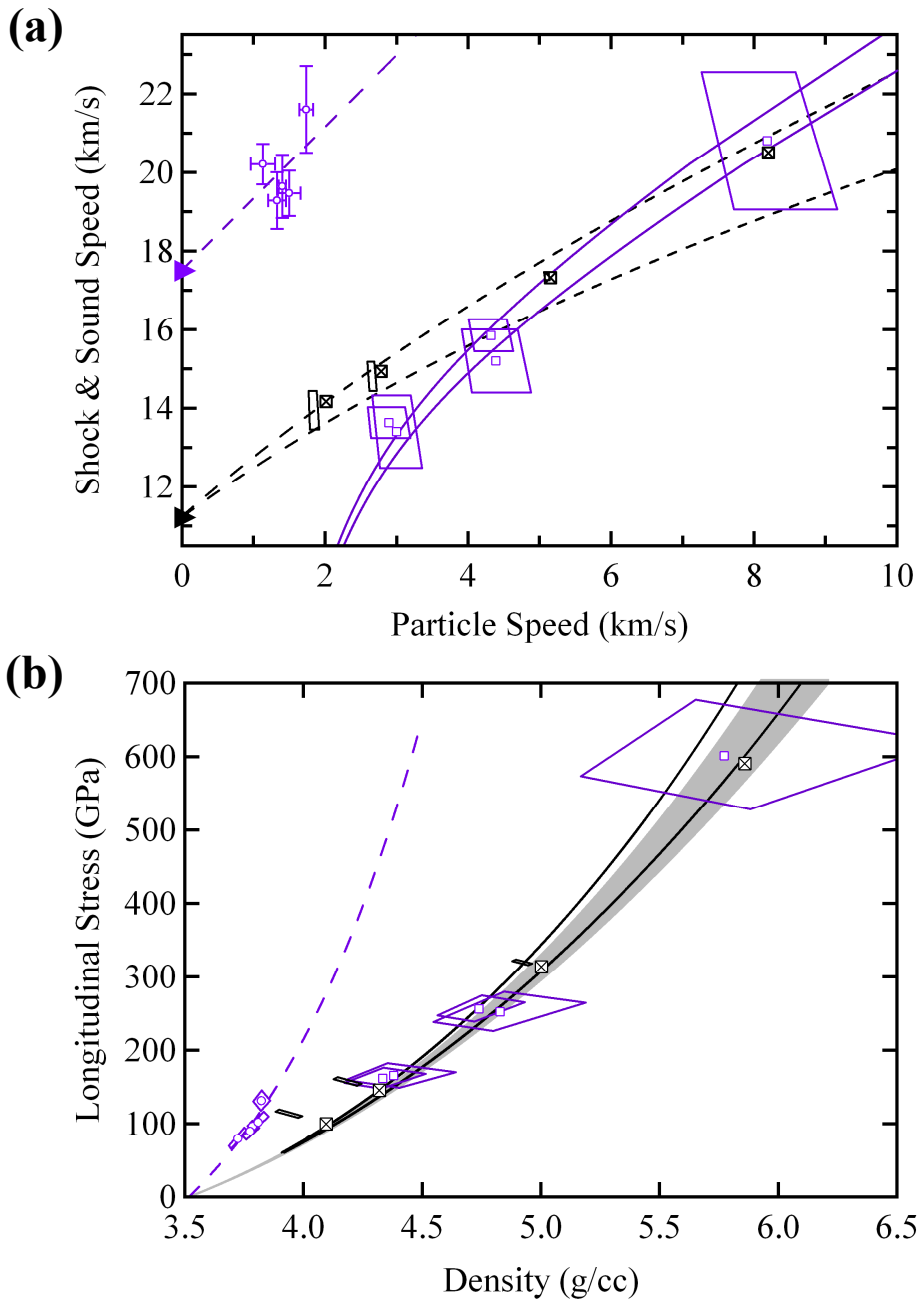

Figure D.1. Original (black, open, crossed squares) and corrected (black open polygons) data of Pavlovskii [23] in (a) *D*-*u* and (b) *P*-ρ spaces, shown with the present results on the <100> orientation of diamond. Remaining symbols and coloration are as in Fig. 1.10 and 1.11. The three lowest stress data of Pavlovskii exhibit shock speeds less than the ambient longitudinal sound speed (purple triangle), which strongly suggests precursors were present in that study. Pavlovskii's data, either before or after correction, show a disagreement with the present results in (a). In (b), the agreement of Pavlovskii's original measurements with the hydrostatic response at low stress may be spurious; correction for an elastic precursor results in a significant deviation from the hydrostat. The highest-stress datum of Pavlovskii is unaffected by the elastic precursor and is considered to be accurate.

BIBLIOGRAPHY

[1] Ross, M. *The Ice Layer in Uranus and Neptune - Diamonds in the Sky.* Nature, **292**(5822), p. 435, 1981.

[2] Benedetti, L.R., et al. *Dissociation of CH4 at high pressures and temperatures: Diamond formation in giant planet interiors?* Science, **286**(5437), p. 100, 1999.

[3] Ancilotto, F., et al. *Dissociation of methane into hydrocarbons at extreme (planetary) pressure and temperature.* Science, **275**(5304), p. 1288, 1997.

[4] Roberge, A., et al. *Stabilization of the disk around beta Pictoris by extremely carbon-rich gas.* Nature, **441**(7094), p. 724, 2006.

[5] Seager, S., et al. *Mass-radius relationships for solid exoplanets.* Astrophysical Journal, **669**(2), p. 1279, 2007.

[6] Bradley, D.K., et al. *Shock compressing diamond to a conducting fluid.* Physical Review Letters, **93**(19), p. 195506, 2004.

[7] Kondo, K. and T.J. Ahrens. *Shock Compression of Diamond Crystal.* Geophysical Research Letters, **10**(4), p. 281, 1983.

[8] Field, J.E. *The Properties of Natural and Synthetic Diamond*. San Diego, Ca: Academic Press, Inc. 1992.

[9] Tyson, W.R. *Theoretical Strength of Perfect Crystals.* Philosophical Magazine, **14**(131), p. 925, 1966.

[10] Kelly, A., W.R. Tyson, and A.H. Cottrell. *Ductile and Brittle Crystals.* Philosophical Magazine, **15**(135), p. 567, 1967.

[11] Ruoff, A.L. *Yield Strength of Diamond.* Journal of Applied Physics, **50**(5), p. 3354, 1979.

[12] Zhao, J.J., et al. *Elasticity and mechanical instabilities of diamond at Megabar stresses: Implications for diamond-anvil-cell research.* Applied Physics Letters, **75**(4), p. 487, 1999.

[13] Chacham, H. and L. Kleinman. *Instabilities in diamond under high shear stress.* Physical Review Letters, **85**(23), p. 4904, 2000.

[14] Roundy, D. and M.L. Cohen. *Ideal strength of diamond, Si, and Ge.* Physical Review B, **6421**(21), p. 212103, 2001.

[15] Telling, R.H., et al. *Theoretical strength and cleavage of diamond.* Physical Review Letters, **84**(22), p. 5160, 2000.

[16] Eremets, M.I., et al. *The strength of diamond.* Applied Physics Letters, **87**(14), 2005.

[17] Altshuler, L.V., M.N. Pavlovskii, and V.P. Drakin. *Peculiarities of Phase Transitions in Compression and Rarefaction Shock Waves.* Soviet Physics JETP - USSR, **25**(2), p. 260, 1967.

[18] Graham, R.A. and W.P. Brooks. *Shock-wave compression of sapphire from 15 to 420 kbar - effects of large anisotropic compressions.* Journal of Physics and Chemistry of Solids, **32**(10), p. 2311, 1971.

[19] Fowles, G.R. *Shock Wave Compression of Hardened and Annealed 2024 Aluminum.* Journal of Applied Physics, **32**(8), p. 1475, 1961.

[20] Grady, D.E. *Processes Occurring in Shock Wave Compression of Rocks and Minerals*, in *High Pressure Research: Applications in Geophysics*, M.H. Manghnani and S. Akimoto, Editors. Academic Press, Inc.: New York. 1977.

[21] Davison, L. and R.A. Graham. *Shock Compression of Solids.* Physics Reports-Review Section of Physics Letters, **55**(4), p. 255, 1979.

[22] Grady, D.E. *Shock Deformation of Brittle Solids.* Journal of Geophysical Research, **85**(NB2), p. 913, 1980.

[23] Pavlovskii, M.N. *Shock Compression of Diamond.* Soviet Physics Solid State - USSR, **13**(3), p. 741, 1971.

[24] Knudson, M.D., et al., *Shock Response of Diamond Crystals, Sandia Report SAND2001-3738*. 2001.

[25] Nagao, H., et al. *Hugoniot measurement of diamond under laser shock compression up to 2 TPa.* Physics of Plasmas, **13**(5), 2006.

[26] Brygoo, S., et al. *Laser-shock compression of diamond and evidence of a negative-slope melting curve.* Nature Materials, **6**(4), p. 274, 2007.

[27] Bradley, D.K., *unpublished.*

[28] Eggert, J.H., et al. *Shock-Compressed Diamond: Melt, Insulator-Conductor, and Polymeric-Atomic Transitions.* In preparation.

[29] Barker, L.M. and R.E. Hollenbach. *Laser Interferometer for Measuring High Velocities of Any Reflecting Surface.* Journal of Applied Physics, **43**(11), p. 4669, 1972.

[30] Celliers, P.M., et al. *Line-imaging velocimeter for shock diagnostics at the OMEGA laser facility.* Review of Scientific Instruments, **75**(11), p. 4916, 2004.

[31] Miller, J.E., et al. *Streaked optical pyrometer system for laser-driven shock-wave experiments on OMEGA.* Review of Scientific Instruments, **78**(3), p. 034903, 2007.

[32] Spaulding, D.K., et al. *New Optical Diagnostics for Equation of State Experiments on the Janus Laser.* AIP Conference Proceedings, **955**(1), p. 1071, 2007.

[33] Barker, L.M. and R.E. Hollenbach. *Shock-Wave Studies of PMMA, Fused Silica, and Sapphire.* Journal of Applied Physics, **41**(10), p. 4208, 1970.

[34] Kwiatkowski, C.S. and Y.M. Gupta. *Optical measurements to probe inelastic deformation in shocked brittle materials*. in *Shock Compression of Condensed Matter 1999*. Snowbird, Utah (USA): AIP 2000.

[35] Fat'yanov, O.V., R.L. Webb, and Y.M. Gupta. *Optical transmission through inelastically deformed shocked sapphire: stress and crystal orientation effects.* Journal of Applied Physics, **97**(12), p. 123529, 2005.

[36] Correa, A.A., S.A. Bonev, and G. Galli. *Carbon under extreme conditions: Phase boundaries and electronic properties from first-principles theory.* Proceedings of the National Academy of Sciences of the United States of America, **103**(5), p. 1204, 2006.

[37] Romero, N.A. and W.D. Mattson. *Density-functional calculation of the shock Hugoniot for diamond.* Physical Review B, **76**(21), p. 214113, 2007.

[38] Grady, D.E. *Shock-wave compression of brittle solids.* Mechanics of Materials, **29**(3-4), p. 181, 1998.

[39] Hicks, D.G., et al. *Shock compression of quartz in the high-pressure fluid regime.* Physics of Plasmas, **12**(8), p. 082702, 2005.

[40] Hicks, D.G., et al. *Dissociation of liquid silica at high pressures and temperatures.* Physical Review Letters, **97**(2), p. 025502, 2006.

[41] Jones, S.C. and Y.M. Gupta. *Refractive index and elastic properties of z-cut quartz shocked to 60 kbar.* Journal of Applied Physics, **88**(10), p. 5671, 2000.

[42] Brugger, K. *Pure Modes for Elastic Waves in Crystals.* Journal of Applied Physics, **36**(3P1), p. 759, 1965.

[43] Winey, J.M. and Y.M. Gupta. *Nonlinear anisotropic description for shocked single crystals: Thermoelastic response and pure mode wave propagation.* Journal of Applied Physics, **96**(4), p. 1993, 2004.

[44] Boteler, J.M., *Time resolved Raman spectroscopy in diamonds shock compressed along [110] and [100] orientations.* Thesis, Washington State University. 1993.

[45] Wackerle, J. *Shock-Wave Compression of Quartz.* Journal of Applied Physics, **33**(3), p. 922, 1962.

[46] Fowles, R. *Dynamic Compression of Quartz.* Journal of Geophysical Research, **72**(22), p. 5729, 1967.

[47] Balzaretti, N.M. and J.A.H. daJornada. *Pressure dependence of the refractive index of diamond, cubic silicon carbide and cubic boron nitride.* Solid State Communications, **99**(12), p. 943, 1996.

[48] Eremets, M.I., et al. *Refractive index of diamond under pressure.* High Pressure Research, **9-10**(1-2), p. 347, 1992.

[49] Vogelgesang, R., et al. *Brillouin and Raman scattering in natural and isotopically controlled diamond.* Physical Review B, **54**(6), p. 3989, 1996.

[50] Asay, J.R., Y. Gupta, and G.R. Fowles. *Determination of Material Relaxation Properties from Measurements on Decaying Elastic Shock Fronts.* Journal of Applied Physics, **43**(2), p. 744, 1972.

[51] Ahrens, T.J., W.H. Gust, and E.B. Royce. *Material Strength Effect in Shock Compression of Alumina.* Journal of Applied Physics, **39**(10), p. 4610, 1968.

[52] Goto, T., T. Sato, and Y. Syono. *Reduction of Shear-Strength and Phase-Transition in Shock-Loaded Silicon.* Japanese Journal of Applied Physics Part 2-Letters, **21**(6), p. L369, 1982.

[53] Turneaure, S.J. and Y.M. Gupta. *Inelastic deformation and phase transformation of shock compressed silicon single crystals.* Applied Physics Letters, **91**(20), p. 201913, 2007.

[54] Celliers, P.M., et al. *Systematic uncertainties in shock-wave impedance-match analysis and the high-pressure equation of state of Al.* Journal of Applied Physics, **98**(11), p. 113529, 2005.

[55] Kerley, G.I. *Theoretical equation of state for aluminum.* International Journal of Impact Engineering, **5**(1-4), p. 441, 1987.

[56] Kerley, G.I., *Equations of State for Composite Materials, Kerley Report KPS99-4*. Kerley Publishing Services: Albuquerque, N.M. 1999.

[57] Graham, R.A. *Determination of Third-Order and Fourth-Order Longitudinal Elastic-Constants by Shock Compression Techniques - Application to Sapphire and Fused Quartz.* Journal of the Acoustical Society of America, **51**(5), p. 1576, 1972.

[58] Anastassakis, E., A. Cantarero, and M. Cardona. *Piezo-Raman Measurements and Anharmonic Parameters in Silicon and Diamond.* Physical Review B, **41**(11), p. 7529, 1990.

[59] Occelli, F., P. Loubeyre, and R. Letoullec. *Properties of diamond under hydrostatic pressures up to 140 GPa.* Nature Materials, **2**(3), p. 151, 2003.

[60] Datchi, F., et al. *Equation of state of cubic boron nitride at high pressures and temperatures.* Physical Review B, **75**(21), p. 214104, 2007.

[61] Kunc, K., I. Loa, and K. Syassen. *Equation of state and phonon frequency calculations of diamond at high pressures.* Physical Review B, **68**(9), p. 094107, 2003.

[62] Maezono, R., et al. *Equation of state and Raman frequency of diamond from quantum Monte Carlo simulations.* Physical Review Letters, **98**(2), p. 025701, 2007.

[63] Jeanloz, R., et al. *Achieving high-density states through shock-wave loading of precompressed samples.* Proceedings of the National Academy of Sciences of the United States of America, **104**(22), p. 9172, 2007.

[64] Winey, J.M. and Y.M. Gupta. *Nonlinear anisotropic description for the thermomechanical response of shocked single crystals: Inelastic deformation.* Journal of Applied Physics, **99**(2), p. 023510, 2006.

[65] Birch, F. *Finite Strain Isotherm and Velocities for Single-Crystal and Polycrystalline NaCl at High-Pressures and 300-Degree-K.* Journal of Geophysical Research, **83**(NB3), p. 1257, 1978.

[66] Barsch, G.R. *Adiabatic Isothermal and Intermediate Pressure Derivatives of Elastic Constants for Cubic Symmetry.* Physica Status Solidi, **19**(1), p. 129, 1967.

[67] Spetzler, H., C.G. Sammis, and R.J. O'Connell. *Equation of State of NaCl - Ultrasonic Measurements to 8 Kbar and 8000 Degrees C and Static Lattice Theory.* Journal of Physics and Chemistry of Solids, **33**(9), p. 1727, 1972.

[68] Slack, G.A. and S.F. Bartram. *Thermal-Expansion of Some Diamond-Like Crystals.* Journal of Applied Physics, **46**(1), p. 89, 1975.

[69] Victor, A.C. *Heat Capacity of Diamond at High Temperatures.* Journal of Chemical Physics, **36**(7), p. 1903, 1962.

[70] Nielsen, O.H. *Optical Phonons and Elasticity of Diamond at Megabar Stresses.* Physical Review B, **34**(8), p. 5808, 1986.

[71] Zouboulis, E.S., et al. *Temperature dependence of the elastic moduli of diamond: A Brillouin-scattering study.* Physical Review B, **57**(5), p. 2889, 1998.

[72] Dewaele, A., et al. *High pressure-high temperature equations of state of neon and diamond.* Physical Review B, **77**(9), p. 094106, 2008.

[73] Zel'dovich, Y.B. and Y.P. Raizer. *Physics of Shock Waves and High-Temperature Hydrodynamic Phenomena*, ed. W.D. Hayes and R.F. Probstein. Mineola, New York: Dover Publications, Inc. 2002.

[74] McLaughlin, K., et al. *Molecular Dynamics Simulations of an Anomalous Response of Diamond to Shock Compression.* AIP Conference Proceedings, **955**(1), p. 321, 2007.

[75] Zybin, S.V., M.L. Elert, and C.T. White. *Nanoscale view of shock-wave splitting in diamond.* Metallurgical and Materials Transactions A - Physical Metallurgy and Materials Science, **35A**(9), p. 2647, 2004.

[76] Steinberg, D.J., S.G. Cochran, and M.W. Guinan. *A Constitutive Model for Metals Applicable at High-Strain Rate.* Journal of Applied Physics, **51**(3), p. 1498, 1980.

[77] Vogler, T.J. and L.C. Chhabildas. *Strength behavior of materials at high pressures.* International Journal of Impact Engineering, **33**(1-12), p. 812, 2006.

[78] Whitlock, J. and A.L. Ruoff. *The failure strengths of perfect diamond crystals.* Scripta Metallurgica, **15**(5), p. 525, 1981.

[79] Dorogokupets, P.I. and A.R. Oganov. *Ruby, metals, and MgO as alternative pressure scales: A semiempirical description of shock-wave, ultrasonic, x-ray, and thermochemical data at high temperatures and pressures.* Physical Review B, **75**(2), p. 024115, 2007.

[80] Cardona, M. *Semiconductors under uniaxial strain.* Physica Status Solidi B - Basic Research, **198**(1), p. 5, 1996.

[81] Zhao, J.J., J.M. Winey, and Y.M. Gupta. *First-principles calculations of second- and third-order elastic constants for single crystals of arbitrary symmetry.* Physical Review B, **75**(9), p. 094105, 2007.

[82] Thurston, R.N. *Wave Propagation in Fluids and Normal Solids.* Physical Acoustics, **1-A**, p. 1, 1964.

[83] Birch, F. *Finite Elastic Strain of Cubic Crystals.* Physical Review, **71**(11), p. 809, 1947.

[84] Jeanloz, R. *Shock-Wave Equation of State and Finite Strain Theory.* Journal of Geophysical Research - Solid Earth and Planets, **94**(B5), p. 5873, 1989.

[85] Murnaghan, F.D. *Finite deformations of an elastic solid.* American Journal of Mathematics, **59**, p. 235, 1937.

[86] Jeanloz, R. *Universal Equation of State.* Physical Review B, **38**(1), p. 805, 1988.

[87] Wallace, D.C. *Thermoelasticity of Stressed Materials and Comparison of Various Elastic Constants.* Physical Review, **162**(3), p. 776, 1967.

[88] Weiner, J.H. *Statistical Mechanics of Elasticity*. New York: John Wiley & Sons, Inc. 1983.

[89] Hankey, R.E. and D.E. Schuele. *Third-Order Elastic Constants of Al2O3.* Journal of the Acoustical Society of America, **48**(1), p. 190, 1970.

[90] Gieske, J.H. and G.R. Barsch. *Pressure Dependence of Elastic Constants of Single Crystalline Aluminum Oxide.* Physica Status Solidi, **29**(1), p. 121, 1968.

[91] Thurston, R.N., H.J. McSkimin, and P. Andreatch. *3rd-Order Elastic Coefficients of Quartz.* Journal of Applied Physics, **37**(1), p. 267, 1966.

[92] McSkimin, H.J., P. Andreatch, and R.N. Thurston. *Elastic Moduli of Quartz Versus Hydrostatic Pressure at 25 Degrees and -195.8 Degrees C.* Journal of Applied Physics, **36**(5), p. 1624, 1965.

[93] Heinz, D.L. and R. Jeanloz. *The Equation of State of the Gold Calibration Standard.* Journal of Applied Physics, **55**(4), p. 885, 1984.

[94] Davies, G.F. *Invariant Finite Strain Measures in Elasticity and Lattice-Dynamics.* Journal of Physics and Chemistry of Solids, **34**(5), p. 841, 1973.

[95] Davies, G.F. *Quasi-Harmonic Finite Strain Equations of State of Solids.* Journal of Physics and Chemistry of Solids, **34**(8), p. 1417, 1973.

[96] Thomsen, L. *On Fourth-Order Anharmonic Equation of State of Solids.* Journal of Physics and Chemistry of Solids, **31**(9), p. 2003, 1970.

[97] Thomsen, L. *Fourth-Order Anharmonic Theory - Elasticity and Stability.* Journal of Physics and Chemistry of Solids, **33**(2), p. 363, 1972.

[98] Malvern, L.E. *Introduction to the Mechanics of a Continuous Media.* Upper Saddle River, NJ: Prentice-Hall, Inc. 1969.

[99] Jones, S.C., B.A.M. Vaughan, and Y.M. Gupta. *Refractive indices of sapphire under elastic, uniaxial strain compression along the a axis.* Journal of Applied Physics, **90**(10), p. 4990, 2001.

[100] Mashimo, T., Y. Hanaoka, and K. Nagayama. *Elastoplastic Properties under Shock Compression of Al2O3 Single-Crystal and Polycrystal.* Journal of Applied Physics, **63**(2), p. 327, 1988.

[101] Winey, J.M., Y.M. Gupta, and D.E. Hare. *R-axis sound speed and elastic properties of sapphire single crystals.* Journal of Applied Physics, **90**(6), p. 3109, 2001.

[102] Boteler, J.M. and Y.M. Gupta. *Shock-Induced Splitting of the Triply Degenerate Raman Line in Diamond.* Physical Review Letters, **71**(21), p. 3497, 1993.

[103] Boteler, J.M. and Y.M. Gupta. *Raman spectra of shocked diamond single crystals.* Physical Review B, **66**(1), p. 014107, 2002.

[104] Grimsditch, M.H., E. Anastassakis, and M. Cardona. *Effect of Uniaxial Stress on Zone-Center Optical Phonon of Diamond.* Physical Review B, **18**(2), p. 901, 1978.

[105] Zybin, S.V., et al. *Atomistic Modeling of Orientation Dependence of Shock Wave Properties in Diamond*. in *Shock Compression of Condensed Matter - 2001: 12th APS Topical Conference*: AIP 2002.

[106] Zybin, S.V., et al. *Nanoscale Modelling of Shock-Induced Deformation.* Materials Research Society Symposium Proceedings, **800**, p. AA7.7.1, 2004.

[107] Nielsen, O.H., *Personal Communication.* 2008.

[108] Thurston, R.N. *Definition of a Linear Medium for 1-Dimensional Longitudinal Motion.* Journal of the Acoustical Society of America, **45**(6), p. 1329, 1969.

[109] Nelson, D.A. and A.L. Ruoff. *Compressive Strength of Perfect Diamond.* Journal of Applied Physics, **50**(4), p. 2763, 1979.

[110] Ruoff, A.L. *Ultimate Yield Strength of Solids.* Journal of Applied Physics, **49**(1), p. 197, 1978.

[111] Jamieson, J.C. *Crystal Structures at High Pressures of Metallic Modifications of Silicon and Germanium.* Science, **139**(355), p. 762, 1963.

[112] Gupta, M.C. and A.L. Ruoff. *Static compression of silicon in the [100] and in the [111] directions.* Journal of Applied Physics, **51**(2), p. 1072, 1980.

[113] Scandolo, S., G.L. Chiarotti, and E. Tosatti. *Stability of diamond at Megabar pressures.* Physica Status Solidi B - Basic Research, **198**(1), p. 447, 1996.

[114] Lee, I.H., J.W. Jeong, and K.J. Chang. *Invariant-molecular-dynamics study of the diamond-to-beta-Sn transition in Si under hydrostatic and uniaxial compressions.* Physical Review B, **55**(9), p. 5689, 1997.

[115] Gogotsi, Y.G., A. Kailer, and K.G. Nickel. *Materials - Transformation of diamond to graphite.* Nature, **401**(6754), p. 663, 1999.

[116] Cheng, C., W.H. Huang, and H.J. Li. *Thermodynamics of uniaxial phase transition: Ab-initio study of the diamond-to-beta-tin transition in Si and Ge.* Physical Review B, **63**(15), p. 153202, 2001.

[117] Lyzenga, G.A., T.J. Ahrens, and A.C. Mitchell. *Shock Temperatures of SiO2 and Their Geophysical Implications.* Journal of Geophysical Research, **88**(NB3), p. 2431, 1983.

[118] Luo, S.N. and T.J. Ahrens. *Shock-induced superheating and melting curves of geophysically important minerals.* Physics of the Earth and Planetary Interiors, **143-44**, p. 369, 2004.

[119] Hayes, D. *Unsteady compression waves in interferometer windows.* Journal of Applied Physics, **89**(11), p. 6484, 2001.

[120] Marler, B. *On the Relationship between Refractive-Index and Density for SiO2 Polymorphs.* Physics and Chemistry of Minerals, **16**(3), p. 286, 1988.

[121] Lee, C.Y. and X. Gonze. *SiO2 stishovite under high pressure: Dielectric and dynamical properties and the ferroelastic phase transition.* Physical Review B, **56**(12), p. 7321, 1997.

[122] Stoffler, D. and F. Langenhorst. *Shock Metamorphism of Quartz in Nature and Experiment: 1. Basic Observation and Theory.* Meteoritics, **29**(2), p. 155, 1994.

[123] Akins, J.A. and T.J. Ahrens. *Dynamic compression of SiO2: A new interpretation.* Geophysical Research Letters, **29**(10), 2002.

[124] Alt'shuler, L. *Use of Shock Waves in High-Pressure Physics.* Soviet Physics Uspekhi - USSR, **8**(1), p. 52, 1965.

[125] Altshuler, V.L., et al. *Investigation of Alkali-Metal Halides at High Pressures and Temperatures Produced by Shock Compression.* Soviet Physics-Solid State, **5**(1), p. 203, 1963.

[126] Trunin, R. *Shock Compression of Condensed Material*. Cambridge: Camb. Univ. Press. 1998.

[127] Pavlovskii, M. *Formation of Metallic Modifications of Germanium and Silicon under Shock Loading.* Soviet Physics Solid State - USSR, **9**(11), p. 2514, 1968.